Development and Calibration of New 3-D Vector VSP Imaging Technology:
Vinton Salt Dome, LA

FINAL REPORT

Report Period: September 25, 2001 – August 31, 2004

Principal Authors: Dr. Kurt J. Marfurt
Dr. Hua-Wei Zhou
Dr. E. Charlotte Sullivan

Date issued: September 2004

DOE Award Number: DE-FC26-01BC15353

Name and Address of Submitting Organization:

University of Houston
4800 Calhoun, SR1, Room 504
Houston, TX 77204-5006

DISCLAIMER

ABSTRACT:

Vinton salt dome is located in Southwestern Louisiana, in Calcasieu Parish. Tectonically, the piercement dome is within the salt dome minibasin province. The field has been in production since 1901, with most of the production coming from Miocene and Oligocene sands. The goal of our project was to develop and calibrate new processing and interpretation technology to fully exploit the information available from a simultaneous 3-D surface seismic survey and 3-C, 3-D vertical seismic profile (VSP) survey over the dome. More specifically the goal was to better image salt dome flanks and small, reservoir-compartmentalizing faults. This new technology has application to mature salt-related fields across the Gulf Coast.

The primary focus of our effort was to develop, apply, and assess the limitations of new 3-C, 3-D wavefield separation and imaging technology that could be used to image aliased, limited-aperture, vector VSP data. Through 2-D and 3-D full elastic modeling, we verified that salt flank reflections exist in the horizontally-traveling portion of the wavefield rather than up- and down-going portions of the wavefield, thereby explaining why many commercial VSP processing flow failed. Since the P-wave reflections from the salt flank are measured primarily on the horizontal components while P-wave reflections from deeper sedimentary horizons are measured primarily on the vertical component, a true vector VSP analysis was needed.

We developed an antialiased discrete Radon transform filter to accurately model P- and S-wave data components measured by the vector VSP. On-the-fly polarization filtering embedded in our Kirchhoff imaging algorithm was effective in separating PP from PS wave images. By the novel application of semblance-weighted filters, we were able to suppress many of the migration artifacts associated with low fold, sparse VSP acquisition geometries. To provide a better velocity/depth model, we applied 3-D prestack depth migration to the surface data. The reflector dip calculated from these images were used to further constrain the depth images from the less well sampled VSP data.

In spite of the above technical success, we were less than pleased with our final VSP images. Since no extra sources are used, simultaneous recording of the surface and VSP data were believed to provide a cost-effective means to acquire 3-D VSP data. However, the subsurface sampling associated with the VSP is quite different from that associated with the surface seismic data. After our analysis, we find that considerable shot infill would result in a better, unaliased subsurface image. We were able to ascertain that the subsurface illuminated by the VSP was extremely small, with the PS image being even smaller than the PP image. One-way wave equation extrapolators do not work well for the VSP geometry, where we wish to extrapolate energy sideways (from the VSP well towards and away from the salt dome) as well as vertically (away from the shots on the earth surface). Merging separately-generated images proved to be both cumbersome and error-prone. Alternative, advanced multiarrival traveltime calculations that we obtained from research colleagues at other institutions could not be easily modified to image rays that had an upgoing component. In the end, we used a simpler first-arrival Eikonal-based traveltime algorithm with its well-known limitations.

While the surface acquisition using radial receiver lines and concentric shot lines provided good illumination of the salt dome, this unconventional geometry proved to be particularly difficult to process using commercial software, where the lack of "shot lines" and "receiver lines" necessary for dip filtering, residual statics, and residual velocity analysis proved to be nearly intractable. We also learned that while commercial software available at UH works well for a bootstrapped velocity model computed from the seismic data alone, it was severely limited in its ability to include the dense well control available at Vinton Dome.

To more accurately estimate velocities, we developed a 3-D turning wave tomography algorithm adapted to the VSP geometry employed at Vinton Dome. We were able to determine that there is about 10% anisotropy at Vinton Dome, with the axis of transverse isotropy perpendicular to the geologic formations deformed by the diapirism. At the time of this final report, we have not yet integrated traveltimes from the surface data into the tomographic inversion to better constrain the velocity model, nor developed an anisotropic migration algorithm to image the 3-D 3-C VSP (objectives well beyond the original scope of the project).

As a secondary objective, we developed a suite of new 3-D volumetric attribute algorithms and image enhancement algorithms. We estimate volumetric dip and azimuth using a multiwindow Kuwahara approach that avoids smoothing amplitude and dip across faults. Based on these robust estimates of dip and azimuth, we developed a unique structure-oriented filtering algorithm based on principal component filtering. We also developed a modified seismic coherence algorithm based on the analytic trace rather than the 'real part' of the seismic data, thereby avoiding artifacts at zero crossings. Coherent energy gradients, a by-product of the principle component filtering, provide good indications of channels that fall below the tuning thickness. Finally, we developed and applied volumetric curvature to map both short and long wavelength variations in reflector dip and azimuth. We found that long wavelength estimates of most negative and most positive curvature to be particularly useful, allowing us to map subtle faults that do not show up in coherence and are difficult to correlate on time slices through the seismic data.

The new VSP processing and migration technology, augmented by the structure-oriented filtering and seismic attributes, has the potential to improve imaging of reservoir compartmentalization, not only for the petroleum industry, but also for the larger public issue of subsurface imaging of geologic structures being considered for CO_2 sequestration. The new geometric attributes calibrated during this study are now being used to reduce geologic and mechanical risk in petroleum exploration across the USA in the Fort Worth Basin, the Permian Basin, East Texas Basin, Midcontinent and the Greater Green River Basins, in addition to the Gulf Coast.

The Vinton Dome project resulted in four MS theses, two PhD theses, and 24 presentations and/or publications at National and International meetings. Two additional

theses, one MS and one PhD, are under completion. In addition, the results of the Vinton Dome project have been presented to some 15 oil companies working the Gulf Coast region of the USA. These results have been and continue to be used as teaching material in seismic attribute short courses and seismic interpretation classes and are expected to result in at least four additional peer-reviewed publications. We are currently applying and perfecting our tomography, filtering, and imaging technology to three 3-C VSPs acquired offshore Long Beach, California, over the Wilmington field operated by Occidental for the City of Long Beach and the State of California.

TABLE OF CONTENTS:

1.0 INTRODUCTION:

Geophysical data acquired in 1997 at Vinton Dome, a piercement salt feature in Calcasieu Parish, southwestern Louisiana, included 3-D surface seismic and two 3-D vertical seismic profiles (VSP). Due to limitations in software, contractor processing of the VSPs was restricted to the vertical component, and failed to image the salt flank. The surface seismic data were also commercially processed using current industry standards (prestack time migration), but resulted in a seismic volume having only moderate vertical and lateral resolution. While the input data and processing of both the VSP and surface seismic data quality met or exceeded industry standards, the resulting images did not have the resolution necessary to accurately image the flanks of the dome and the small faults that compartmentalize this prolific, super-mature field. Targets of interest can be as small as 4 hectares (10 acres), but produce over 1 million bbl of oil. At Vinton dome, where the top of salt is only a few hundred feet below the surface, P-wave seismic velocities in the salt can be twice those in the adjacent sediments. Spatial fidelity is highly dependent upon the velocity model. We addressed the image fidelity problem through experiments in reflection tomography, VSP processing, physical and numerical seismic modeling, prestack depth migration, and seismic attribute analysis.

1.1 Vinton Salt Dome Geology

Vinton Dome is located in Southwestern Louisiana, Calcasieu Parish, 3 ½ miles southwest of the town of Vinton (Figure 1.1.1). Vinton Dome is within the salt dome minibasin province, which is characterized by stocks of Jurassic salt and intervening Cenozoic shelf minibasins, bounded by large-displacement, arcuate, predominantly

counter-regional, growth faults (Jackson et al., 1995). Vinton was the first of the salt dome oil fields in which oil was found on salt dome flanks. The first well was drilled in May 1901, near the bank of the east side of Gray Lake (Thompson and Eichelberger, 1928).

Surface geology

The layers exposed at the surface belong to the Port Hudson series, of Pleistocene age, which in Texas is known as the Beaumont clay. This series is composed of sands and clays (Thompson and Eichelberger, 1928; Wilson and Noel, 1983).

Subsurface geology

The subsurface geology in the survey area consists of strata that are relatively flat distal to the salt dome, and steeply dipping in the vicinity of the dome. The dome consists of a core of massive salt and a well defined cap-rock that successively grades downward from limestone to gypsum and anhydrite. The evaporites commonly have cavernous porosity, which may be filled with sulphur water (Thompson and Eichelberger, 1928). The salt core is approximately 4200 ft wide North-South and 5000 ft long from East to West (Figures 1.1.2 and 1.1.3). The highest elevation of the dome is 925 ft below sea level near the north end of Gray Lake. The uppermost Pleistocene sands, gravels and clays dip gently away from the dome.

Pre-Pleistocene sediments include Miocene to Pliocene sandstones and shales of the Fleming Formation (Wilson and Noel, 1983), which overlies the Anahuac and Frio

Formations. The Oligocene Vicksburg Formation and the Eocene Jackson Group occur below the Frio. Thompson and Eichelberger (1928) provided the first basic stratigraphic description of the Vinton dome area. Details of the stratigraphy are shown in stratigraphic column for the Gulf of Mexico (Figure 1.1.4) and are outlined below.

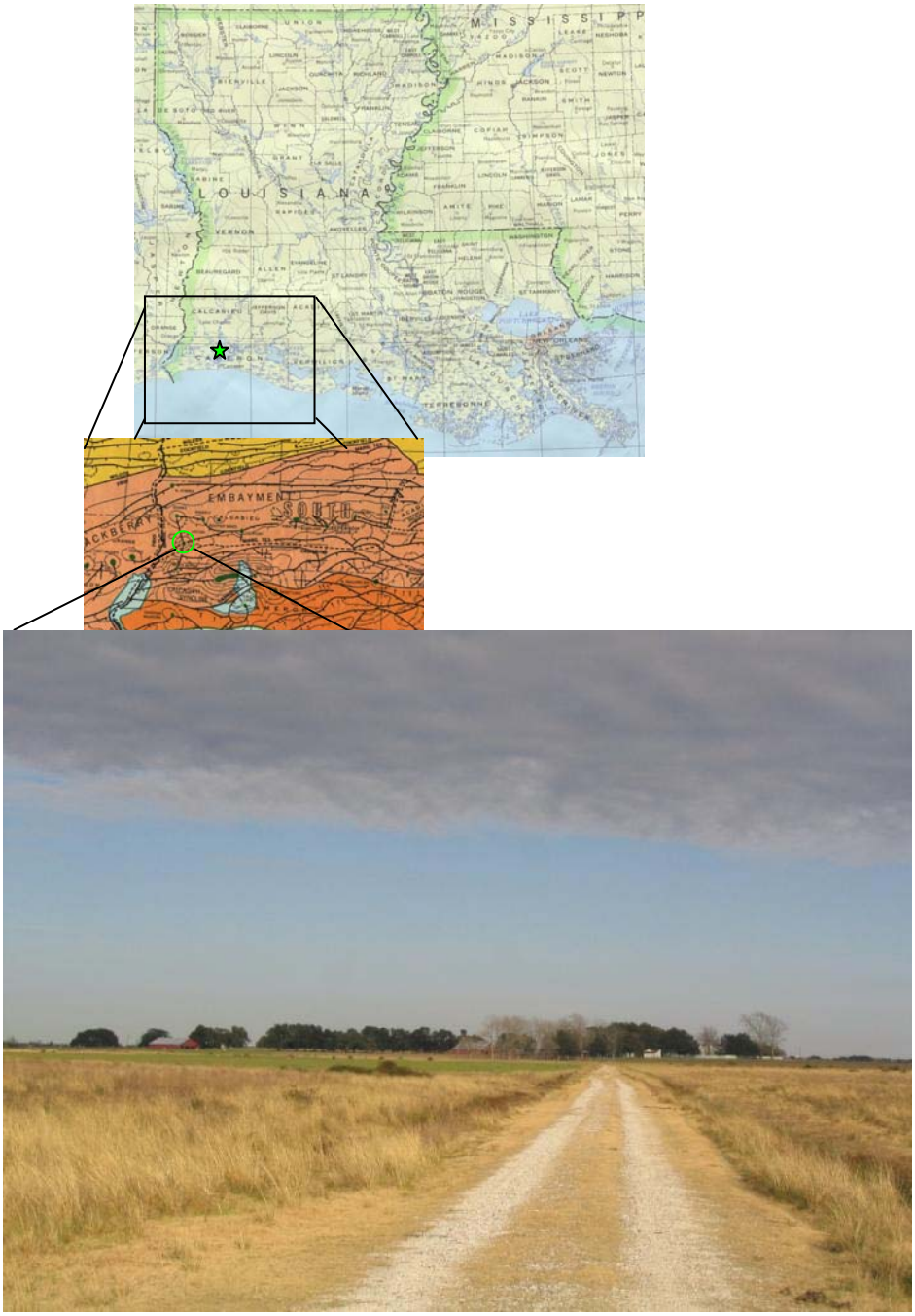

Figure 1.1.1. Location of the Vinton salt dome (From Duncan, 2005).

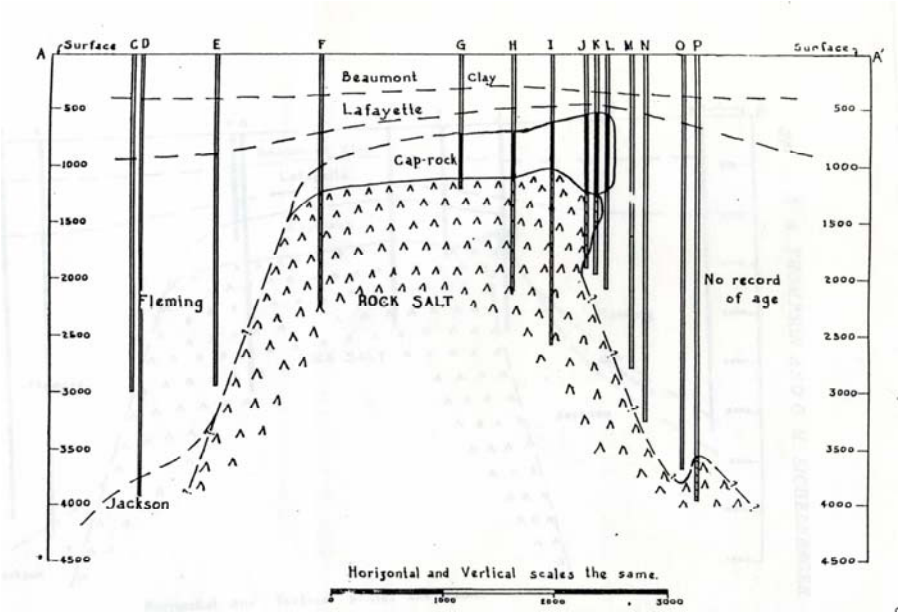

Figure 1.1.2. North-South diagrammatic cross-section of the Vinton salt dome. Jurassic salt, deposited in rifts associated with the opening of the Gulf of Mexico, was deformed by Mesozoic and Cenozoic sediment loading and by largely syndepositional faulting (after Thompson and Eichelberger, 1928).

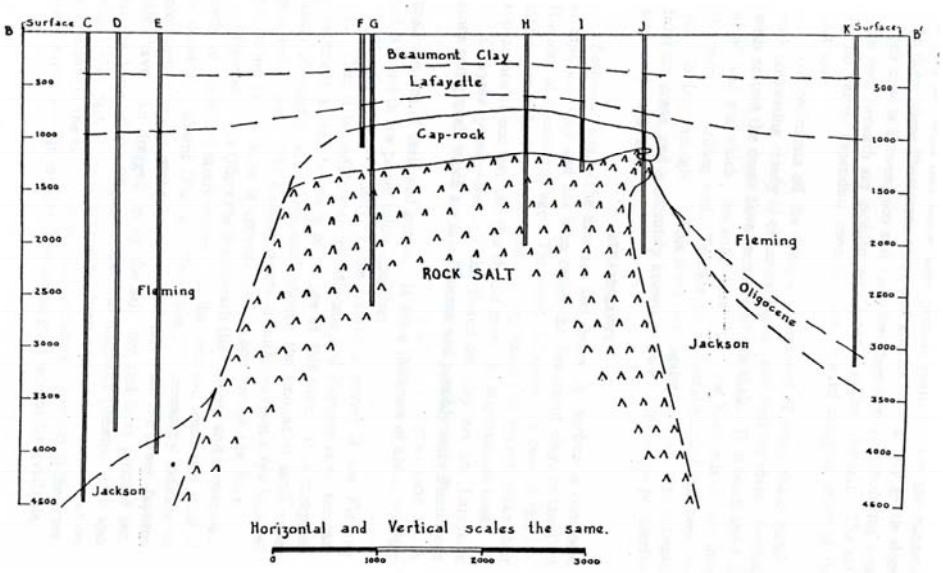

Figure 1.1.3. East-West diagrammatic cross section through the Vinton salt dome. Lowermost sedimentary rocks shown in this figure belong to the Upper Eocene Jackson Group (after Thompson and Eichelberger, 1928).

Beaumont clay

The first 200 ft (61 m) below the surface is composed of sand and clay and has been called the Beaumont clay, or the Port Hudson, of Pleistocene age. Beds of gravel appear at 400 ft (122 m) and mark the approximate base of the Beaumont clay.

Lafayette gravel

Beneath the Beaumont clay are the Lafayette sands and gravels of late Pliocene and to early Pleistocene age. This interval is dominated by gravel, but includes sand and a small amount of shale and gumbo clay. The Lafayette gravel has a thickness of about 600 ft (183 m) and seldom occurs below a depth of about 1000 ft (305 m).

Fleming Group

Underlying the Lafayette gravel is the Fleming Group. Here the Group consists of undifferentiated Miocene and Pliocene age clays and mudstones, with a variable amount of sand. The Fleming ranges in thickness from a few hundred feet on top of the dome to approximately 3000 ft (915 m) on the flank. The Miocene Fleming sands are productive close to the dome, and were deposited in deltaic and marginal marine environments. The results of this project indicate that lateral variation in the Fleming sands is probably one of the major contributors to seismic velocity heterogeneity. We now have a graduate student mapping the Miocene sands as part of her master's thesis research.

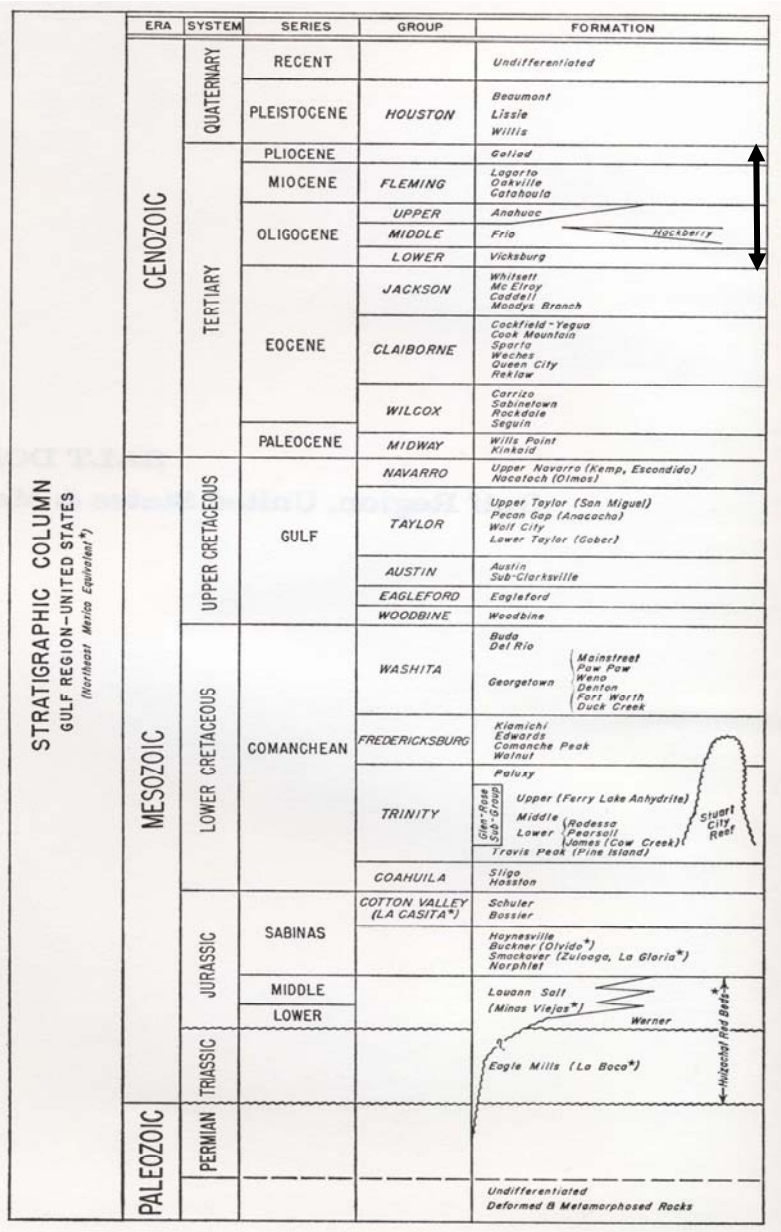

Figure 1.1.4. Stratigraphic column of Gulf of Mexico (after Halbouty, 1972). Arrow indicates the Cenozoic interval of interest at Vinton Dome.

Oligocene

The Oligocene section beneath the Fleming is composed chiefly of shale, sandstone and sandy shale of the Anahuac and Frio Formations (Figures 1.1.5 and 1.1.6). It is absent on the West and Southwest sides of the dome (Figure 1.1.2). This does not necessarily

indicate an unconformity but is probably due to the fact that the lower Jackson shales have been dragged up by the salt core and have pinched out all the Oligocene that was originally present near the dome. Part of the Oligocene may have been irregularly pinched out on the east side in the same manner. As a consequence, the thickness of 300 ft (92 m) in the cross-section is only a rough estimate. The deepest wells in the study area penetrate Oligocene sediments, and the following is a more detailed discussion of the stratigraphy of the Oligocene strata.

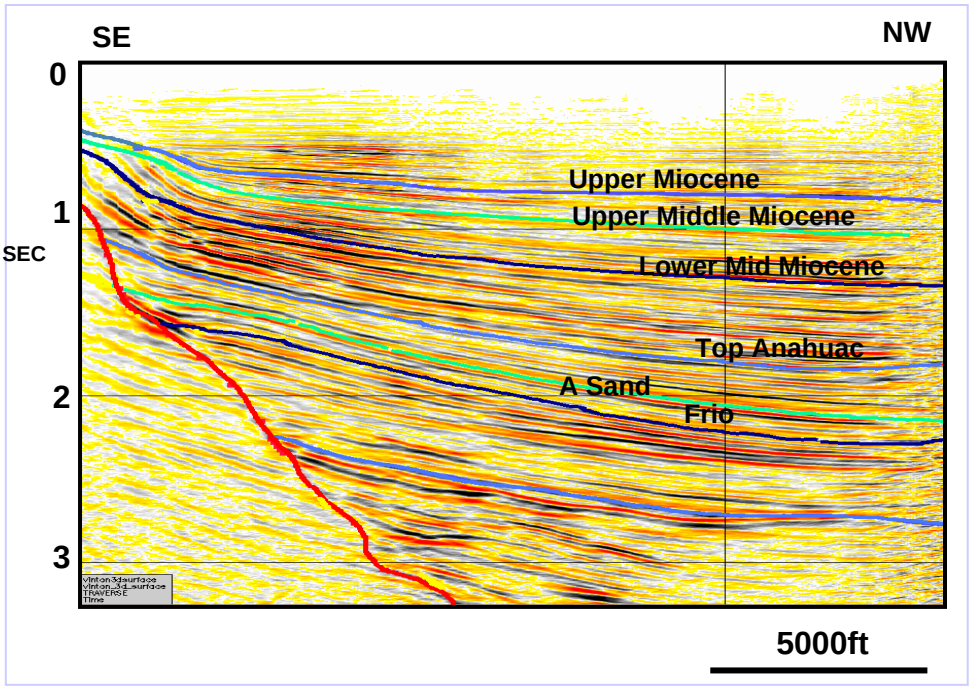

Figure 1.1.5. Seismic section across the northwest part of the Vinton Dome survey. The Fleming Group Miocene sands are productive only close to the salt dome, but both the Miocene and overlying Pliocene deltaic and shallow shelf sands cause considerable velocity heterogeneity within the survey. Main production is from the middle and outer shelf Klumpp A, B, C, and D upper Frio sandstones.

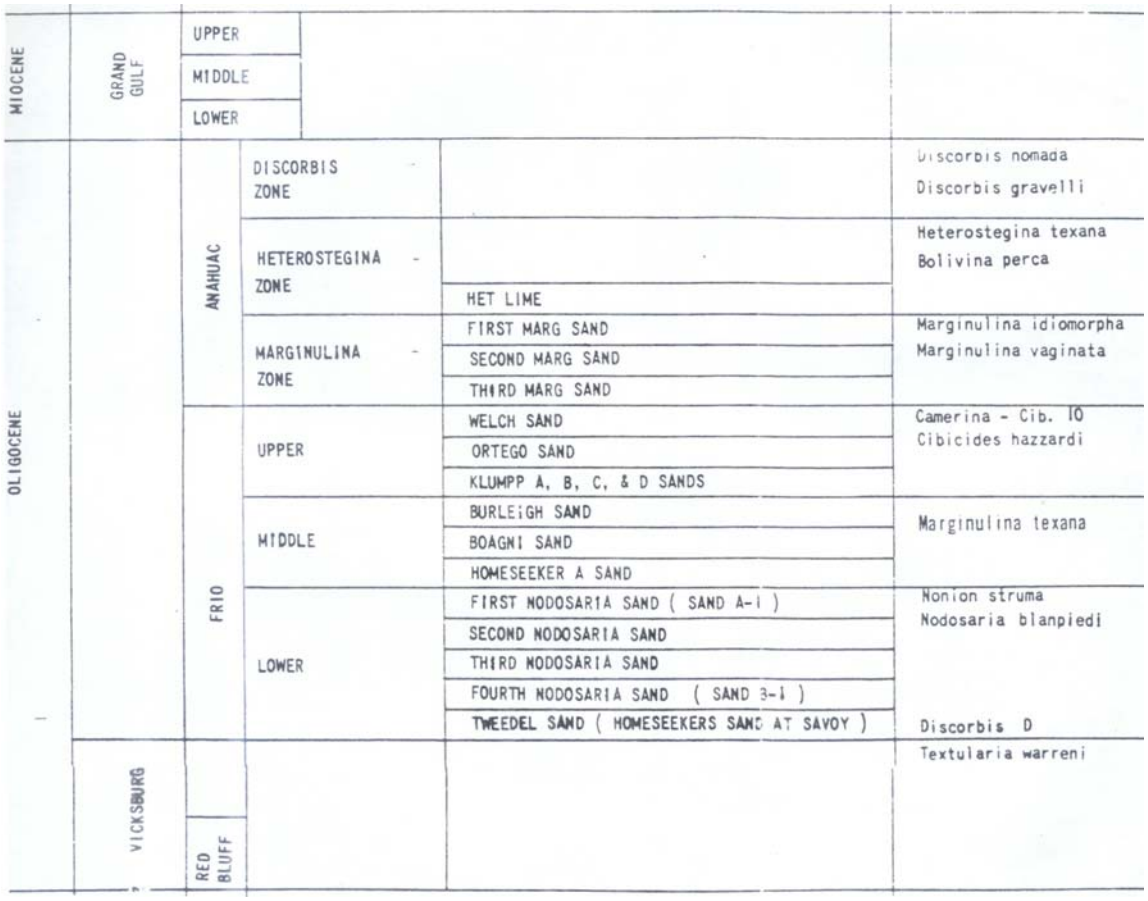

Figure 1.1.6. Details of the Oligocene stratigraphic column in the Vinton Dome area (after Tabbi-Anneni, 1975). A major sea level drop at the base of the Anahuac caused incision and down-cutting through the underlying Frio and Vicksburg. The Hackberry sandstones and shales (Figure 1.1.4) were deposited as turbidites and other gravity process deposits within these large submarine channels. Without 3-D coverage, areas of faulting can be mistaken for "Hackberry channels".

The **Anahuac Formation** is considered to be located at the top of Oligocene interval, and contains shale and sandstones deposited in marginal to shallow marine environments, during a major late Oligocene marine transgression (Wilson and Noel, 1983). Dark, greenish gray, calcareous shale with beds of sand and calcareous sand and occasional thin lenses of limestone are also present (Warren, 1957). The unit becomes more calcareous eastward and finally grades into reefal and bioclastic detrital limestones, with trace amounts of shale and sand. The Anahuac Formation is approximately 2700 ft (820 m) thick and thickens downdip to local thicknesses of greater than 3500 ft (1065 m).

The **Frio Formation** underlies the Anahuac formation and consists of sands and shale representing a variety of marginal marine and deep marine environments (Wilson and Noel, 1983). Jackson and Galloway (1984) describe the depositional environment of the upper part of the Frio Formation as a combination of two major delta systems and an interdelatic wave-dominated shore-zone system, all fronted by the shelf margin and continental slope. They define three paleomargin sequences that display depositional and structural features typical of an unstable progradational margin. The lower part of the Frio is composed primarily of bathyal shales deposited on the continental slope. The structural setting during deposition included the development of major bounding growth faults and deep rooted salt domes. In the Vinton Dome area, the middle Frio is absent as a result of being cut out by the Hackberry unconformity.

The **Hackberry wedge** (Figures 1.1.7 and 1.1.8) is a deep-water marine wedge that cuts the Frio and extends from the eastern flank of the Houston delta system into western Louisiana. The Hackberry consists of a lower sequence containing sands and an upper transgressive sequence dominated by shale. The Hackberry unconformity is related to both sea level drop and to uplift, folding, and erosion, related to salt movement. The Hackberry unconformity displays considerable channeling and local truncation of underlying Frio section with relief that exceeds 1000 ft (600 m). Hackberry sandstones occur mainly within the incised canyons and are a current exploration target. One of the major factors controlling Hackberry deposition is the presence of paleohighs related to differential loading and sediment ponding, associated with salt withdrawal.

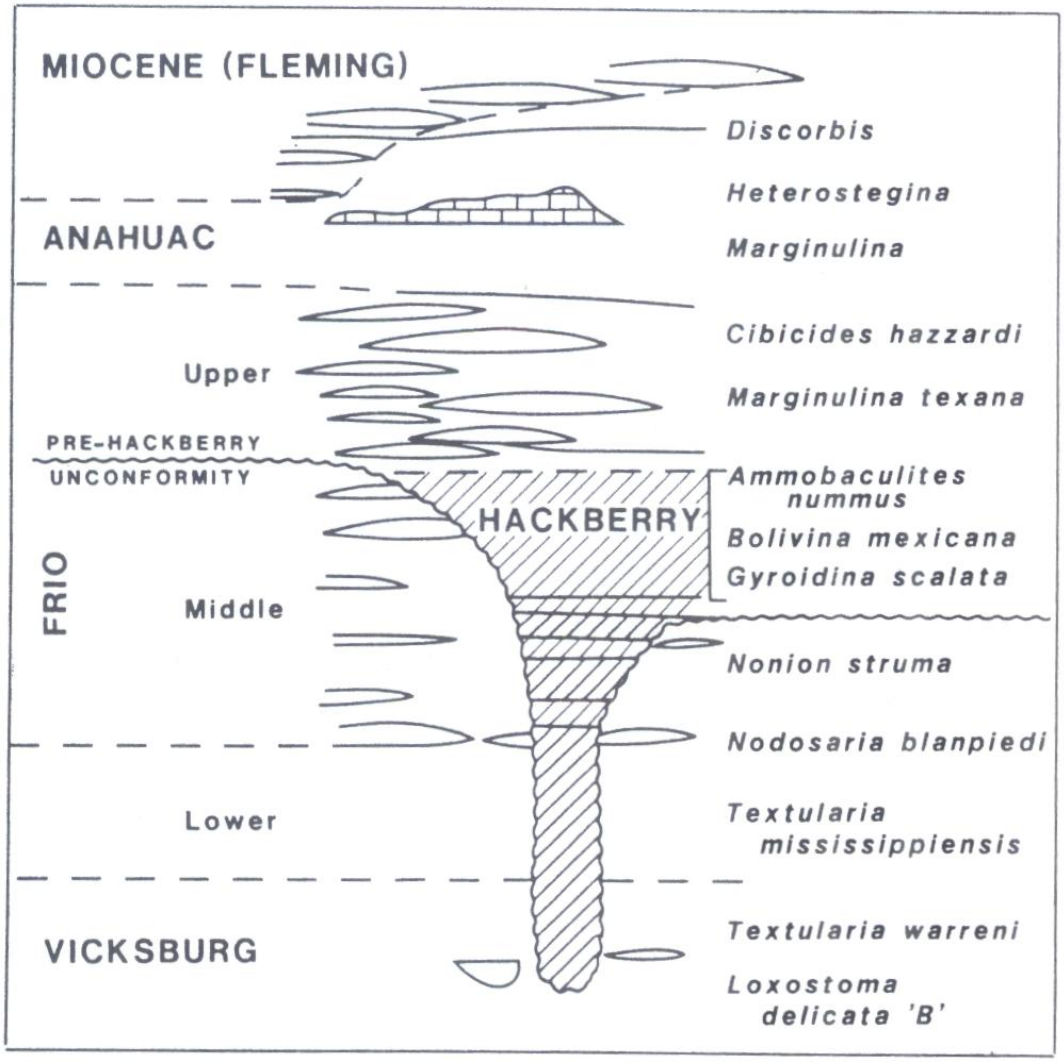

Figure 1.1.7. Productive sandstone reservoirs were deposited within upper Oligocene lowstand submarine Hackberry channels (after Eubanks, 1987). One such channel occurs within the Vinton Dome survey.

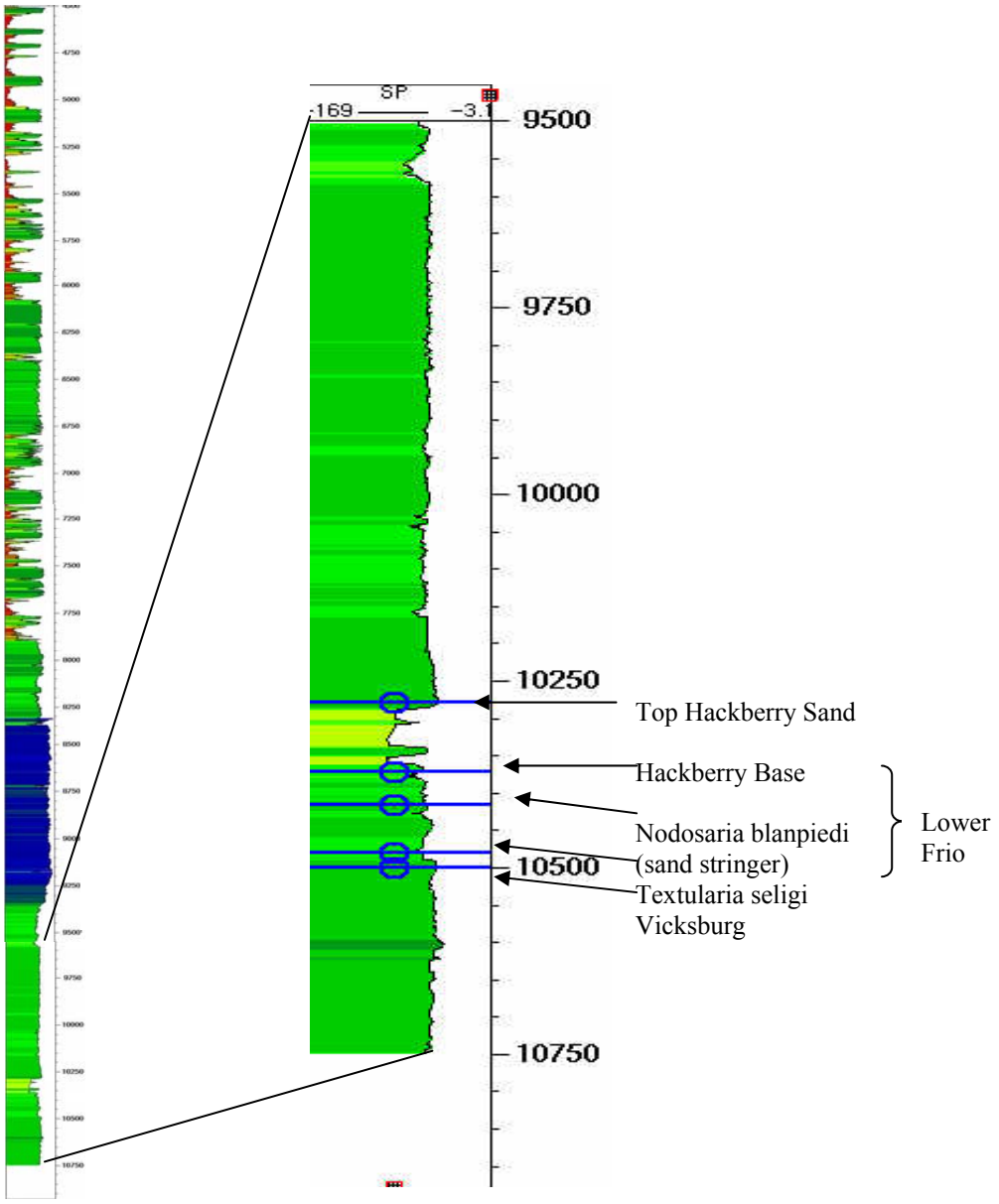

Figure 1.1.8. Spontaneous potential log of the Oligocene section from a Vinton dome well showing the transgressive phase from the Vicksburg through the lower Frio and the unconformable Hackberry channel sands. The logs are inversely color filled (from Duncan, 2005).

The **Vicksburg Formation** is consists of dark-gray to brown, fossiliferous and calcareous marine shales of early Oligocene age. The strata vary in thickness from 200 ft (60 m) to more than 300 ft (90 m).

The upper Eocene **Jackson Formation** lies below the Vicksburg and regionally consists of dark marine shale. No local thickness information is available, since no wells have penetrated this interval at the present time.

Salt Tectonics

Salt tectonics exerted a major control on the Cenozoic depositional environments and associated sand body geometries at Vinton dome. Salt bodies are generally stratiform and sub horizontal before flow. Due to low density and low yield strength, salt will flow in the solid state due to gravity alone. Factors influencing salt flow are temperature, pressure, and the presence of impurities. Water will increase diffusive flow and non-evaporite impurities will reduce plasticity and can cause a salt pillar to form a mushroom shape. Evolution of salt structures generally proceeds from concordant low-amplitude salt anticlines, rollers and pillows to discordant high-amplitude diapiric salt walls, stocks, nappes, detached teardrop units, and ultimately, to salt extrusions (Figure 1.1.9). Salt flow can stop or reactivate at any time in this developmental sequence (Jackson and Talbot, 1986). Salt in the vicinity of Vinton Dome had already formed paleohighs by the time of Hackberry deposition. At Hackberry time Vinton Dome was a diapiric feature and belonged to an east-west trending line of salt domes, connected by a large regional,

down-to-the-basin normal fault (Le Vie, 1986). Structure on the Hackberry indicates a strongly extensional regime and continued diapirism.

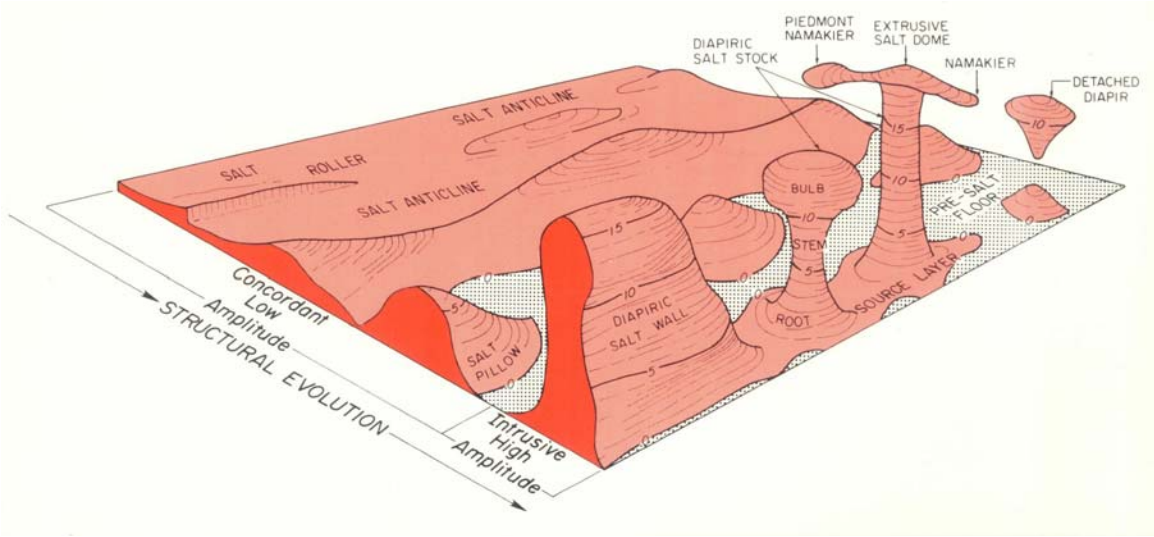

Figure 1.1.9. Evolution of salt structures from concordant low amplitude salt rollers and anticlines to intrusive high amplitude structures (after Jackson and Talbot, 1986).

A salt diapir is a salt body that has either pierced or appears to have pierced the overburden; a salt dome is a diapir and its surrounding arched strata (Jackson and Talbot, 1986). Diapirs can be classified into three types: reactive, active, and passive. Reactive diapirs initiate and grow under grabens formed by extension of the overburden. Active diapirs rise by pushing aside thinned overburden, and passive diapirs form by "downbuilding" that results from differential sinking of unconsolidated water-saturated overburden until the overburden becomes denser than salt. The Vinton salt dome was an active diapir at least through deposition of the Hackberry and the lowermost part of the upper Frio. Structural interpretation by Duncan (2005) indicates that during the older Pre Hackberry stages, the salt mass at Vinton Dome grew by passive diapirism, associated with loading of salt by sediments with contrasting densities. The salt tectonic style

changed to active diapirism by time of deposition of the upper Frio, and back to passive by time of deposition of the Anahuac.

Salt Structure Fault Patterns

The salt activity and its impact on the structural evolution in the Gulf area have been studied since the early 1960's. Fails (1990) proposed a fault pattern classification for salt structures based on the analysis of over 200 salt domes in the coastal basin area offshore Texas and Louisiana. He considers three groups: Single or multiple offset, Compensated, and Crossed Offset, shown in Figure 1.1.10. He also grouped the salt domes in three classes: penetrant (shallow piercement), semipenetrant (intermediate piercement), and nonpenetrant (deep-seated), displayed in Figure 1.1.11.

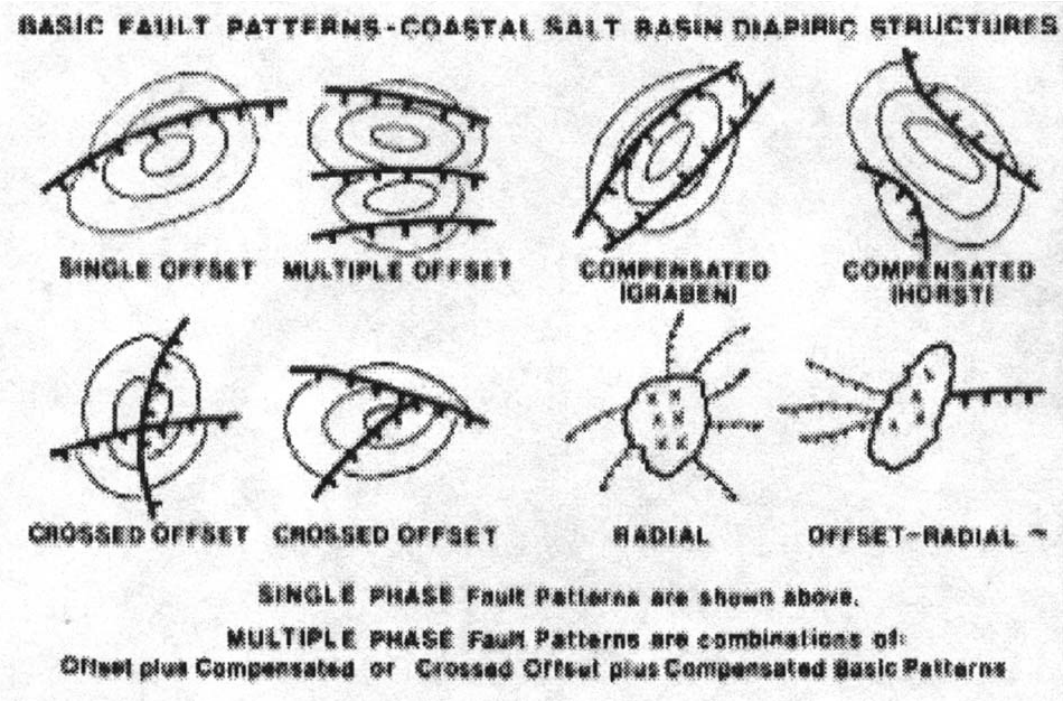

Figure 1.1.10. Fault pattern classification for Coastal Salt Basin diapiric structures, including salt domes (after Fails, 1990).

Fails (1990) indicated that penetrant and semipenetrant salt domes are heavily faulted with complex fault patterns. He found that penetrant and semipenetrant domes reveal similar characteristics such as counter regional or counter basinal faulting, and that radial faults are specific only to penetrant domes. The basic single phase fault patterns are:

Offset: one or more semi parallel major faults downthrown in the same direction.

Compensated: two or more semi parallel major faults downthrown in opposite directions, to form a graben or a horst.

Crossed offset: two or more major faults in crossed orientation.

Multiple phase fault patterns consist of combinations of superimposed offset plus compensated or crossed offset plus compensated single phase patterns. The less common **radial** pattern is restricted to penetrant salt domes, while the relatively uncommon **offset radial** pattern can occur on any salt dome type. Figures 1.1.12-1.1.15 show faults associated with Vinton Dome.

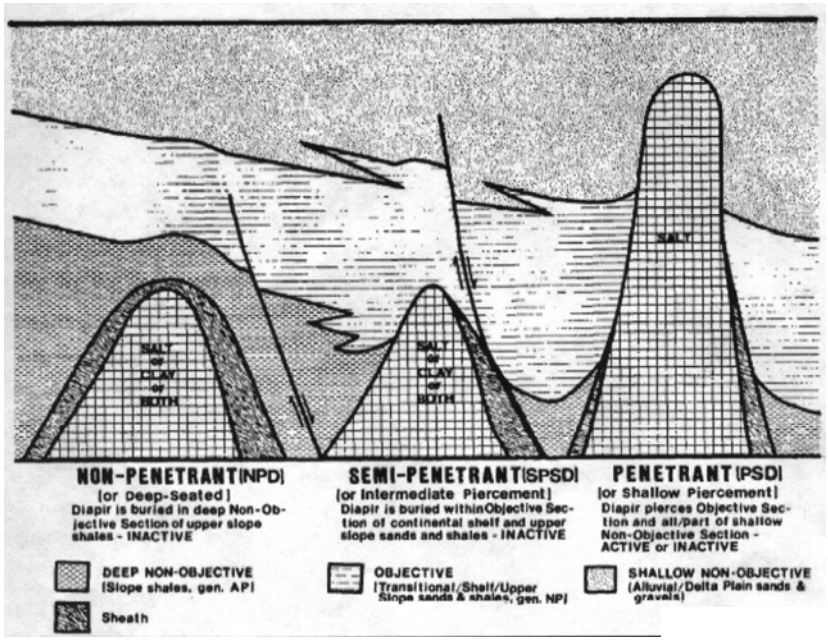

Figure 1.1.11. Salt dome classification (after Fails, 1990)

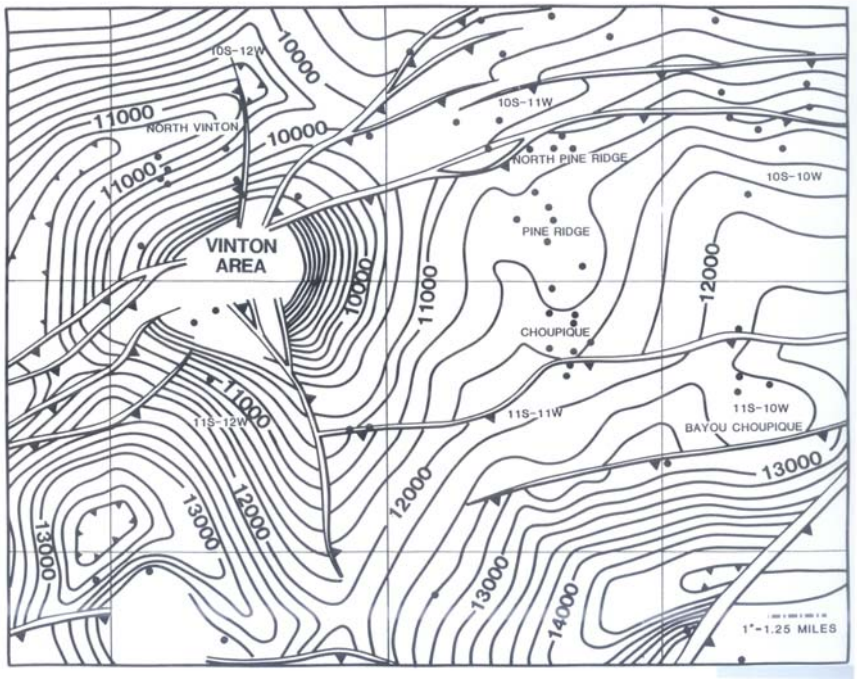

Figure 1.1.12. Structure map contoured to the lower Hackberry showing linking regional faults and depressions that represent salt withdrawal features (from LeVie, 1986)

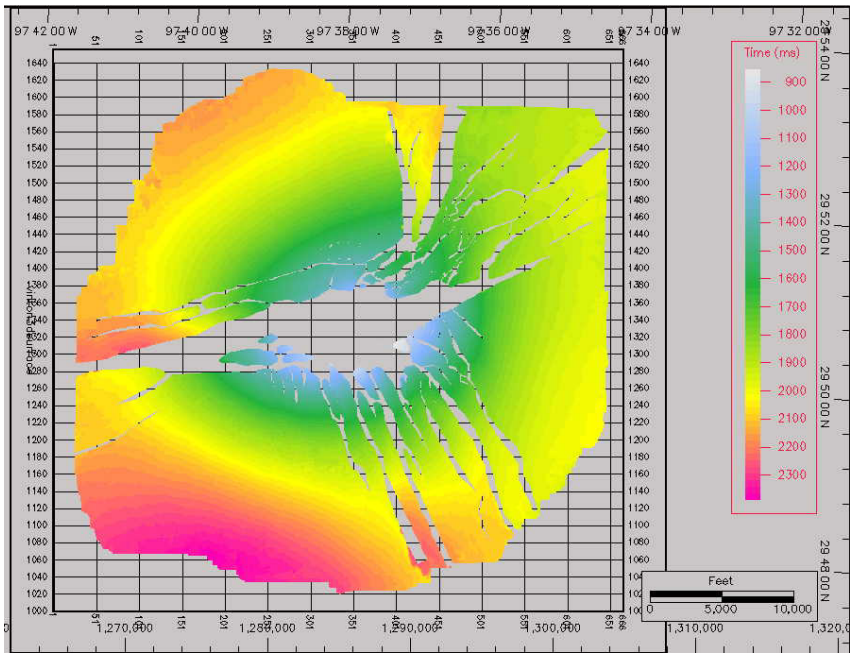

Figure 1.1.13. Structure on the A-Sand of the upper Frio. The large fault cutting through and extending beyond the dome indicates active diapirism (from Duncan, 2005).

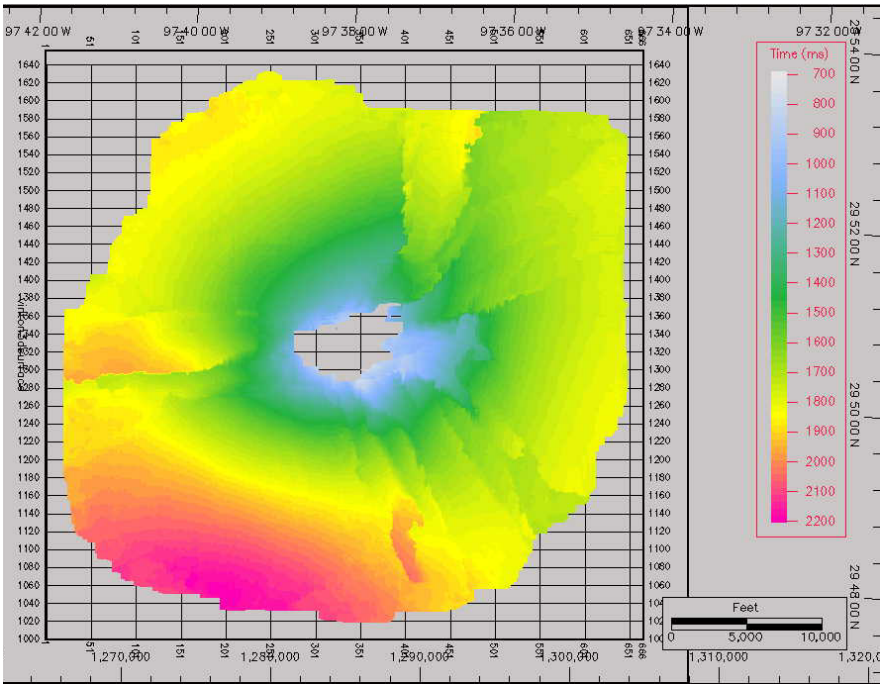

Figure 1.1.14. Radial faults visible in the map of structure on top Anahuac indicate penetrant but passive diapirism (from Duncan, 2005).

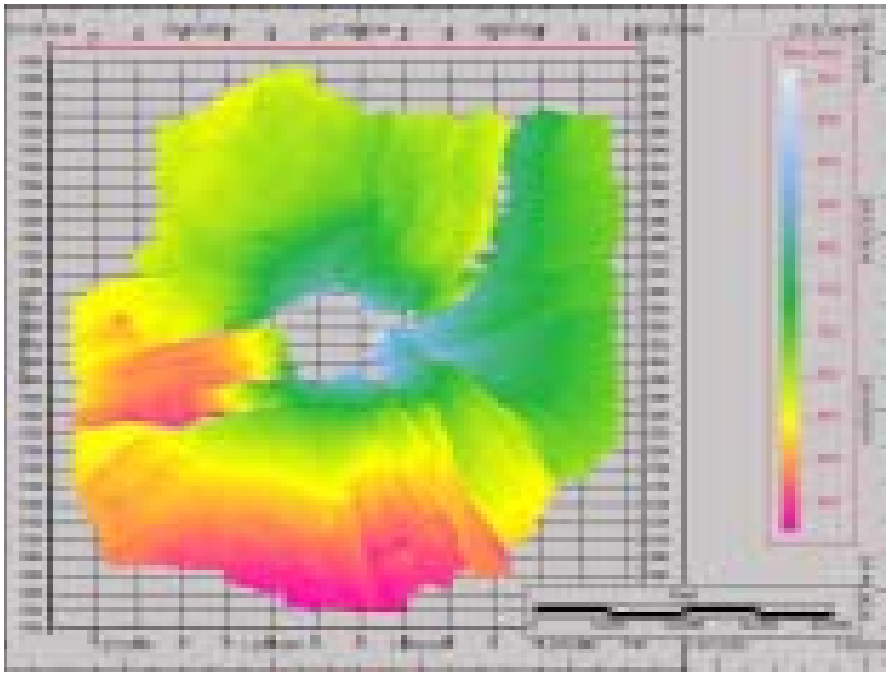

Figure 1.1.15. Structure on the main upper Miocene sand shows that passive diapirism continued through late Miocene (From Duncan, 2005).

2.0 EXPERIMENTAL

Improving poor image fidelity (correct spatial placement and resolution of seismic events) was a chief motivation for this study. We addressed the image fidelity problem through experiments in reflection tomography, VSP processing, physical and numerical modeling, and depth migration.

2.1 3-D 3-C VSP Data Processing

A 3-C VSP measures the complete seismic wavefield (down-going, up-going, and horizontally-traveling P- and S-waves) in the subsurface and is therefore an ideal tool for a detailed stratigraphic and lithological interpretation (Ahmed et al., 1986; Ahmed, 1987, 1990). Simultaneous acquisition of surface 3-D and subsurface 3-C VSP data provides a comprehensive data set for imaging the subsurface. Since no extra sources are used, this method was considered to be a cost-effective means to acquire 3-D VSP data. However, the subsurface sampling associated with the VSP is quite different from that associated with the surface seismic data. After our analysis, we believe that considerable shot infill would result in a better, unaliased subsurface image. The combination of surface seismic and VSP also provides an opportunity to add extra control for the determination of seismic velocities (Constance et al., 1999) and estimate the source wavelet. Because the location of the salt was well known, the Vinton Dome acquisition program used a radial receiver grid on the surface, two multilevel downhole 3-C arrays, and concentric source lines (Figure 2.1.1).

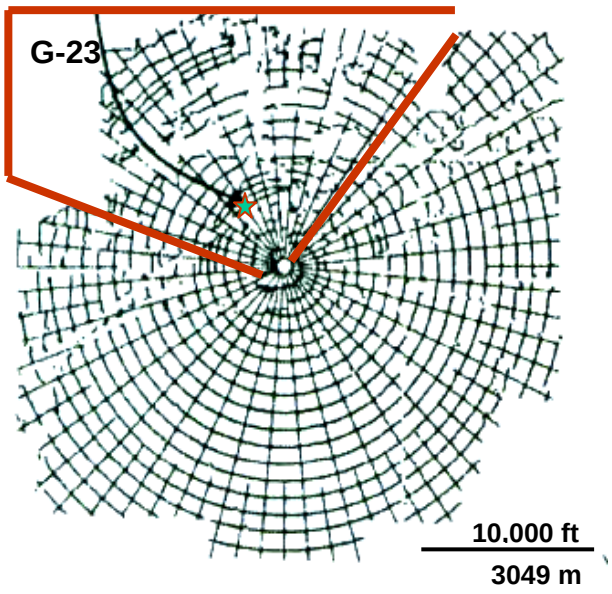

Figure 2.1.1. Seismic acquisition at Vinton Dome. Receivers are along radial lines, sources on concentric arcs. The VSP in well G-23 used sources included in the shaded polygon (after Constance, 1999).

The polygon in Figure 2.1.1 indicates the sources recorded by the 3-C geophones in well G-23. Source locations are approximated by concentric circles, with shot spacing 165 ft along an arc. The seismic sources consisted of 5.5 lb. pentolite charges set off at 60 ft. depth (18 m). The receiver line interval on the surface is variable, ranging from approximately 900 ft to 1200 ft (275 to 365 m), with alternating long and short line segments spaced at 5° increments. The receiver station spacing is 165 ft (50 m) along a receiver line segment. At each station, a 6 element array was deployed using 10 Hz geophones. Cultural obstacles in the northern and western portions of the survey area, including houses, wells, canals, pipelines, and the four-lane US Interstate 10, produced irregularities from the original planned source grid.

The active recording spread consisted of 19 receiver lines, which represents a 90° wedge of the 360° coverage produced by the radial receiver line distribution. Typically, 1400 to 2000 channels were active in the surface spread.

While the approximate northern half of the surface seismic survey was acquired, two abandoned boreholes were used to deploy 3-C arrays in the subsurface. Well G-23, has 80 levels of 3-C geophones cemented in place at 50 ft (15.24 m) spacing, located between 943 and 4893 ft (287 to 1492 m). The last 19 groups were damaged during deployment and were not operational for recording. Figure 2.1.2 shows the map view of the 1176 sources recorded by G-23, as generated in Seisup. Sources are color-coded based on shot depth. The size of the survey is around 18700 ft (5702 m) NS and 30000 ft (9147 m) EW.

Deconvolution and rotation of horizontal geophones

Deconvolution, the process of convolving with an inverse filter (Sheriff and Geldart, 1995) has two goals – (1) to shape the wavelet and balance the frequency bandwidth, and (2) to suppress multiples. For VSPs, we calculate the deconvolution operator from the down-going waves (Hinds et al., 2001). In this process we first pick the first arrivals on a common-shot gather, then flatten the first arrivals, then apply a median filter to enhance the down-going waves and suppress the up-going waves. Finally, we sum all the traces to generate a statistically robust wavelet.

Accurate geophone orientation is essential in multicomponent seismology, since this allows separation of P- from S-waves (Guevara and Stewart, 2001). Usually, gyroscopes are not used to determine downhole orientation of the horizontal phones. In certain cases where we carefully deploy geophones down hole, we may assume a predefined geophone orientation. Alternatively, we may obtain the orientation directly from the field data, which was the case at Vinton Dome. Polarization of first arrivals has been used successfully to obtain geophone orientation in both VSP (DiSiena et al., 1984), and marine multicomponent data (Gaiser, 1999). For this study, we followed DiSiena et al. (1984) and selected a hodogram method to orient the data. We displayed the terminus of a moving vector as a function of x, y and time, allowing for the simultaneous analysis of amplitude, polarization and relative orientation.

Separation of up-going and down-going events

One important step during VSP processing is the separation of up-going and down-going events. The down-going waves are used to extract the source wavelet necessary for deconvolution of the upgoing waves. Normally, in the case of a horizontal or slightly dipping layered medium, all reflections from the subsurface boundaries are up-going events. In this case, separation of the wavefield into up- and down-going events is appropriate (Foster and Mosher, 1988; Moon et al., 1986).

At Vinton Dome, our case is different. The subsurface structure is steeply dipping and highly faulted. We are also very interested in imaging reflections from the salt flank. To understand more about the implications in seismic wave propagation in the presence of steep dips, we performed a modeling study (Hoelting et al., 2003b). This study was based

on a previous model built using a 2-D dip line through the time migrated seismic volume obtained from the surface data (Hoelting et al., 2002, 2003a). The dip line is oriented NW-SE including the well G-23 and the center of the salt dome (Figure 2.1.2).

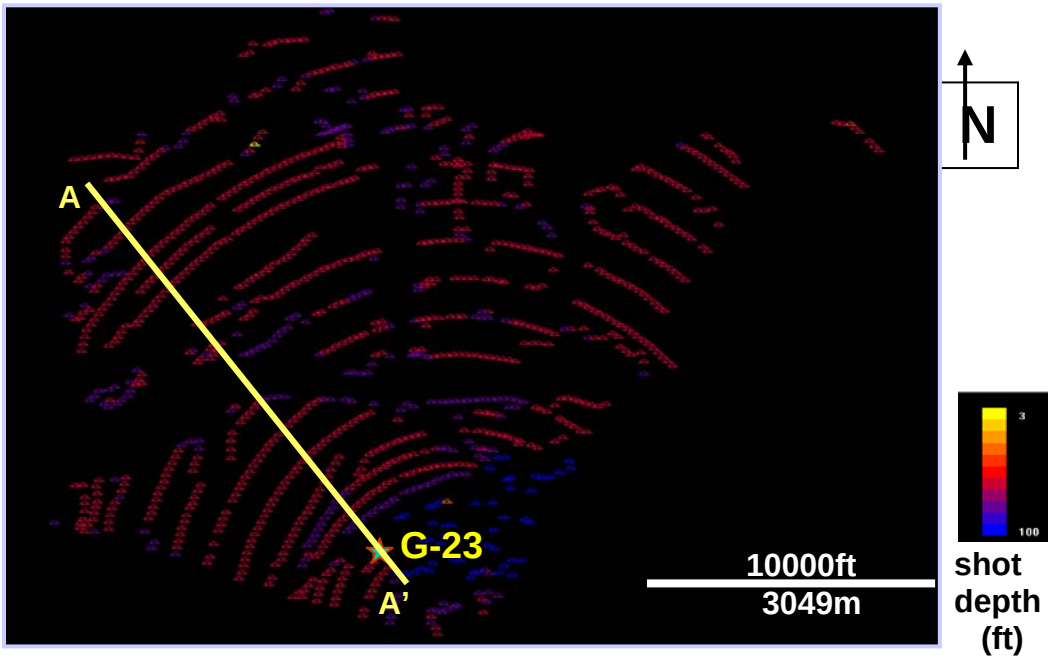

Figure 2.1.2. Mapview of sources recorded in well G-23. AA' represents the 2-D dip line selected from the 3-D time-migrated surface data to generate the depth model.

There are more than 500 wells in this area, which provide formation tops, and helped identify horizons and salt in the 3-D time migrated surface data (Figure 2.1.3). The picks shown in Figure 2.1.3 were exported in ASCII format and then imported into the seismic modeling software, GX-II. Interval P-wave velocities were calculated from check-shot velocities. We then used Castagna's equations to estimate S-wave velocities and densities. No velocity gradient has been applied. We then used these velocities to convert the time horizons from Figure 2.1.3 to depth horizons displayed in Figure 2.1.4.

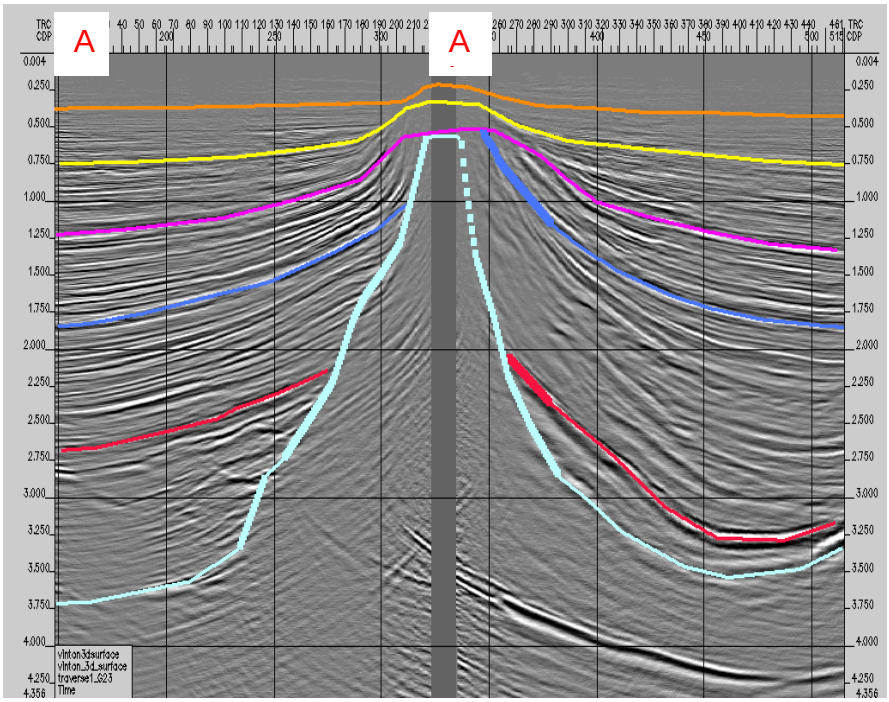

Figure 2.1.3. 2-D vertical seismic section along the dip-line. Picked horizons are displayed in color: Upper Miocene (orange), Upper mid-Miocene (yellow), Mid-Miocene (purple), Frio A sand (blue), Hackberry (red), and Salt (light blue).

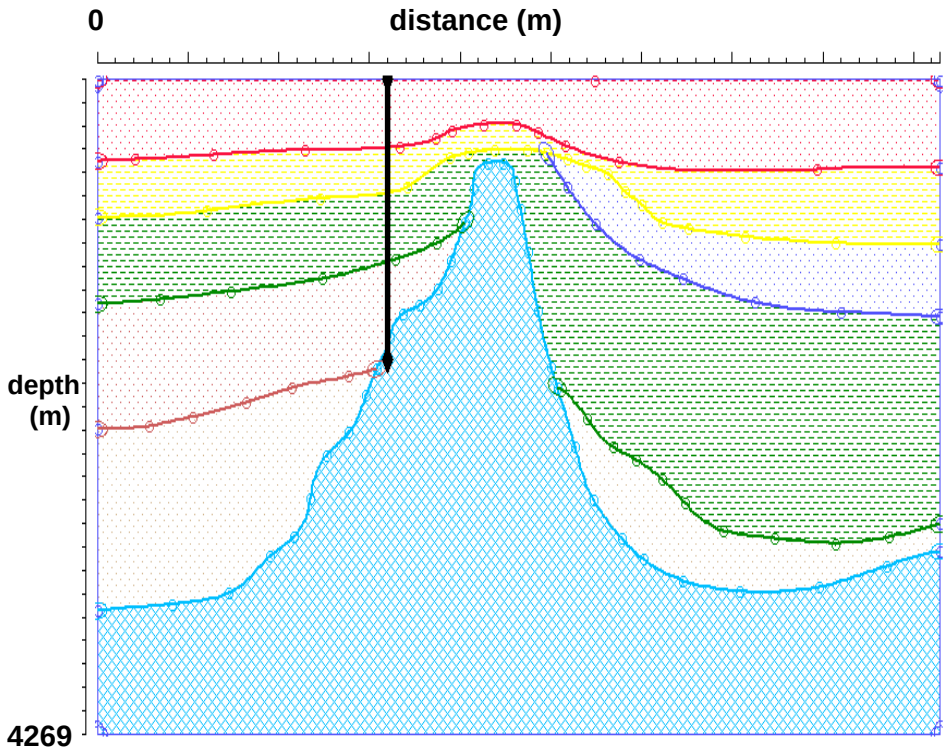

Figure 2.1.4. 2-D depth model generated in GX-II based on the time horizons displayed in Figure 2.1.3.

Although the salt flank has been picked on the time migrated data and there are uncertainties regarding the correct location, we can assume that our model is accurate in some part. We have information that the VSP well entered in salt around depth of 6000 ft (~1830m), which helped us to calibrate the model. Sources were placed 60 ft (18.3 m) below the top-boundary of the model and 61 receivers were placed in the well. Common-shot gathers for vertical and horizontal components were generated in GX-II.

The modeling results indicate that the salt reflection is composed of both, up-going and down-going events such that the separation into up and down-going waves is inappropriate. Since the goal of our project is salt flank imaging, the entire information available in the data is needed.

Another interesting observation is that PP events from the salt flank are better observed on the horizontal component and PS events on the vertical component. This observation contradicts the conventional supposition that PP reflections are observed mainly on the vertical phone and PS reflections on the horizontal phone (Figures 2.1.5 – 2.1.8).

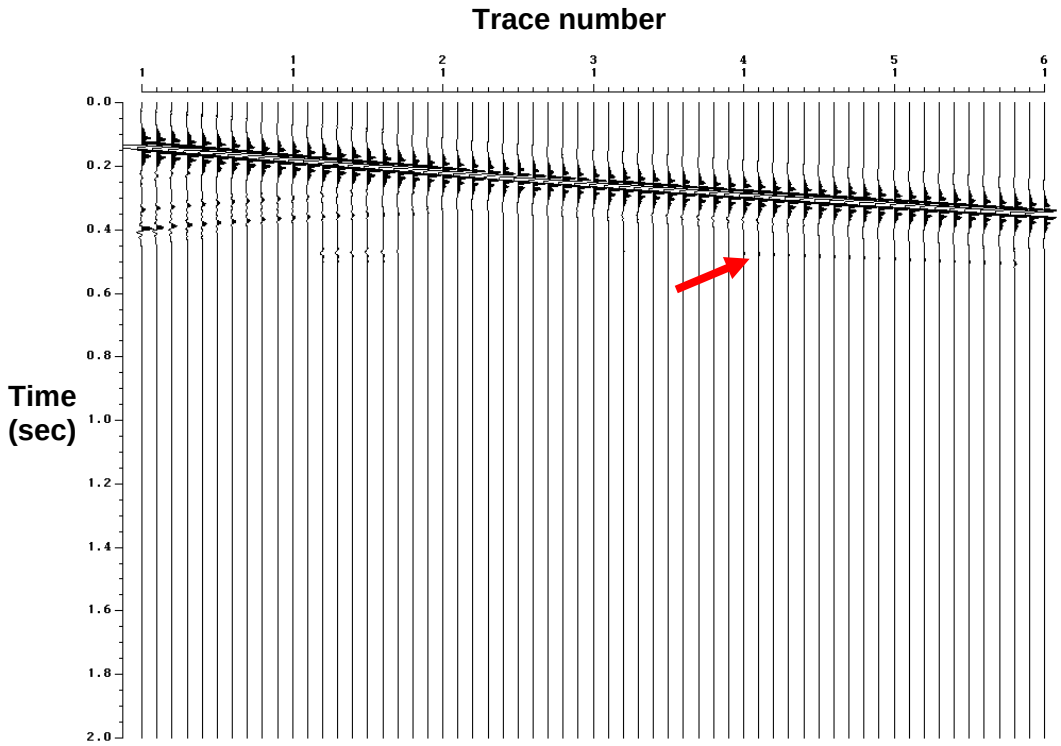

Figure 2.1.5. Near offset common-shot gather vertical component (P and PP events only). Note the weak PP salt reflection on the deeper traces around 0.5 seconds (red arrow).

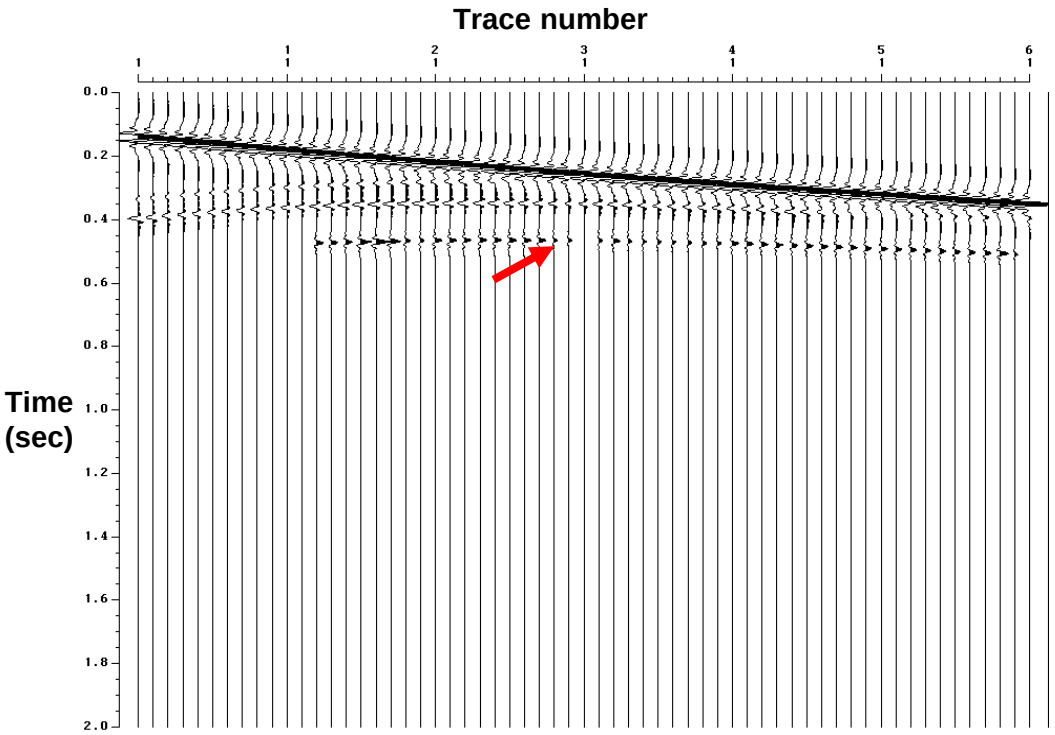

Figure 2.1.6. Near offset common-shot gather horizontal component (P and PP events only). Note the strong PP salt reflection around 0.5 seconds (red arrow).

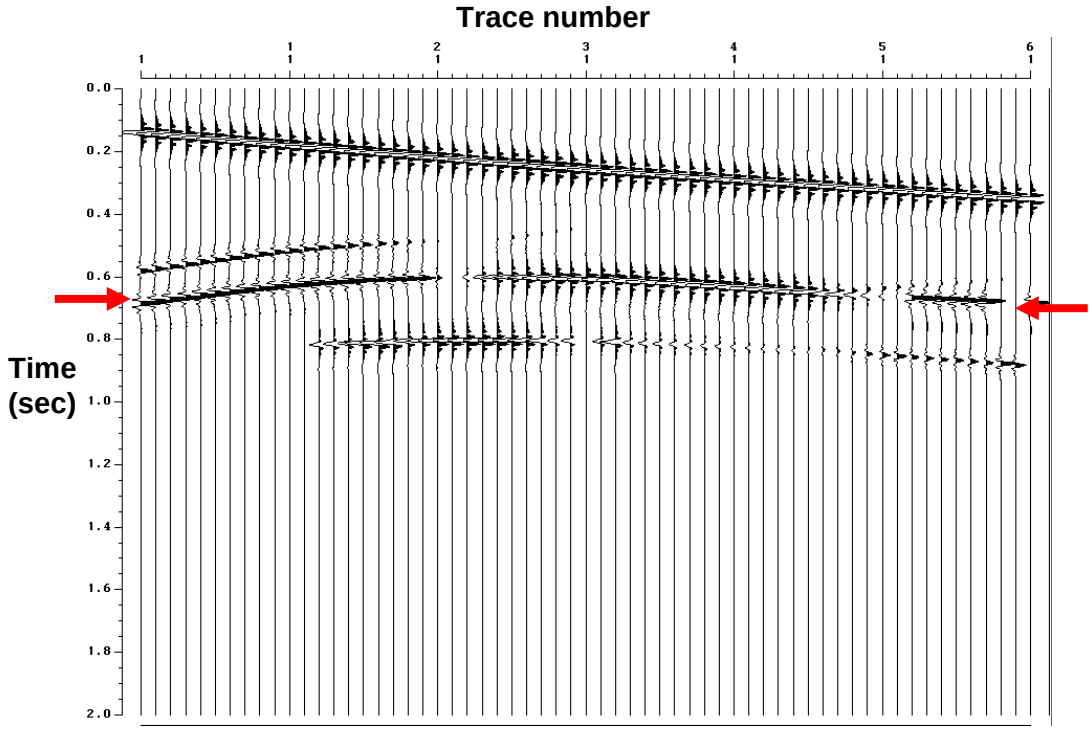

Figure 2.1.7. Near offset common-shot gather vertical component (P and PS events only) Note the strong PS salt reflection coming around 0.7 sec (red arrows).

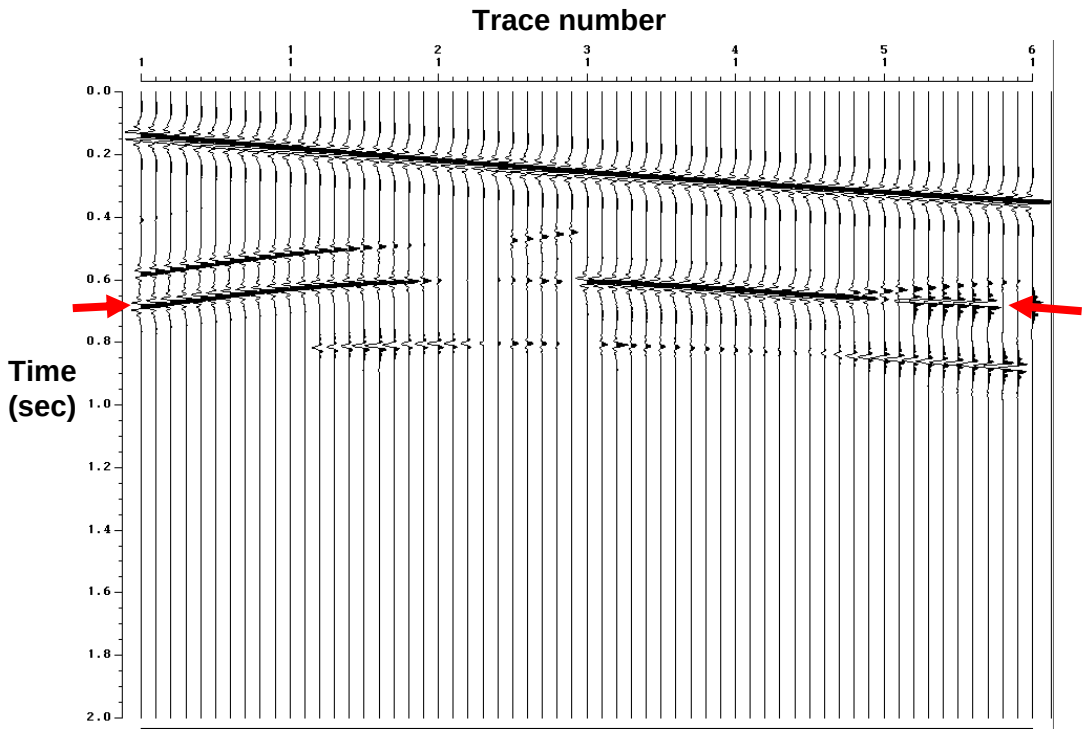

Figure 2.1.8. Near offset common-shot gather horizontal component (P and PS events only). Note the weak PS salt reflection at about 0.7 sec (red arrow).

2.2 Numerical Modeling

In addition to the raytraced synthetics presented at the end of the previous section, we conducted 2-D and 3-D finite difference modeling. This type of numerical modeling more faithfully approximates wave propagation in the earth and thus provides a more rigorous calibration suite for our processing and imaging algorithms. The next two subsections describe the 2-D elastic finite difference modeling and the 3-D acoustic pseudospectral modeling, respectively.

2-D Numerical modeling

We ran several 2-D multicomponent VSP finite difference synthetics over a radial line connecting one of our wells with 3-C VSP data (G-23) and the center of the salt dome, in order to better study wave propagation phenomena, and to calibrate our polarization

filtering, migration, and tomography algorithms. This effort was undertaken as a classroom effort in our graduate level Seismic Modeling class, where we compared and contrasted the information content provided by ray theoretical modeling, acoustic FD, and elastic FD. During this time we also installed LLNL's E3D algorithm on the UH HPC Sun cluster, and tested and verified that the code worked correctly in scalar mode. We constructed 3-D acoustic and elastic models to help calibrate our processing and imaging strategies.

We also investigated the way in which energy reflected from steeply dipping interfaces is recorded, using multicomponent acquisition. Specifically, we analyzed the way in which reflection events from the flanks of salt structures are distributed on 3C geophones for VSPs. The ultimate goal of this part of the investigation is to improve the structural imaging of steeply dipping interfaces and eventually to evaluate the use of the recorded elastic wavefield for fluid description near these interfaces. We focused on a common assumption used when processing converted-wave reflection seismic data: that most PP energy is recorded on the vertical geophone and/or the hydrophone and that most PS energy is recorded on the horizontal geophones. This is a useful assumption when it is valid, because it eliminates the need for separation of the recorded wavefield into P and S wave types. Using two elastic models, we examined the validity of this assumption in the presence of steeply dipping interfaces. The results of our modeling study contain two important implications for converted-wave/vector VSP salt flank imaging. Firstly, the salt flank reflections can closely parallel reflections from horizontal interfaces, as seen in the 2D SEG/EAGE salt structure, and often contain both upgoing and downgoing energy.

Therefore, we must take great care not to remove this reflected energy in preprocessing before migration. Secondly, most PP reflection energy is recorded on the horizontal component for vertical interfaces and on the vertical component for horizontal interfaces and vice versa for PS reflections.

3-D VSP subsurface illumination through acoustic pseudo-spectral modeling

The final part of the VSP subsurface illumination study consists of modeling 3D acoustic VSP data via an in-house 3d acoustic pseudo-spectral modeling algorithm. Gherasim (2005) built a 3-D P-wave velocity model that resembles the 2-D velocity model used in the previous modeling. Unlike the commercial 3-D ray-tracing software our wave equation modeling algorithm allows us to model the exact same source and receiver geometry extracted from the Vinton VSP field data.

Gherasim (2005) obtained good illumination of sedimentary interfaces and salt flank (Figure 2.2.1). However, only the portions of the sediment reflected wavefield located closer to the VSP well are recorded, which basically minimizes the amount of information received from the sedimentary boundaries.

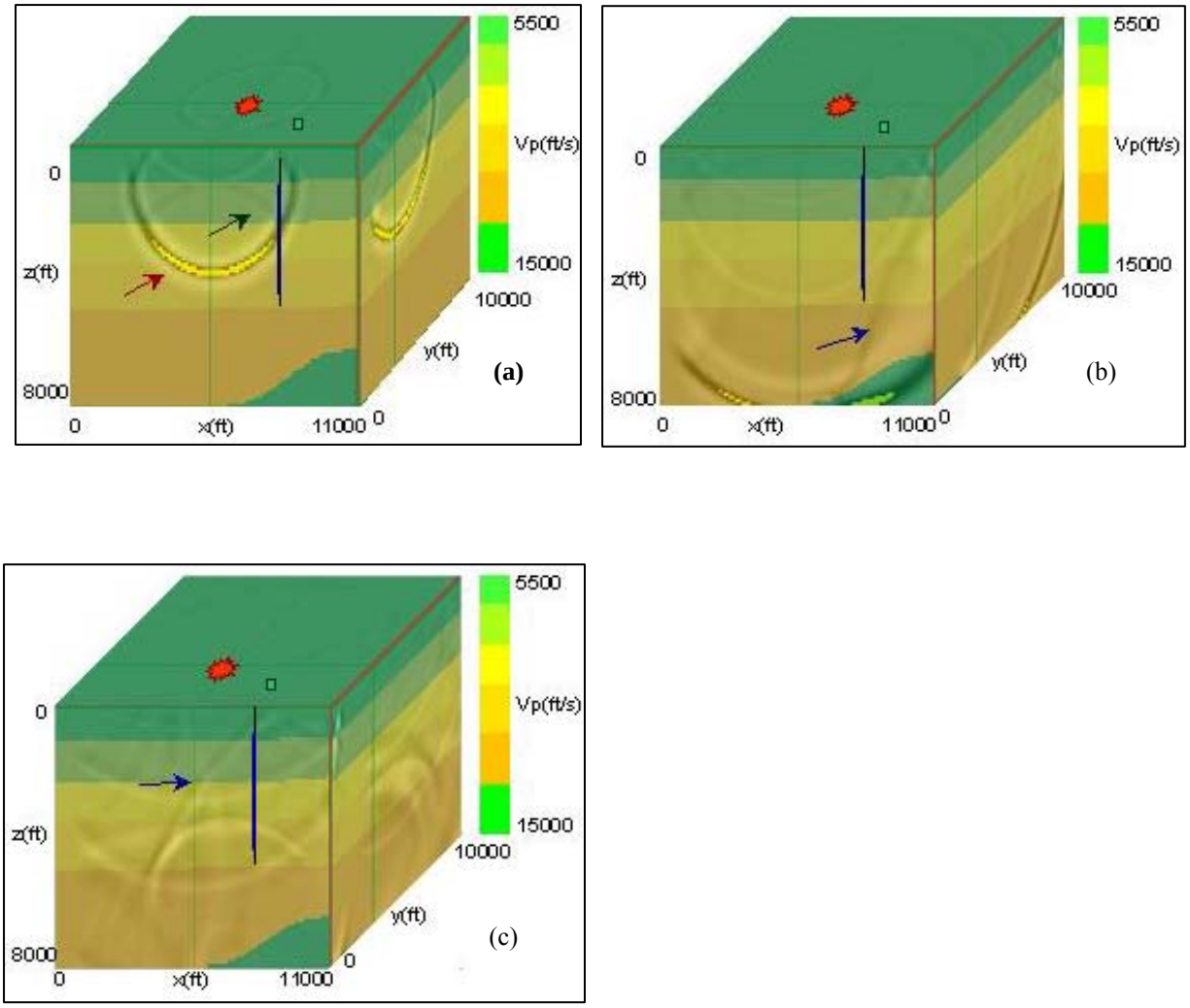

Figure 2.2.1. 3-D P-wave snapshots recorded at 0.5 sec (a), 1.0 sec (b), and 1.5 sec (c). Red star marks the shot location, green dot marks the surface location of the well, and dark blue line marks the VSP receiver array. The dark red arrow marks direct P wavefield, the dark green arrow marks the sediment PP reflections, and the dark blue arrow marks the salt PP reflections. (From Gherasim, 2005).

2.3 Separation of P- and S- waves using antialias vector Radon transforms

We applied high resolution discrete Radon transform algorithm on the one second of the recorded and rotated radial and vertical component from the shot 3068 from the Vinton Dome 3-D 3-C VSP data (Figure 2.3.1). Mathematical details of this method can be found in Javanovic and Marfurt (2005). As we can see from the obtained results (Figure 2.3.2), only the strongest events, i.e. downgoing events are partially modeled.

To allow modeling of all events, we have applied amplitude balancing and muting to the input shot gathers (Figure 2.3.3). To balance the data, we multiplied each sample by t^4 event such that early and late events of a seismogram have similar amplitudes. Such a deterministic gain can easily be removed by multiplying the result of filtering by t^{-4}. We muted all events to be zero before the first arrival. The separated P and S wavefields (Figure 2.3.4) now contain all arrivals. In order to check quality of separation, we reconstructed radial and vertical components (Figure 2.3.5), and calculated residuals between the original data and the reconstructed components (Figure 2.3.6).

In order to understand the importance of applied constraints for wave mode separation, we compare three examples with different constraints parameter.

To evaluate an unconstrained vector Radon transform, we set a value of our model weights to one, $\mathbf{M}$=1. Since all events are equally favored, the separation is based on the

ray parameter and polarization only. In Figures 2.3.7a and b, we note that $\mathbf{m}_p$ and $\mathbf{m}_s$ have strong dispersion due to data aliasing.

In the next example, we apply the constraints, but allow all τ-p events to be modeled at the last iteration (Figures 2.3.7c and d).

In the final example, we maintain constraints for every iteration (Figures 2.3.7e and f).

The reconstructed P and S wavefields are shown in Figure 2.3.8. Without constraints, P wavefield (Figure 2.3.8a) and S wavefield (Figure 2.3.8b) are very poor. There are also strong edge effects. The sparsely constrained results (Figures 2.3.8c and d) have better P and S separation and there are minimal edge effects. However, the most constrained separated data (Figures 2.3.8e and f) show the most coherent arrivals.

Spatial window test

There are three approaches for τ-p filtering (Figure 2.3.9) depending on the spatial window size, i.e. how many traces from one shot are input to this algorithm:

1) Use a fixed, large spatial window, which includes all traces (Figure 2.3.9a). Unfortunately, discrete waveform discontinuities at major reflectors are not well represented by only a few τ-p parameters. In addition, the semblance estimates are weak since the wavefronts have some curvature (Figure 2.3.10).

2) Use a small trace running window, for example 11 traces. The semblance will be better, but we will still span discontinuities and have artifacts in those areas (Figure

2.3.9b). However, events are better positioned, more coherent and better separated (Figure 2.3.11).

3) Use fixed, sequential windows. Since we know velocities within the well, we can reliably estimate the major velocity breaks and form spatial windows based on this information (Figure 2.3.9c). We have divided data into four zones for the fixed, zonal window application: traces 1-17, traces 18-33, traces 34-45 and 46-61 (Figure 2.3.12). While some deeper events become most coherent with this type of spatial filtering, there are still artificial brakes and artifacts.

Offset test

We tested the algorithm on a near (shot 3060, offset 300 m), mid (shot 3068) and far (shot 3046, offset 1000m) offset data. Inputs to the algorithm are two seconds of the recorded radial and vertical component. Separated P and S wavefields for shot 3060 (Figure 2.3.13) and shot 3068 (Figure 2.3.14) have better resolution then the results obtained for the long offset data (Figure 2.3.15). However, the quality of the separation highly depends on the rotation, number of iterations, relaxation and stopping criteria.

Filtering in τ-p space

There are two ways for data filtering in τ-p space. One way is to select ray parameter values to be muted. The other way is to select a range of angles to be muted.

With a proper mute selection in the model space, one can filter the data. This is a simple way for separation of the downgoing from the upgoing VSP waves. Muting the waves

with negative ray parameters, we allowed modeling of downgoing P-waves and downgoing S-waves only (Figures 2.3.16a and b). Reversing the mute separates upgoing P and upgoing S wavefields from the downgoing waves (Figures 2.3.16c and d).

Beside downgoing-upgoing separation, we can select a certain range in the τ-p space we want to filter. In Figure 2.3.17 we passed arrivals that are more horizontal and muted steeper events. Though it is hard to select a proper mute range, this can be one of the possible methods to filter more horizontal i.e. salt dome reflections from the rest of the data. The large edge effects are due to an abrupt mute selection in the τ-p space; a taper would avoid this problem.

To better image horizontal salt dome reflections, we have filtered data based on the incidence angles ψ_p and ψ_s (Figure 2.3.18). We have selected angles -30º to +30º from the positive x-axis for the P-waves. This range is the same for the S-waves (+30º / -30º), but the filtered zone in τ-p space is larger due to the smaller velocity values. With this filtering approach we are able to extract any particular wave and to avoid strong τ-p filtering artifacts.

In summary, we have presented a new wavefield separation algorithm that uses a high resolution discrete Radon transform approach. Performed in the time, rather than the frequency domain, our Radon transform is both an antialiasing and polarization filter. The major advantages of the developed multicomponent conjugate gradient solution are: the iteration process can be stopped at any time, providing a partial solution, and the user

can specify quality of the separation giving the relaxation criteria and number of iterations.

We have shown on the real data corresponding to Vinton Dome, that our algorithm successfully separates major linear events, though with some minor leakage of one wave mode into the other. Unfortunately, this method requires the model to be a good fit to the data, and because it is a linear Radon transform, it fails to fit our hyperbolic salt reflections.

Additional problems related to a linear model approximation are 'kinks' in the VSP arrivals and projection of some upgoing events beyond transmitted downgoing wave. These problems are successfully overcome using the different spatial windows. Good results are obtained both with a running window and with a velocity based zonal window. Unfortunately, this window approach significantly increases the already high costs of the high resolution Radon transform.

Tests performed on the several different Vinton Dome shots show that quality of the obtained results depends on the preprocessing of the data. This algorithm is strongly affected by the quality of the rotation to the radial and transversal component and strength of the first downgoing arrival, such that some scaling is necessary before the algorithm application. In general, this code requires good balancing of all input parameters.

As it was expected, challenges due to the long offsets and lack of resolution remain. Separation results are better on the near and mid offsets than on the far offset data.

Using the semblance and energy driven constraints, one of the major strengths of this algorithm can be exploited for the purposes of data filtering. Once separated to the P and S wavefields, data can be filtered and separated to the downgoing, upgoing, or any wave type using the mute in the τ-p space. Unfortunately, this type of filtering may produce severe edge effects due to the mute selection. I solved this problem using an incidence angle filter, where any particular wave can be filtered based on the direction of arrival to the well in the vertical plane between a source and receiver.

Extension of this approach to include azimuthal direction for the τ-p-φ space VSP separation is going to be the next step in the high resolution discrete Radon transform algorithm development for P and S waves separation of coarsely sampled 3-D 3-C VSP data.

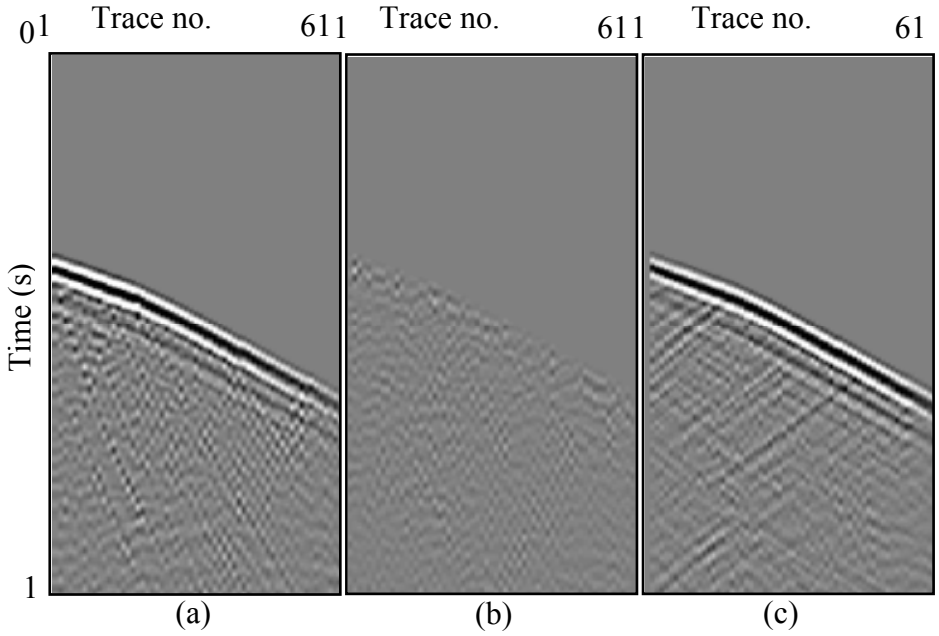

Figure 2.3.1. Radial (a), transversal (b) and vertical (c) component, shot 3068, offset 600 m.

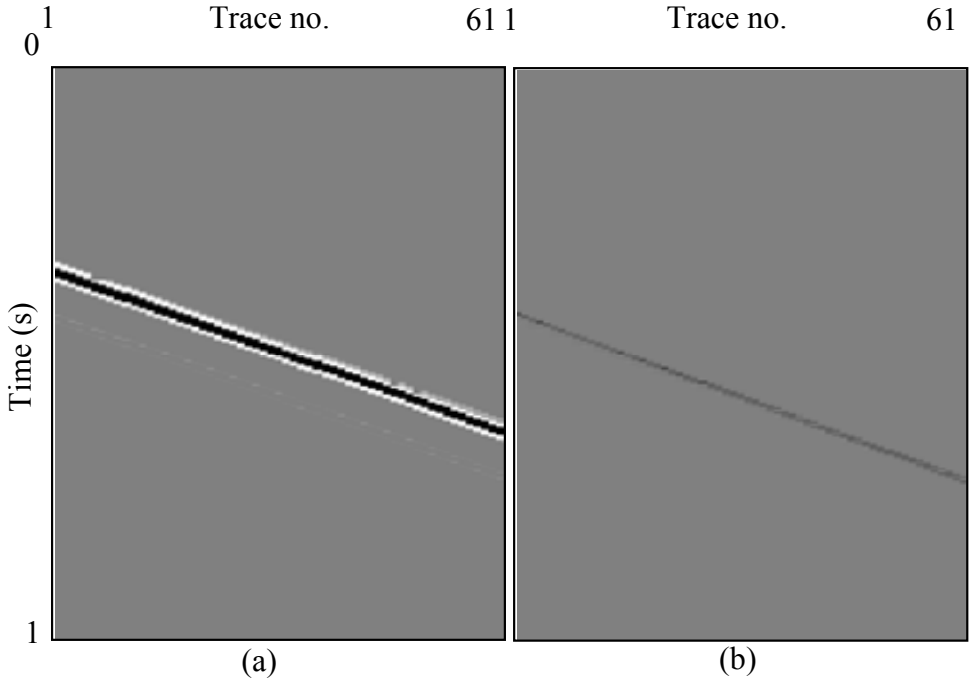

Figure 2.3.2. Separated P-waves (a) and S-waves (b) for shot 3068. Due to the strength of the first arrivals, we can not model other events.

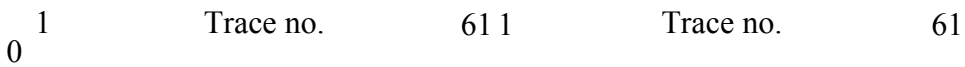

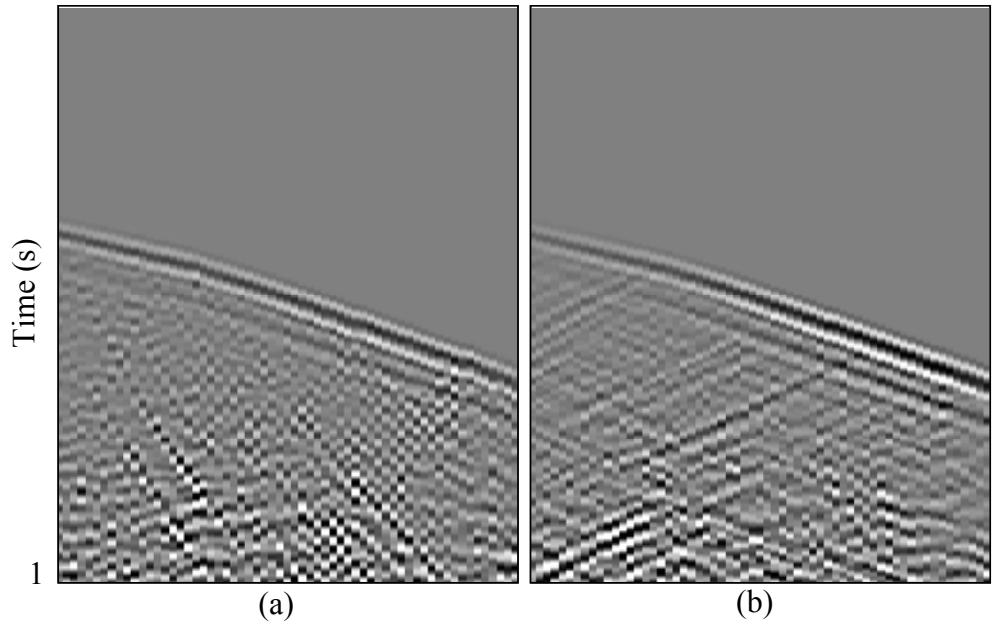

Figure 2.3.3. Scaled and muted radial (a) and vertical (b) component, shot 3068, offset 600 m.

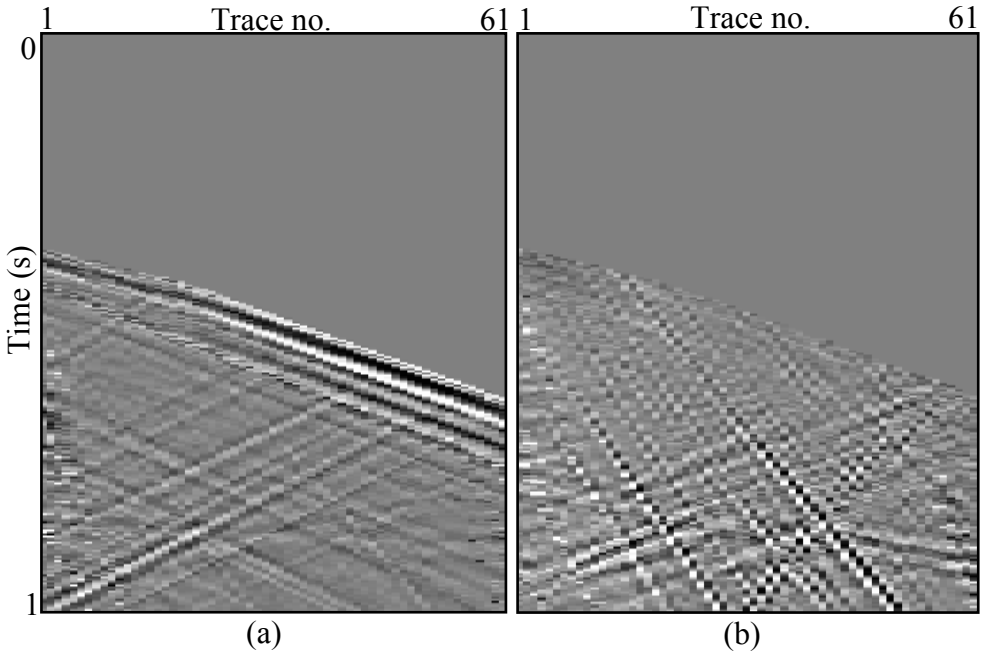

Figure 2.3.4. Separated P (a) and S (b) wavefields for shot 3068.

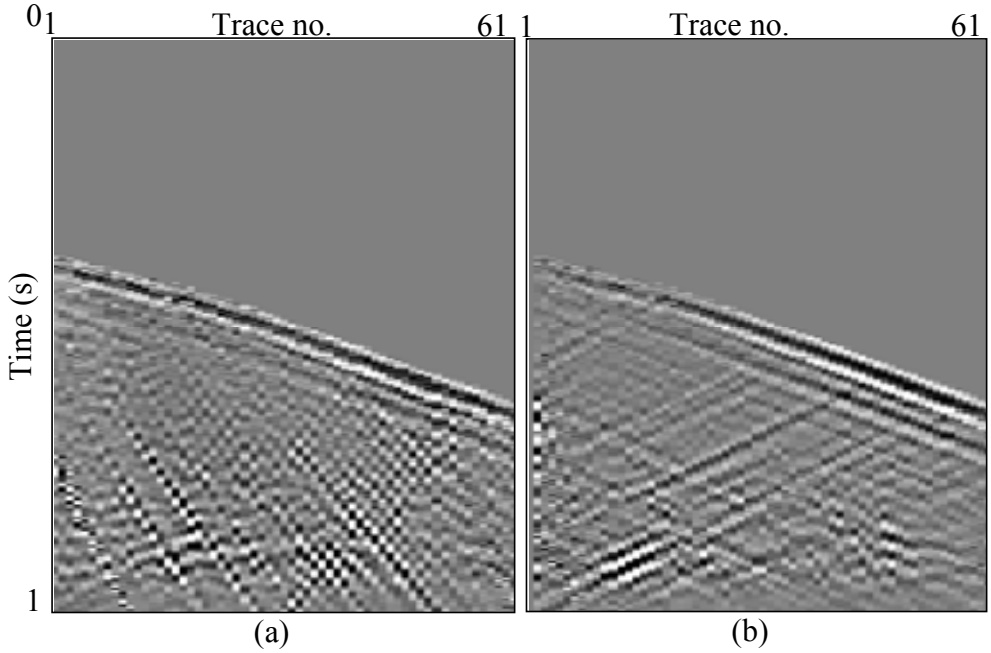

Figure 2.3.5. Reconstructed radial (a) and vertical component (b) for shot 3068.

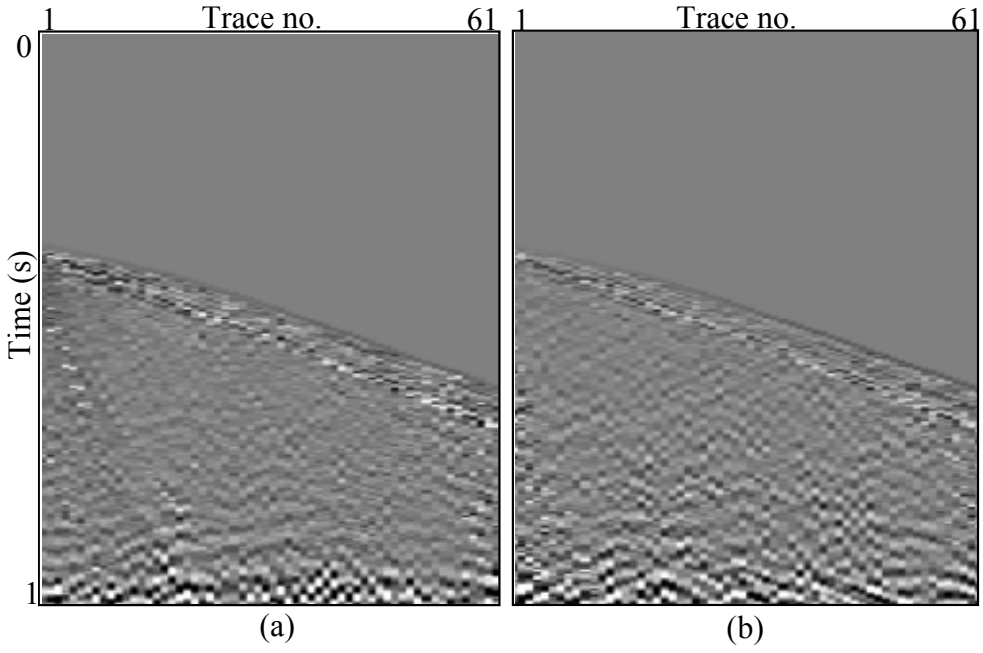

Figure 2.3.6. (a) Residual between the original (Figure 2.3.3a) and reconstructed radial component (Figure 2.3.6b) and (b) residual between the original (Figure 2.3.3b) and reconstructed vertical component (Figure 2.3.5b).

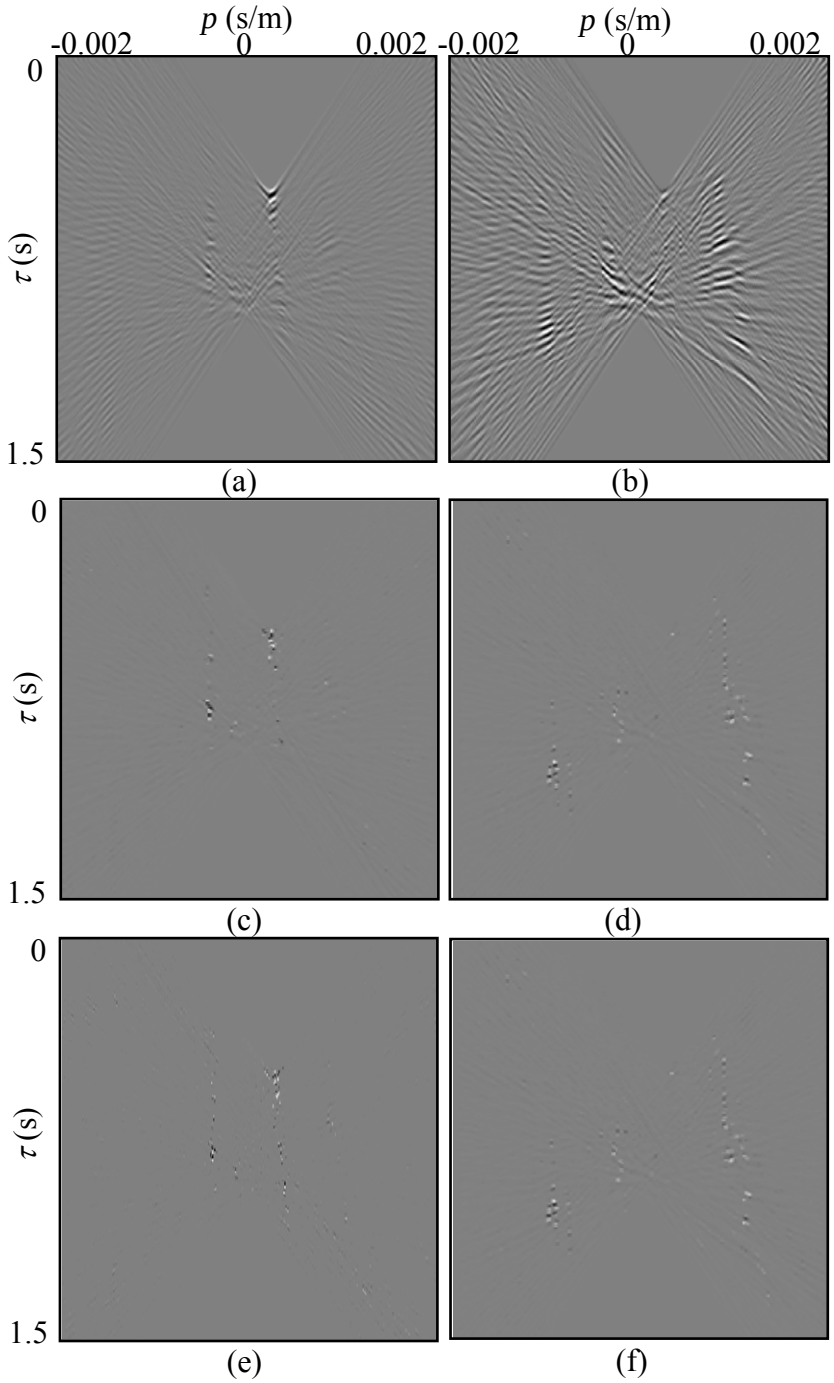

Figure 2.3.7. The last iteration models m_p and m_s depend on the constraints applied: no constraints at all P-wave model (a) and S-wave model (b), sparse constraints P-wave model (c) and S-wave model (d) and constrained P-wave model (e) and S-wave model (f).

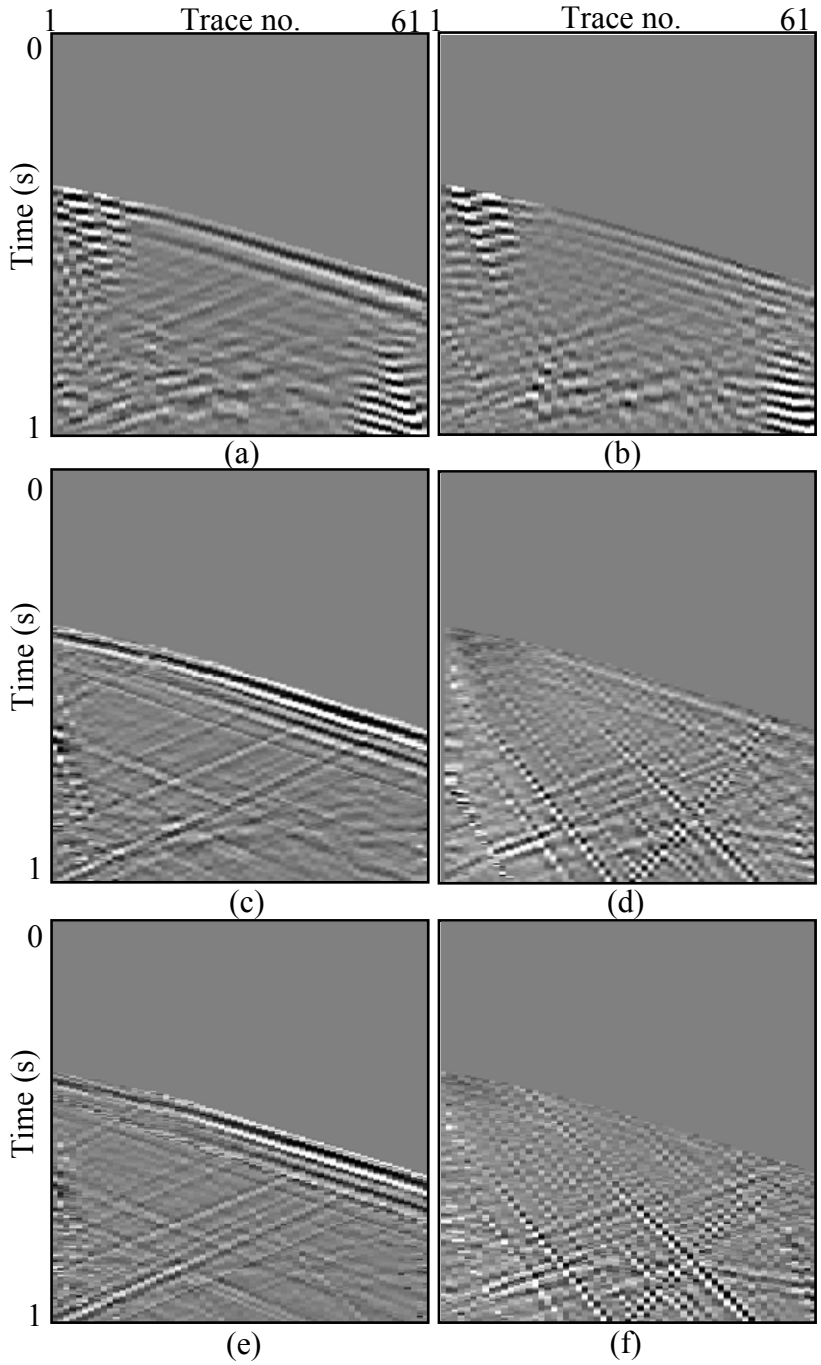

Figure 2.3.8. P wavefield (a) and S wavefield (b) with no constraints applied, sparse constraints P wavefield (c) and S wavefield (d), and constrained P wavefield (e) and S wavefield (f).

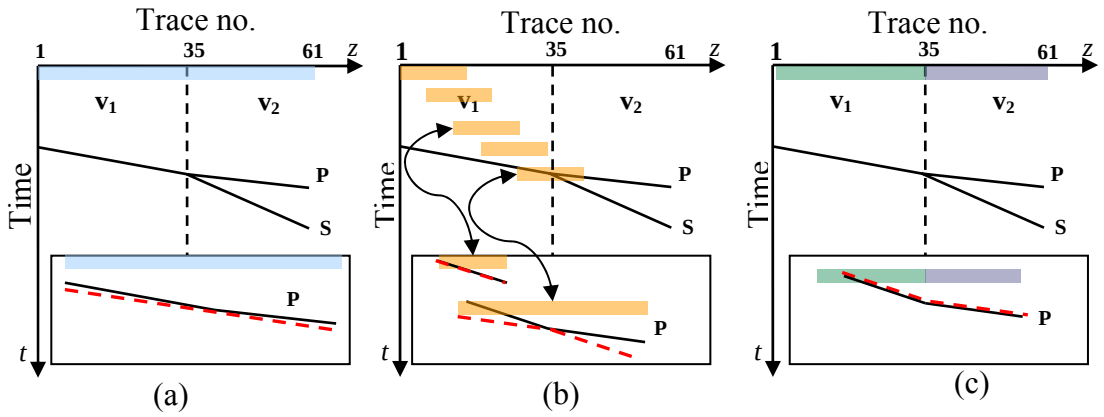

Figure 2.3.9. Three approaches for τ-p filtering: (a) A fixed, large spatial window, (b) a small, running spatial window and (c) a velocity based fixed sequential window (c). Different colours on this scheme show positions and sizes of spatial windows. Reconstruction quality is approximated with dashed red lines.

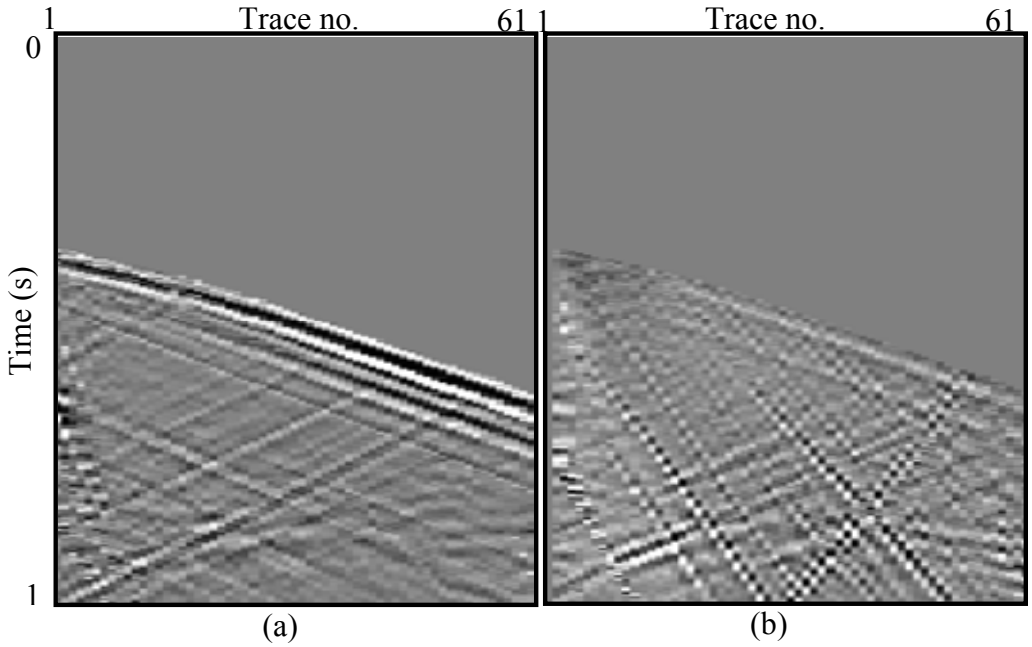

Figure 2.3.10. Separated Vinton Dome shot 3068 P-waves (a) and S-waves (b). High resolution discrete Radon transform algorithm is applied using the fixed, large spatial window approach.

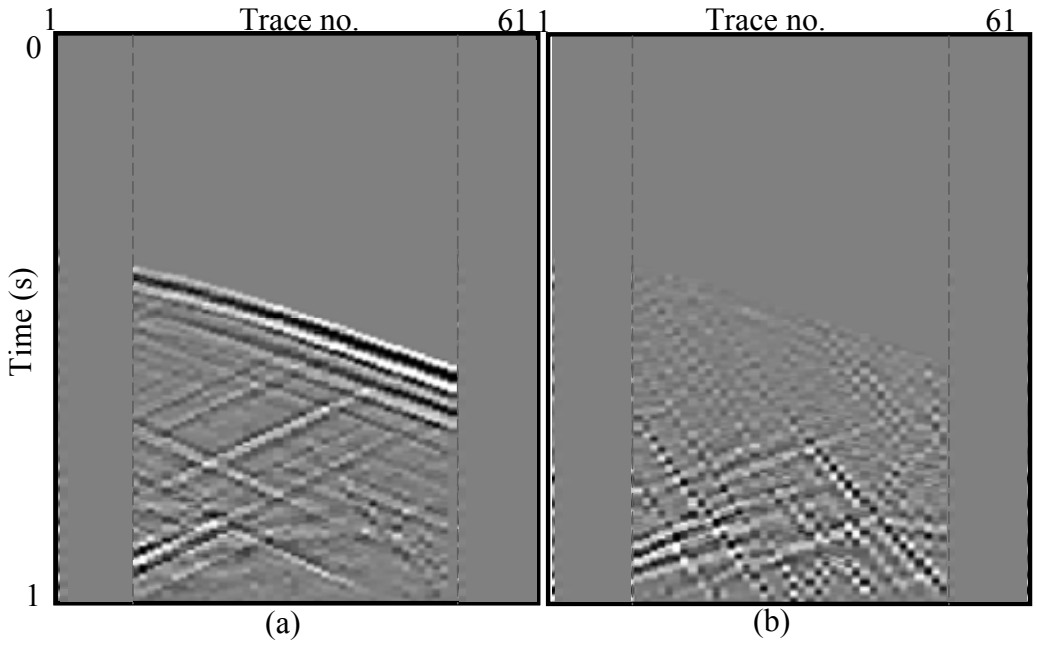

Figure 2.3.11 Separated Vinton Dome shot 3068 P-waves (a) and S-waves (b). High resolution discrete Radon transform algorithm is applied using the small, running spatial window approach. Each window includes 21 traces, such that the first obtained trace is 11th and the last 51st trace.

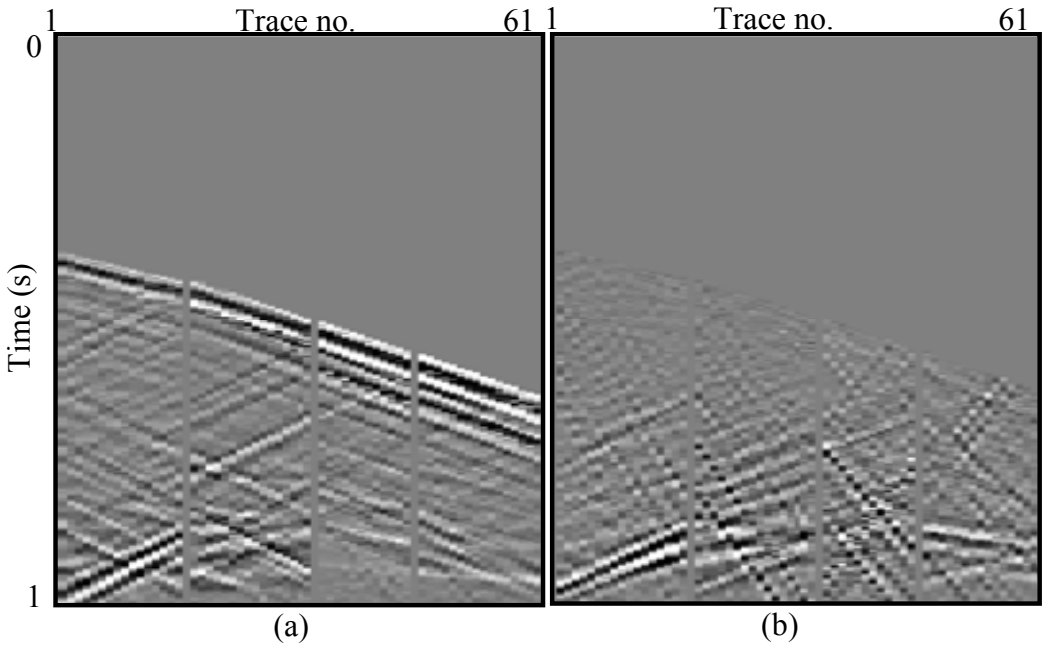

Figure 2.3.12. Separated Vinton Dome shot 3068 P-waves (a) and S-waves (b). High resolution discrete Radon transform algorithm is applied using the fixed, zonal spatial window approach. Window sizes are determined based on the information about the major discontinuities within the well. I have added a gap to show the position of the windows.

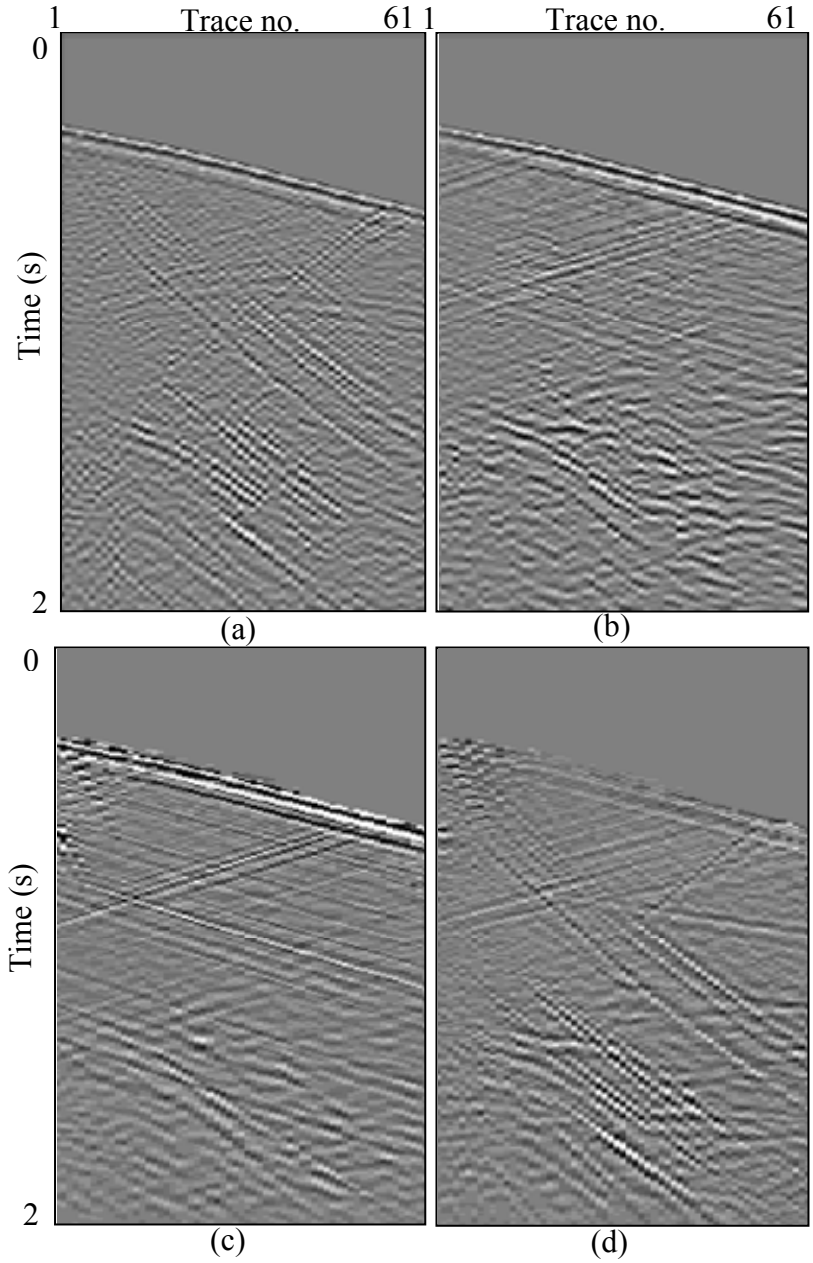

Figure 2.3.13. Shot 3060, near offset 300 m, radial (a) and vertical (b) components. High resolution discrete Radon transform algorithm separates VSP data into P wavefield (c) and S wavefield (d).

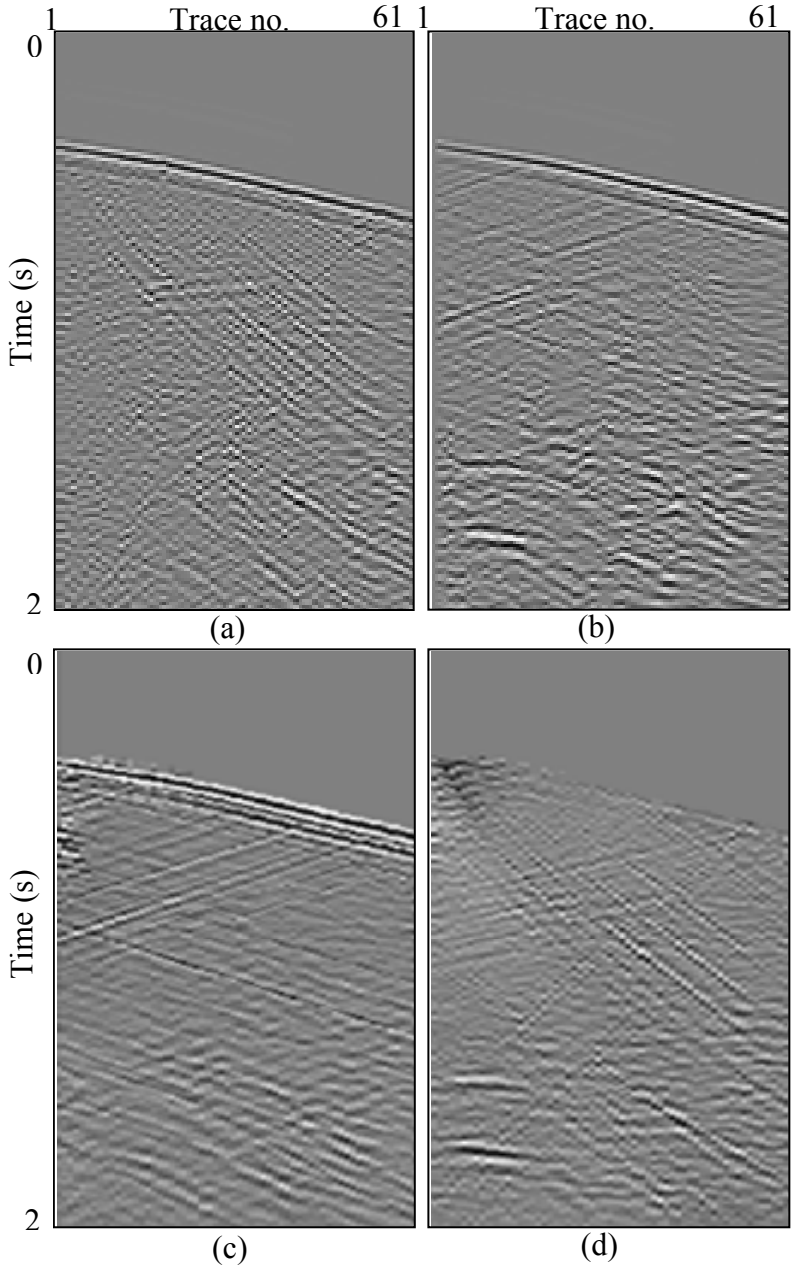

Figure 2.3.14. Shot 3068, mid offset 600 m, radial (a) and vertical (b) components. High resolution discrete Radon transform algorithm separates VSP data into P wavefield (c) and S wavefield.

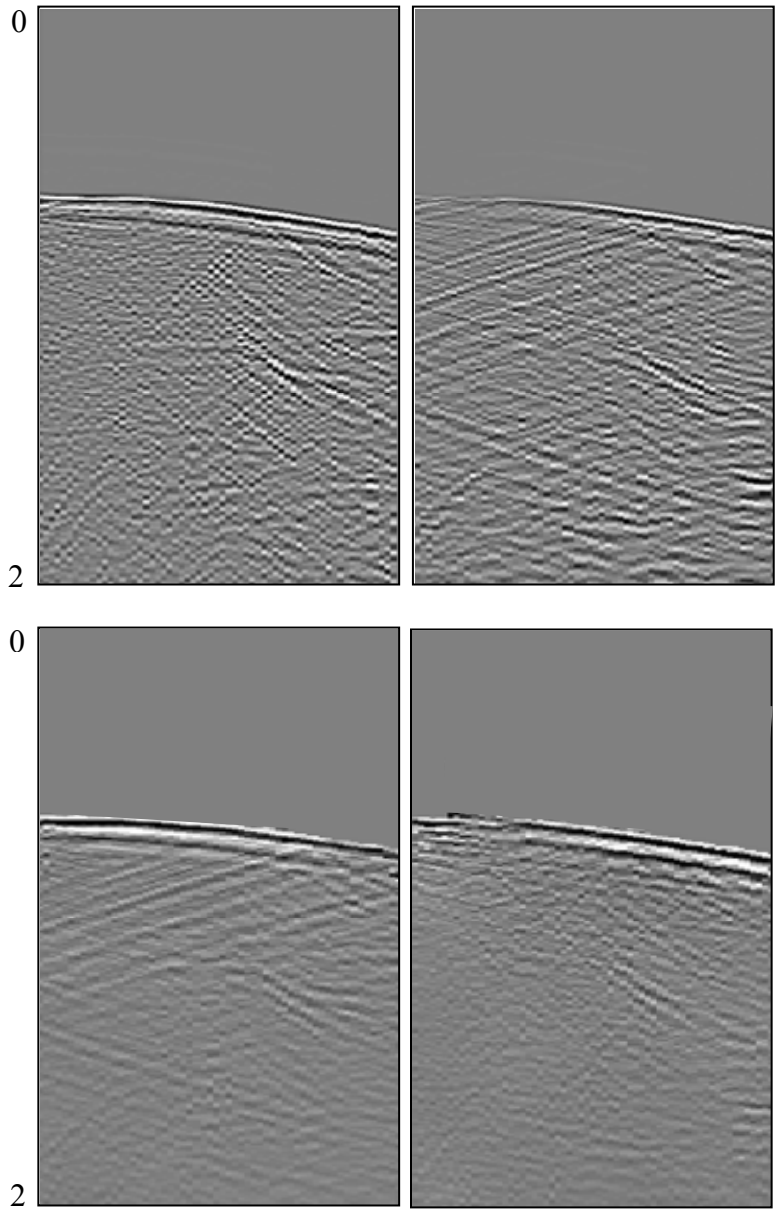

Figure 2.3.15. Shot 3046, far offset 1000 m, radial (a) and vertical (b) components. High resolution discrete Radon transform algorithm separates VSP data into P wavefield (c) and S wavefield.

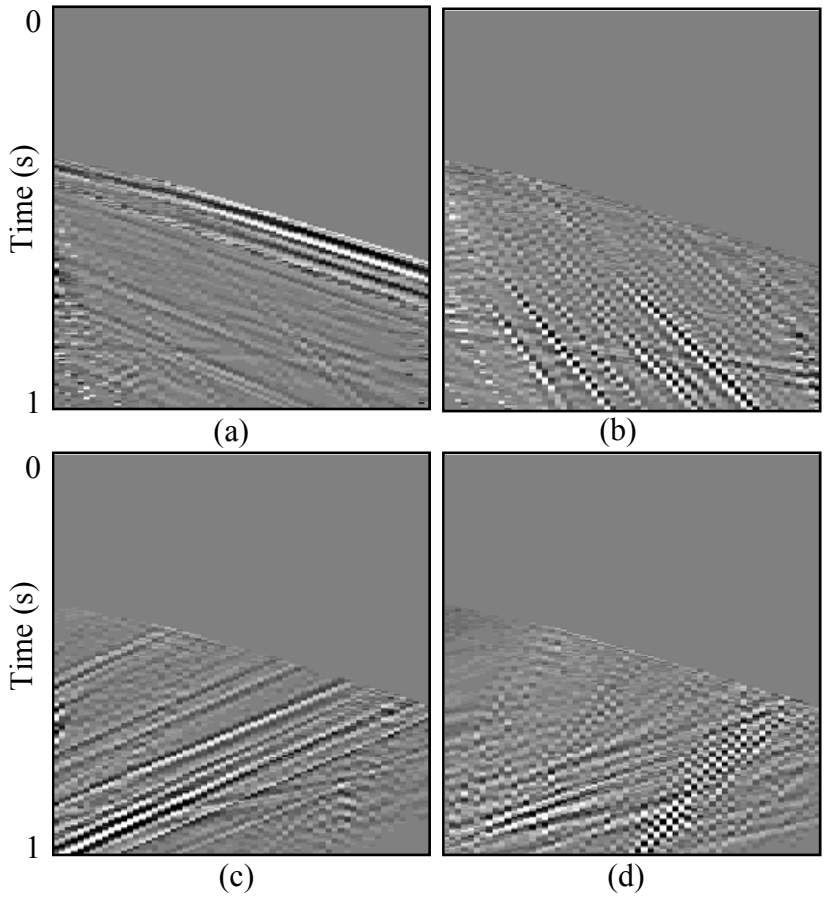

Figure 2.3.16. Negative ray parameters in the P and S model space are muted to separate downgoing P-waves (a) and downgoing S-waves (b). Selection of the opposite mute, filters upgoing P-waves (c) and upgoing S-waves (d).

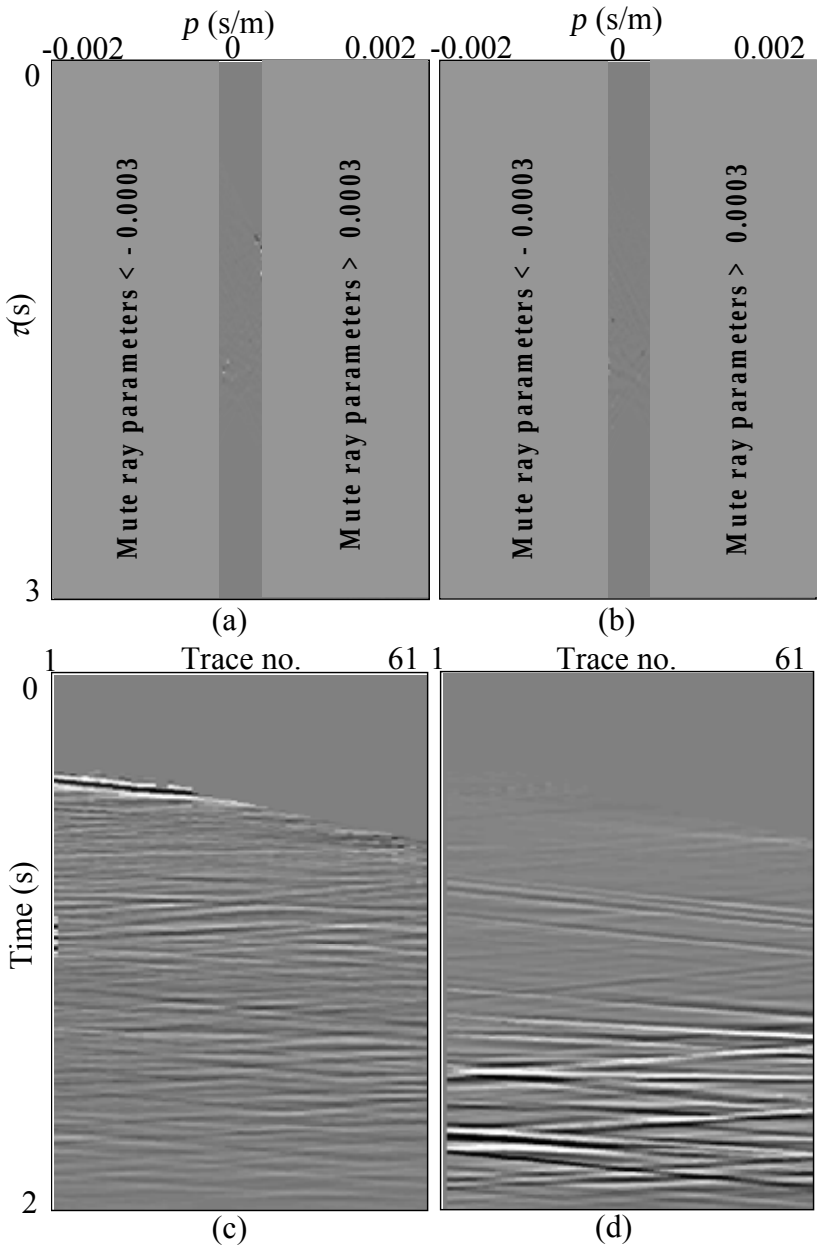

Figure 2.3.17. Mute can be selected for any range of P-waves ray parameter values (a) and S waves ray parameter values (b). Passing the values with the ray parameters close to zero, one can filter out steeper events.

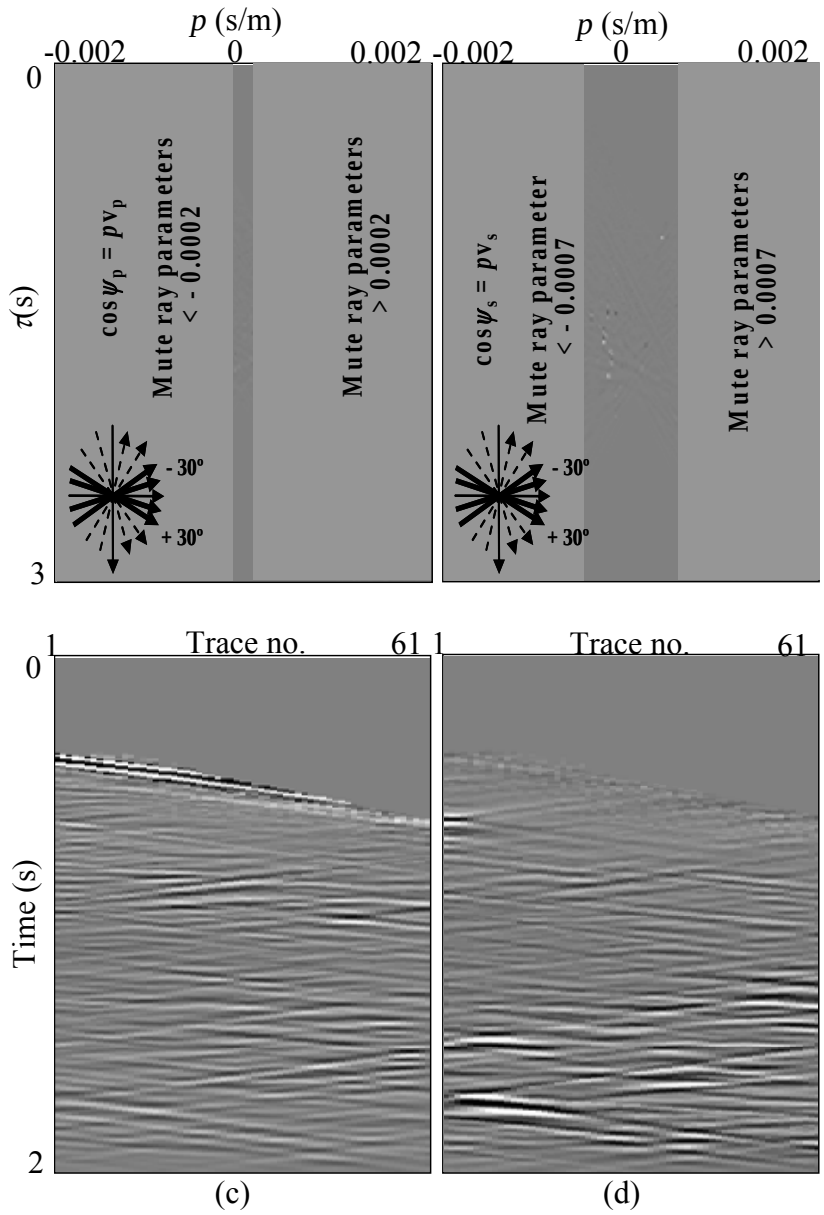

Figure. 2.3.18. Data are filtered based on the incidence angle ψ. For the extraction of the sideways salt reflections, selection of more horizontal events filters the possible salt reflections from the rest of the wavefield (a) and (b). For the extraction of P-wave salt reflections (c), I have selected waves with the incidence angles between +30º and -30º. The same range is selected for the S-wave salt reflections (d).

2.4 Tomographic VSP velocity analysis

Since commercial velocity analysis algorithms are not designed for 3-D VSP geometries, one of our tasks was to develop and apply traveltime tomography to build velocity models for the Vinton Dome VSP data. Building laterally varying velocity models for VSP imaging is challenging due to the narrow ray angle coverage of VSP data. Nearly parallel raypaths from spatially limited positions along the well bore amplify the depth and velocity ambiguity (Bickel, 1990). Simplifications like the flat-layer model (e.g., Moret et al, 2004) and models with planar interfaces (Lines et al., 1984; Lee, 1990) have been implemented to help constrain velocity fields with VSP data. Though a flat-layer velocity model can be robustly constrained with VSP data (e.g., Lizarralde and Swift, 1999), such 1D model is inadequate to resolve the complex geology such as the salt flank and the steep-dipping sediments near the salt dome.

Our solution is a new deformable layer tomography (DLT) which is described in Zhou (2005a) to constrain the geometry of velocity interfaces from an initial model of flat, constant-velocity layers that were parameterized based on *a priori* geologic and geophysical information. The resolution of traveltime tomography depends on ray coverage in terms of hit count (sampling) and crisscrossing level (aperture) of the rays. To ensure that the velocity model be constrainable, DLT directly inverts for the positions (depths) of some pre-defined, laterally continuous velocity interfaces (Zhou, 2005b). A basic assumption of DLT is that a velocity field can be represented by a sequence of constant-velocity layers that may vary in thickness. The DLT acts like an extrapolation tool, starting from a set of estimated layer velocity sequence along the wellbore, DLT

determines the depth variation of the velocity interfaces away from the wellbore for those model blocks that are traversed by the seismic rays.

To illustrate the idea of the DLT, Figure 2.4.1 shows a 2D synthetic test with lateral variations in the interface geometry, using nine near-surface shots and three receivers. The objective of this VSP simulation is to determine the geometry of model interfaces using known layer velocities from well data. Although the first-arrival raypaths that were used are nearly parallel at most locations, DLT can recover the interface geometry within the ray coverage region. As shown above each panel in Figure 2.4.1, the average (av) and standard deviation (sd) of traveltime misfits or residuals decrease with each iteration.

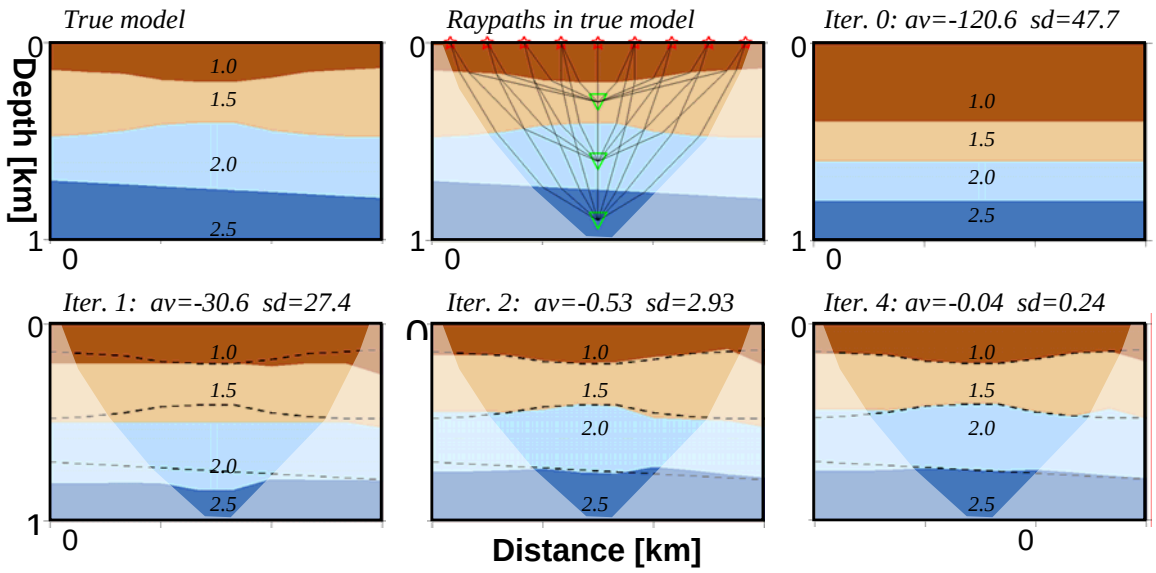

Figure 2.4.1 **The top row show the true model, first-arrival rays from 9 surface shots to 3 VSP receivers, and the initial reference model. The second row shows the solutions of the first, second, and fourth iterations of the DLT. The values on the layers are the velocities in km/s. On each solution panel the dashed curves denote the true interface positions, and the values shown above each panel are the average (av) and standard deviation (sd) of traveltime misfits in milliseconds. On the raypath and solution panels the region outside ray coverage is lightened.**

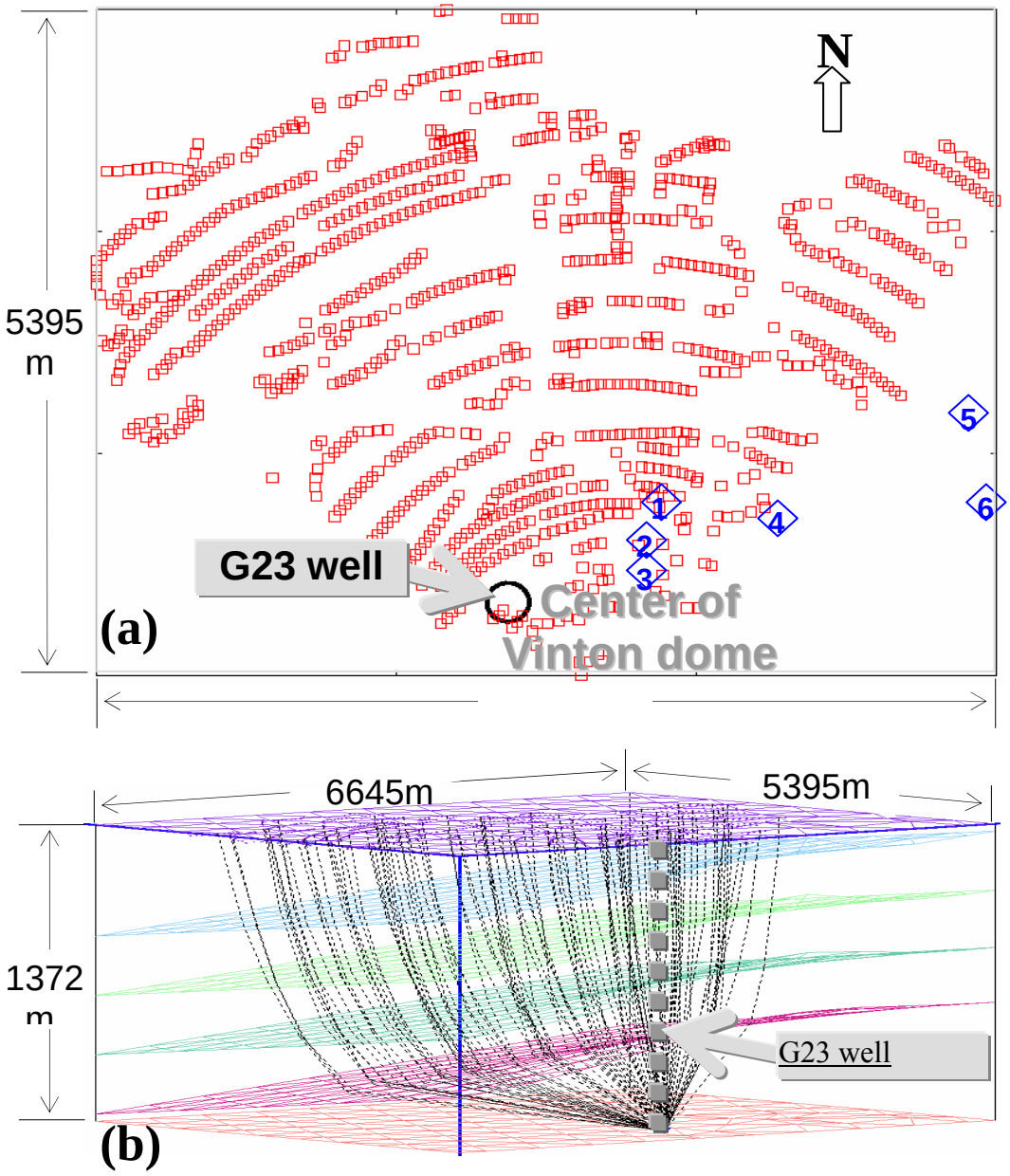

Figure 2.4.2 **(a) Map view of shots (small red boxes) and G23 well (black circle). The blue diamonds with numbers denote locations of six wells with sonic logs that have been compared with the tomographic velocities. (b) 3D view of a five-layer DLT model, a vertical wellbore for downhole receivers (dotted line), and VSP first-arrival raypaths to the deepest receiver (dashed curves).**

Figure 2.4.2a shows the distribution of over 1000 shots for the VSP survey using the G23 well near the northwest flank of the Vinton salt dome. A total of 80 three-component

receivers were cemented inside the wellbore between the depths of 287 m and 1,491 m, with a 15 m depth interval. Nineteen of the receivers were not operable during the survey, and the remaining 61 receivers (Table 2.4.1) recorded high quality data. While the VSP tomography process did not use the velocity information from the sonic logs, six of the sonic logs, whose well locations are indicated by the diamond symbols in Figure 2.4.2a, were used to assess the quality of the tomographic velocity model. Figure 2.4.2b shows raypaths of the first break data from some of the surface shots to the deepest VSP receiver in a five-layer velocity model. The shot-receiver offset of up to 4,951 m is very large in comparison to the maximum receiver depth of 1,354 m.

Table 2.4.1. Receiver order (R#) and depth (Z) of six data subsets.

Subset 1		**Subset 2**		**Subset 3**		**Subset 4**		**Subset 5**		**Subset 6**	
R#	Z[m]	R#	Z[m]	R#	Z[m]	R#	Z[m]	R#	Z[m]	R#	Z[m]
1	287.4	2	302.7	3	317.9	4	333.1	5	439.8	6	455.1
7	370.3	8	485.5	9	500.8	10	516.0	11	531.3	12	546.5
13	561.7	14	577.0	15	592.2	16	607.5	17	622.7	18	637.9
19	653.2	20	668.4	21	744.6	22	759.9	23	775.1	24	790.3
25	805.6	26	820.8	27	836.1	28	851.3	29	866.5	30	881.8
31	897.0	32	912.3	33	927.5	34	942.7	35	958.0	36	973.2
37	988.5	38	1003.7	39	1018.9	40	1034.2	41	1049.4	42	1064.7
43	1079.9	44	1095.1	45	1110.4	46	1125.6	47	1140.9	48	1156.1
49	1171.3	50	1186.6	51	1201.8	52	1217.1	53	1232.3	54	1247.5
55	1262.8	56	1278.0	57	1293.3	58	1308.5	59	1323.7	60	1339.0
61	1354.2										

Methodology and Processing Sequence

The DLT method is based on the traditional layer tomography that has been developed for reflection imaging (e.g., Bishop et al., 1985; Kosloff et al., 1996). Layer tomography is especially suitable for areas where the expected range of velocity values can be estimated from well logs, check-shot surveys, and geologic data. The velocity range can also be inferred from inspection of the traveltime versus distance plots or from previous geophysical surveys. If an approximate velocity structure can be inferred, then the spatial distribution (depths) of the velocity values becomes the principal unknown, and the DLT inversion process will converge to a data-best-fit velocity structure by iteratively adjusting velocity layer depths.

To cope with uneven ray coverage and under-determinacy in parts of the model, the DLT method takes a multi-scale inversion scheme (Zhou, 2003). Multi-scale tomography simultaneously determines overlapping solution components of different wavelengths (different sizes of triangles) with the aim of producing a better matching between the pattern of the targeted heterogeneities at each position with some of the model elements at the location. Divisions of each model interface with triangular elements of different sizes constitute the sub-models of the multi-scale inversion. The hierarchical size structure of the triangular model parameterization is naturally suitable for the multi-scale inversion.

For the Vinton Dome study, the multi-scale DLT algorithm has been adapted to include a progressive inversion sequence from long-wavelengths to short-wavelengths, which is an

important change from an earlier version (Zhou, 2004). The advantage of progressive tomographic modeling has been well documented (e.g., Nemeth et al., 1993; Bube and Langan, 1994, 1999; Washbourne et al., 2002). Figure 2.4.3 shows the processing sequence for multi-scale DLT applied to the VSP dataset. The DLT algorithm includes a progressive inversion sequence of two nested loops. Each outer progressive loop defines the number of multi-scale sub-models to be used by all inner loops. The first sub-model simply calculates the average depth of each interface and/or layer slowness. A new sub-model is added to each subsequent outer-loop until all multi-scale sub-models have been inverted.

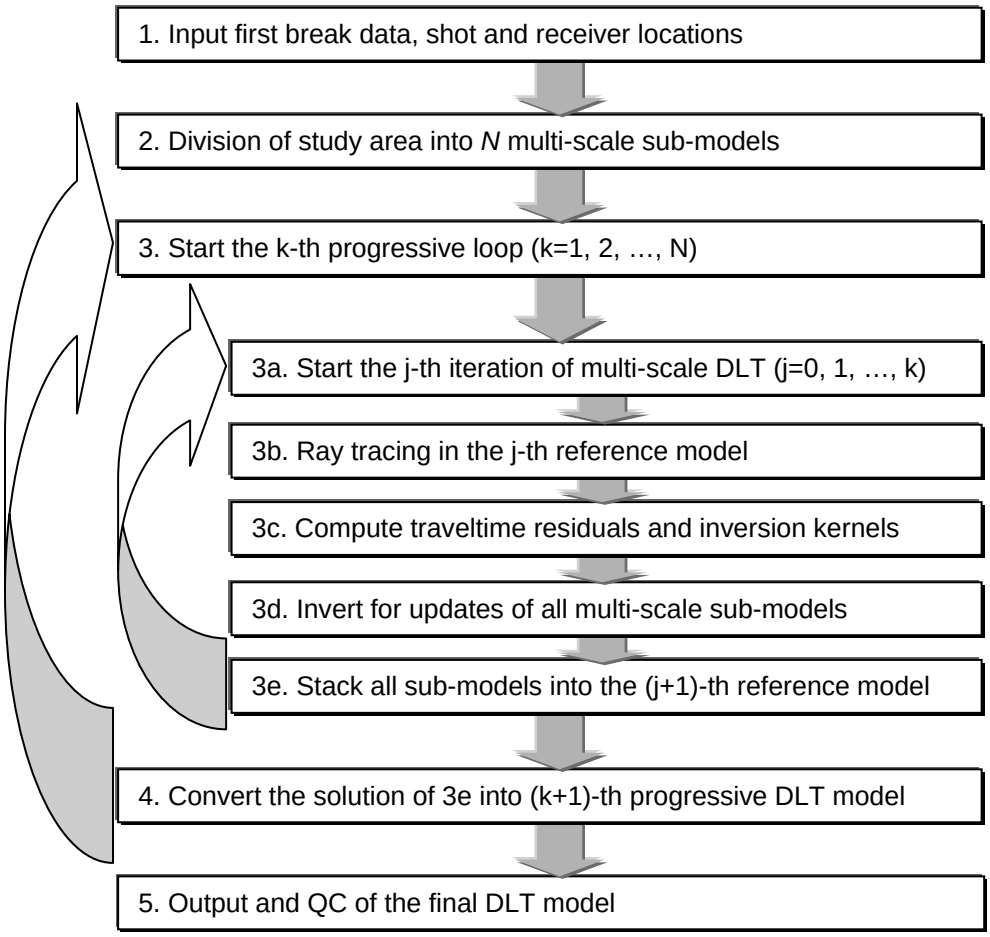

Figure 2.4.3 Flowchart of the progressive multi-scale DLT.

The inner loop is a typical tomographic iteration sequence that simultaneously inverts for updates of all sub-models defined by the outer loop. Each of the inner-loop iterations consists of ray tracing in all sub-models to compute the Frechet kernels and traveltime residuals, inverting for model updates, and assessing data fitting statistics and model variations. The calculations of the data fit and the solution variations through the inversion iterations provide criteria to terminate the iteration sequence and to select the best model.

Figure 2.4.4 illustrates the DLT method for a 3D synthetic model of a 12×15 km^2 area where a 4572-meter-long vertical well is drilled in the middle. There are 14×17=238 shot locations at the surface, and five receivers placed along the well with a depth interval of 914 m. The synthetic true model has four layers, whose velocities are 1.5, 2.0, 2.5, and 3.0 km/s, respectively, from top downwards. The DLT was able to recover the lateral variation of velocity interfaces using only the first arrivals from five VSP receivers.

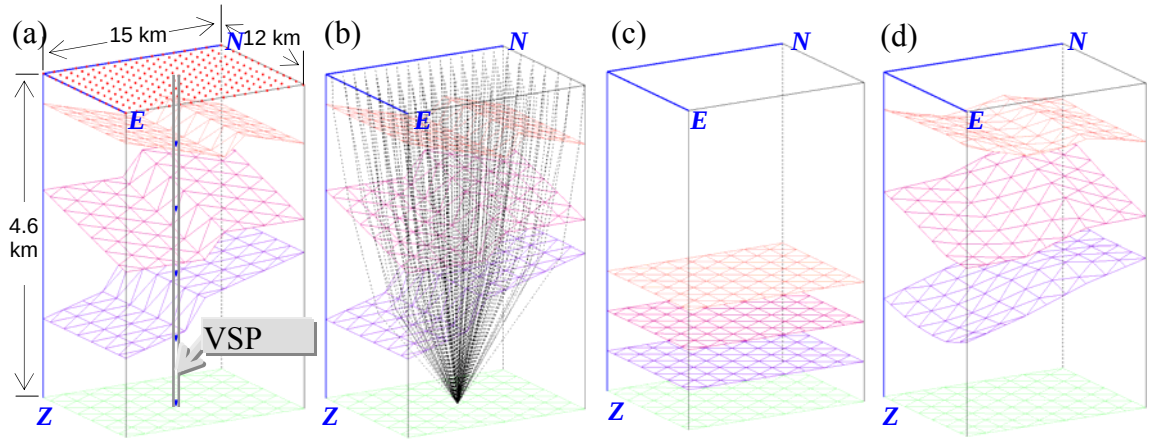

Figure 2.4.4 3D views of a synthetic VSP test. (a) The true model in which three interfaces are faulted. (b) The first-arrival raypaths to the deepest receiver. (c) The initial reference model with flat interfaces. (d) The final DLT solution. There is a 5:1 vertical exaggeration.

Vinton Dome VSP tomographic model and uncertainty estimation

The Vinton Dome model consists of a total of ten multi-scale sub-models with nine triangular divisions of each interface, and the model parameterization was the same for all model interfaces. The first division, which includes the whole area, is the first sub-model for the average depth of each interface as well as the second sub-model for the dip of each interface. The next eight triangular divisions consist of triangles with side lengths of 1/1, 1/2, 1/3, 1/4, 1/5, 1/6, 1/8 and 1/10 of the east-west length of the model area, respectively (cf. Zhou, 2005b). Thus, ten multi-scale sub-models were used for each

model interface. Ten progressive loops, each consists of ten inner-loop iterations of multi-scale tomography (ray tracing, inversion, and model updating), were computed. The first progressive loop used only the first sub-model, the second progressive loop used the first two sub-models, and each subsequent loop added another sub-model. All of the ten sub-models were used in the last progressive loop.

To develop a statistical basis for analyzing uncertainty of the DLT velocity model, the 61 VSP common-receiver gathers from the Vinton Dome G23 well were divided into six data subsets (Table 2.4.1). When the number of data is sufficiently redundant, the solutions from processing different data subsets allow an assessment of solution statistics (e.g., Tichelaar and Ruff, 1989). A DLT velocity model was generated for each data subset, and the results were statistically compared. Each velocity model consists of a small number of layers and the dataset is relatively redundant in this case. Figure 2.4.5 shows a series of the DLT results for the five-layer model using the first data subset with 11 gathers. The given layer velocities are 1.7, 1.9, 2.1, 2.3, and 2.5 km/s, from top downward. The initial reference model (upper left panel in Figure 2.4.5a) has horizontal interfaces distributed evenly in the lower portion of the model space.

As shown in Figure 2.4.5, the first progressive DLT loop is able to recover the average depths of the interfaces. This indicates that further solutions will not depend much on the interface depths of the initial reference model. Additional DLT loops gradually resolve the fold-shaped velocity interfaces which resemble a swell up of sediments near the salt dome. Since the top interface of this solution does not differ much from the ground surface, the subsequent DLT model studies of the Vinton Dome data were carried out

using a four-layer model with layer velocities of 1.8, 2.1, 2.3, and 2.5 km/s. We have derived six four-layer solution models for the six subsets of the Vinton Dome VSP first break data. These solution models are generally similar to each other except near the edges of the model where the ray coverage is poor.

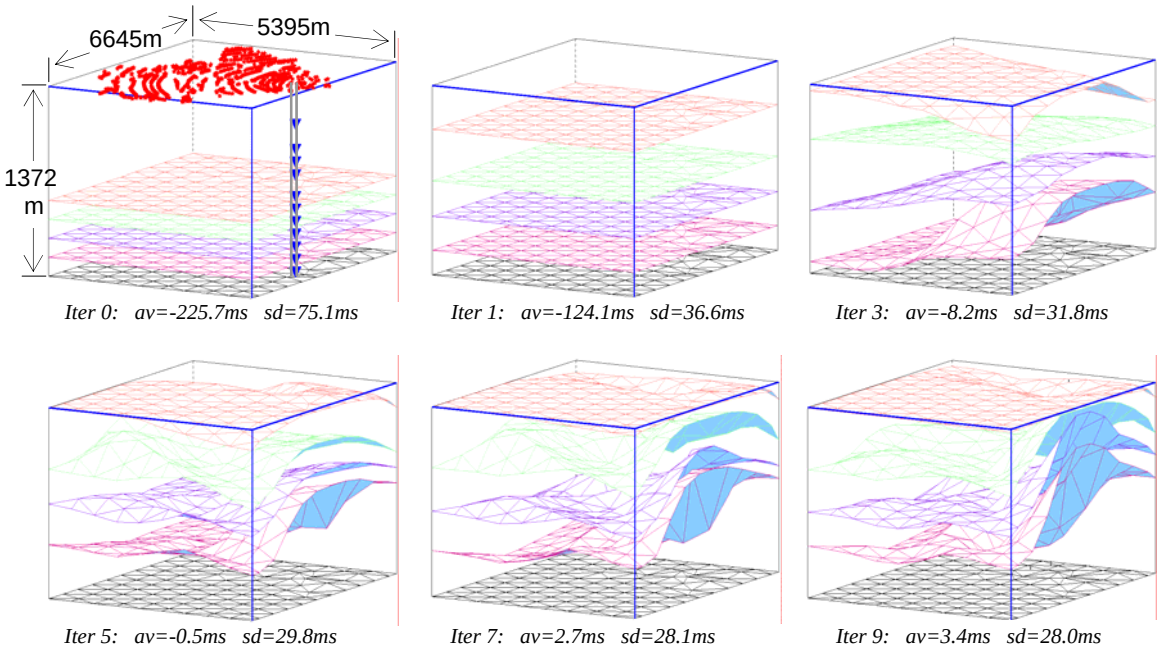

Figure 2.4.5 3D view of the initial reference model and solutions of the first, third, fifth, seventh, and ninth DLT loops for a five-layer model based on the first data subset. In the upper left plot of the initial reference model, the red stars are shots, and blue triangles are VSP receivers. The layer velocities are 1.7, 1.9, 2.1, 2.3, and 2.5 km/s, from top downward. Note the gradual formation of interfaces dipping away from the salt dome (see Figure 1 for location). The values shown blow each solution are the average (av) and standard deviation (sd) of traveltime misfits in milliseconds.

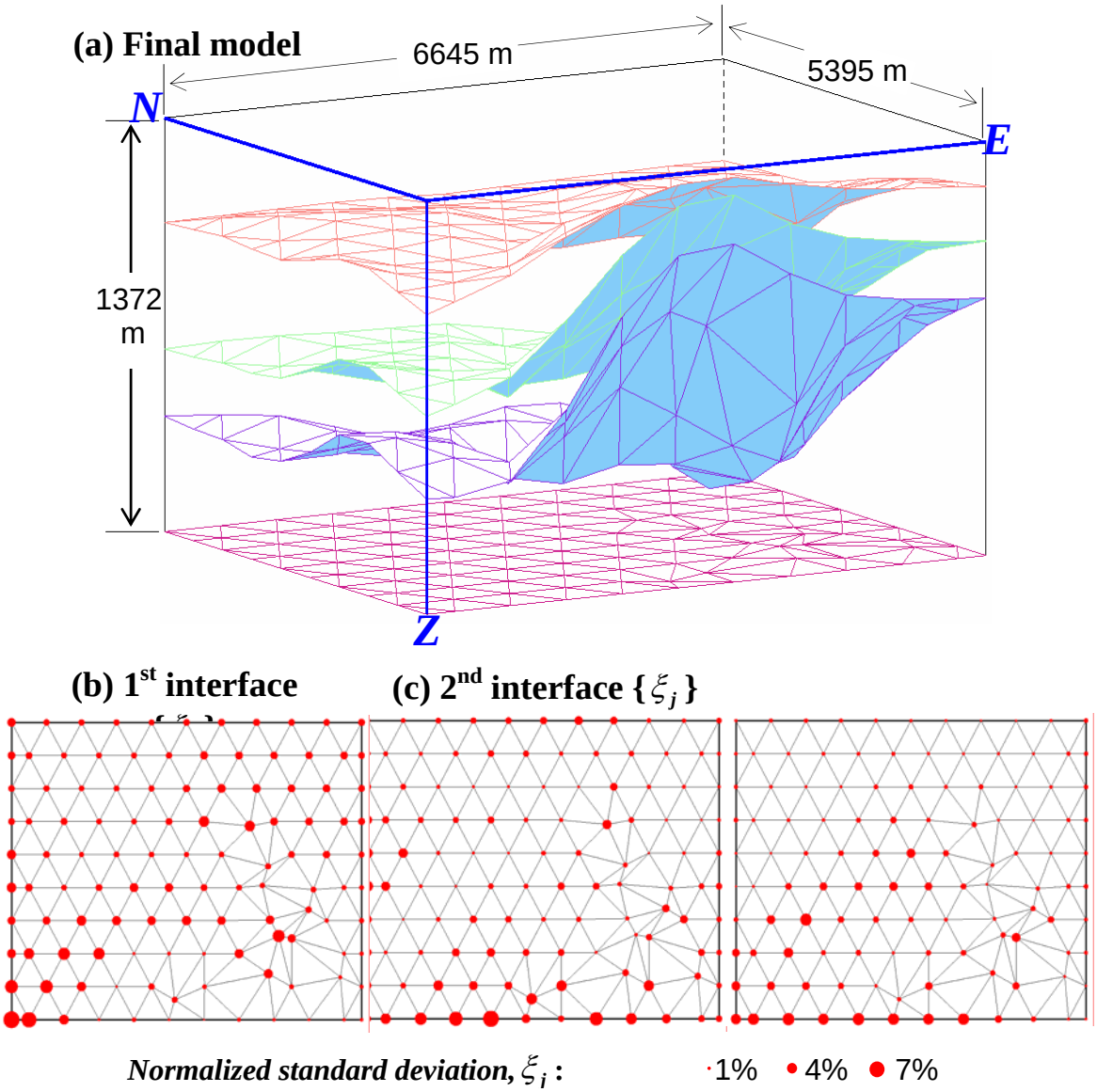

Figure 2.4.6 **(a) 3D view of the final model, which is the average of six solutions from the six data subsets. The layer velocities are 1.8, 2.1, 2.3, and 2.5 km/s, from top downward. For this model, the average and standard deviation of traveltime misfits for all 61,225 first arrivals are 1.16 ms and 27.76 ms, respectively. (b) to (d) are map views of normalized standard deviations $\{\xi_j\}$ of the three internal interfaces.**

The final solution (Figure 2.4.6a) is the average of the six subset solutions. If the differences of the subset solutions are due to random effects, the average or 'stacked' solution should exhibit an enhanced S/N ratio and represent a best estimate solution. Figures 2.4.6b to 2.4.6d show the normalized standard deviation of interface depths for

the six solutions for each internal interface. The normalized standard deviation at the j-th node of the internal interfaces is defined as

$$\xi_j = \frac{100}{Z_{\text{model}}} \times \left[\frac{1}{6} \sum_{i=1}^{6} \left(z_{ij} - \bar{z}_j \right)^2 \right]^{1/2}$$

where Z_{model} is the depth range of the model, z_{ij} is the depth of the j-th node in the i-th subset solution, and $\bar{z}_j$ is the average depth of the j-th node among the six solutions. Each value of $\{\xi_j\}$, as shown in Figure 2.4.6b to 2.4.6d, is the standard deviation of the six solutions normalized as percentage of the model depth range. The robustness of the final solution as shown in Figure 2.4.6a at the j-th node is inversely proportional to the value of ξ_j. A smaller value of the normalized standard deviation means a higher level of robustness. Most of the interface nodes, as shown in Figure 2.4.6b to 2.4.6d, have less than 3% of the normalized standard deviation among the six solutions. Large deviations usually occur near the boundaries or in other poorly covered portions of the model.

Comparison of VSP tomography with sonic logs

Figure 2.4.7 compares six sonic logs with the values of the final DLT solution (Figure 2.4.6a) at the well locations (see locations of wells in Figure 2.4.2a). In addition, velocity values are available from a 3D velocity-depth model for the Vinton Dome region that is based on over 20 well logs and 7 horizons picked from a time-migrated volume of a 3D surface seismic reflection dataset. This previous 3D velocity model is referred to here as the horizon-sonic model to distinguish it from the DLT derived VSP tomographic model. Each panel in Figure 2.4.7 displays the layer velocities of the VSP tomographic model (blue curve), the sonic velocity (dashed red curve), and the horizon-sonic model (green

curve). Obviously the tomographic velocity curves from a four-layer model represent only the long-wavelength component of the velocity field. The horizon-sonic model values closely match the sonic log values because the horizon-sonic model was derived from sonic log velocity values and a sequence of horizons picked from a prestack time migrated volume of the surface seismic data. The horizon-sonic model has a strong regional component, while the sonic curves are local vertical measurements of the P-wave velocity.

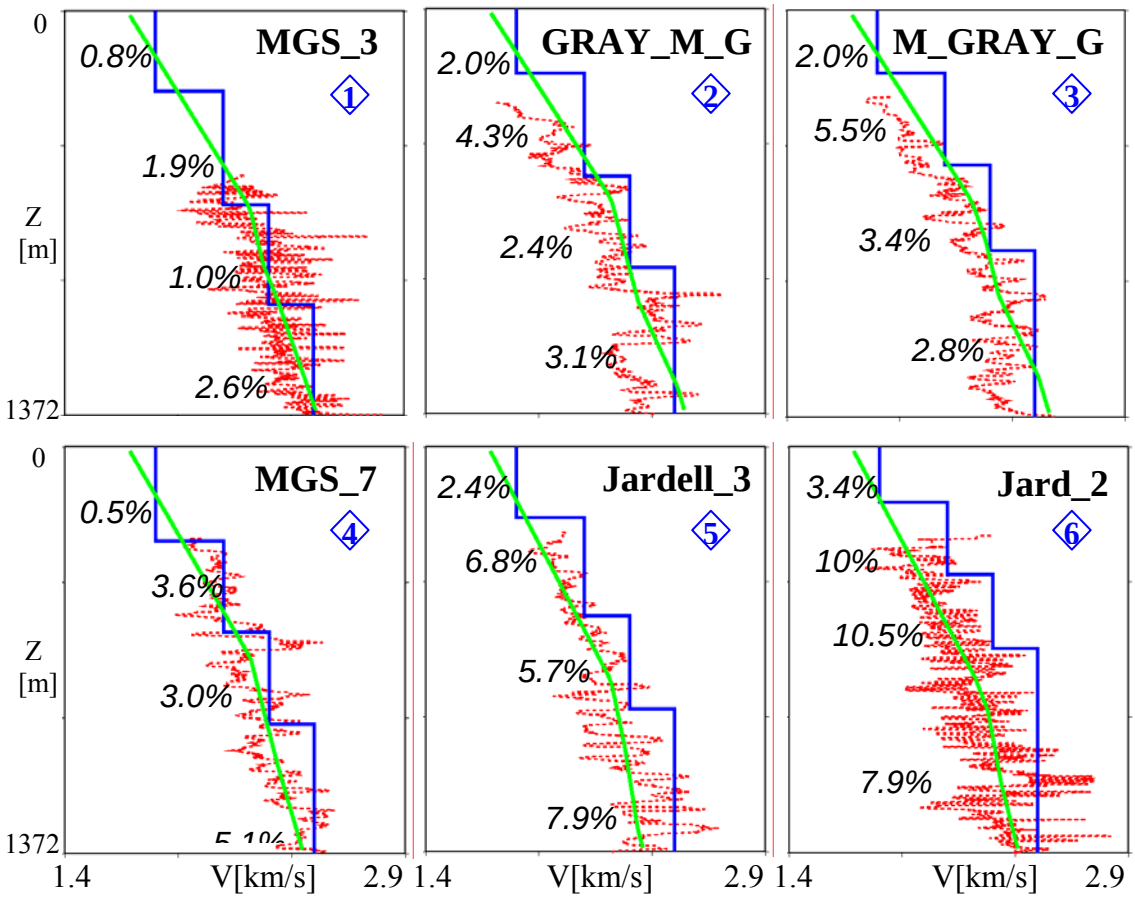

Figure 2.4.7 Comparison between the vertical velocities of the final DLT model (blue curves), sonic logs (dashed curves in red), and the 3D horizon-sonic model (green curves). On each panel the percentage values are the differences between the tomographic VSP velocity and the layer average velocity of the horizon-sonic model. The number inside the diamond symbol indicates each well location shown in Figure 2.4.2.

Though DLT model velocity values match the trends of the sonic logs well, in all six cases shown in Figure 2.4.7, the tomographic velocities are systematically faster than the sonic velocities. The differences between the tomographic VSP velocities and the layer average velocities of the horizon-sonic model are indicated on the figure by the percent values. The first four wells in Figure 2.4.7 are located close to shot locations and are, therefore, in areas of good VSP ray coverage. The interval velocities from these four wells fit the tomographic velocities better than the last two wells, but the tomographic velocity trend is clearly higher than the sonic log trends for all six wells. On the average, the tomographic VSP velocities are 2.75% faster for the first four wells than the horizon-sonic model, which resembles a smoothed trend of the sonic measurements.

One explanation for the slower trend of the vertical VSP velocities than the sonic velocities is related to the effects of bedding anisotropy on seismic velocities. Stewart et al. (1984) showed by modeling that the higher sonic velocities are consistent with the existence of velocity dispersion. De et al. (1994) confirmed that the vertical VSP velocities tend to be slower than the sonic velocities for both P-waves and S-waves, and that the S-wave deviation equaled about one half of the P-wave deviation. The reversed trend of higher tomographic VSP velocities than the sonic velocities at Vinton Dome, as shown in Figure 2.4.7, is likely explained by the presence of velocity anisotropy. Since the offset range of up to nearly 5 km is much greater than the depth range of less than 1.35 km for the Vinton Dome VSP data, many far-offset first arrivals probably had traversed close to the high-velocity bedding directions. Similar trends of faster offset-VSP velocities than sonic velocities were observed by Kebaili and Schmitt (1996). The

current study cannot differentiate between vertical transverse isotropy and bedding-oriented, tilted transverse isotropy, though the latter is more likely. Since the vertical VSP velocity must be slower than the sonic velocity, the lateral VSP velocity must be much faster than the sonic velocity in order for the VSP velocity to be 2.75% faster than the sonic velocity. We plan to investigate more on the level of anisotropy, following previous works by (Chiu and Stewart, 1987; Mao and Stuart, 1997; Grech, et al., 2002; and Zhou et al., 2003).

2.5 Depth migration of VSP data

Hoelting et al. (2002, 2003a) evaluated phase screen migration of VSP geometries. Discussions with Paul Constance of OPEX lead us to believe that turning conventional migration 'sideways' might help us better image the salt flank. Good images were obtained using 2-D synthetics from ray theoretical and finite difference models, and were presented at the October 2002 SEG meeting resulting in the best student poster award for Hoelting and his colleagues.

All “production” migration of the 3-D VSP field data was performed with an in-house 3-D Kirchhoff depth migration. We have implemented to variants of this migration: (1) a scalar migration (like most industry migration algorithms) and (2) an elastic migration which performs polarization filtering during imaging. The elastic version of our Kirchhoff depth migration was the subject of Mariana Gherasim’s thesis (Gherasim, 2005). This section presents relevant results from Gherasim (2005), including VSP images of the field data.

2-D VSP synthetic scalar Kirchhoff pre-stack depth migration

After deciding to calculating the traveltimes using the Fast Marching method eikonal solver from the Stanford Exploration Project (SEP), we focused our attention on developing the scalar pre-stack depth migration algorithm. Gherasim (2005) started with an in-house 3-D Kirchhoff pre-stack time migration code running under MPI. She read in common-shot gathers, the source and receiver traveltime tables, and performed the imaging. She migrated the seismic traces that fell within specified offset and azimuth

limits. A second version of the pre-stack depth migration algorithm sorts the output into receiver depth bins.

Stolt and Benson (1986) presented the following simplified formula for the 3-D prestack Kirchhoff migration:

$$M(x) = \sum_{x_s, x_r} W(x_s, x_r, x) D_{sr}\left(t_s(x_s, x) + t_r(x, x_r)\right) \qquad (2.5.1)$$

where M(x) is the migrated image at 3-D location x,

$W(x_s, x_r, x)$ represents the weighting factor or the amplitude compensation function which relates to the survey geometry, velocities along the raypath, and the geophone aperture,

x_s and x_r are the source and receiver locations in 3-D,

D_{sr} $(t_s(x_s, x) + t_r(x, x_r))$ is the recorded wavefield, and

$t_s(x_s, x)$ and $t_r(x, x_r)$ are traveltimes from the source to image position and from the image position to the receiver.

The migration process spreads the recorded reflected energy at time t onto an ellipsoid. The resulting image at each location x consists of a superposition of weighted energies WD_{sr} of all the ellipsoidal surfaces at x for each source x_s and each receiver x_r (Wang, 2004).

Bleistein (1987) derived a weight equation for pre-stack common-offset migration:

$$W = z\sqrt{1+\frac{(x_s - x)\bullet(x_r - x)}{|x_s - x||x_r - x|}}\sqrt{\frac{|x_s - x|+|x_r - x|}{|x_s - x||x_r - x|}}\left[\frac{|x_r - x|}{|x_s - x|}+\frac{|x_s - x|}{|x_r - x|}\right] \quad (2.5.2)$$

where W – weighting factor,

x_s – source X coordinate,

x_r – receiver X coordinate,

x – imaging point X coordinate, and

z – depth to the image point.

Gray (1998) rearranged Bleistein's equation into a new formula that solely depends on the sum between the source and receiver traveltimes.

$$W = \frac{8}{(t_s + t_r)^2} \quad (2.5.3)$$

where W - weighting factor,

t_s – source traveltime, and

t_r – receiver traveltime.

The major advantage of Gray (1998) formula is the minimum number of operations that needs to be performed in order to calculate the weighting factor, operations that can significantly increase the computation time when included inside the inner migration loop. In obtaining the new formula, Gray assumed constant velocity and ignored constant factors involving powers of 2, π and v.

Since most of the weight or amplitude factor equations are derived for the surface type of acquisition geometry, we preferred to use Gray (1998) formula.

Another important factor in migration techniques is the antialiasing filter (Gray, 1992; Lumley *et al.*, 1994; Abma *et al.*, 1999; Biondi, 2001).

Lumley *et al.*(1994) defined three types of aliasing:

1- Image aliasing occurs when the output sampling of the image space is too coarse to properly represent the migration dips,
2- Operator aliasing occurs when the operator dip along the migration summation trajectory is too steep for a given input seismic trace spacing and frequency content, and
3- Data aliasing occurs when the trace spacing is too coarse (Bardan, 1987).

Since "Image aliasing" can be easily avoided by using a proper output sampling, we will only focus on "Operator aliasing" and "Data aliasing".

Operator aliasing

As stated before, Kirchhoff migration method performs a sum over an aperture of input traces to obtain output at a single point. The length of the aperture is limited by a spatial Nyquist criterion, which typically prohibits imaging very steep dips at very high frequencies without generating severe migration artifacts (migration operator aliasing) (Gray, 1992). We followed Gray's idea of creating three copies of the data. Given an aperture suitable for migrating out to a specified maximum dip the frequencies in the data, which migrate out to the farthest offsets of the migration aperture, are restricted and all frequencies that migrate out to the shorter offsets are left intact.

Gray's antialiasing method is designed for migration in the time domain so we had to adjust it for the depth domain. In the pre-stack time migration algorithm, Nyquist frequency was defined as

$$f_N \le \frac{1}{2 \cdot \Delta t} \qquad (2.5.4)$$

The modified Nyquist formula that we used in the pre-stack depth migration is

$$f_N \le \frac{Vsmooth}{2 \cdot \Delta z} \qquad (2.5.5)$$

Data aliasing

Kirchhoff migration spreads the energy of each time sample of a trace along a traveltime isochrone for each pair source-receiver corresponding to that trace. The final image represents a weighted sum of all the individual images. During the summation, events constructively and destructively interfere to form the image. We assume that the interference should act more successfully when having smaller source spacing.

Gardner *et al.* (1974) stated a similar idea by approximating a horizontal planar reflecting sheet with a set of horizontal cylindrical threads. Their experiment consisted of recording seismic data using constant offset source-receiver pairs along a surface line perpendicular to the axes of the set of parallel threads whose spacing decreases form one side to another. They proved that the resulting image looks smooth and continuous in the part corresponding to the closely spaced threads and is contaminated with migration tails in the part corresponding to the sparse threads.

Calibration

Since the migration program is designed to migrate 3-D data, we constructed a 2.5-D model by concatenating the 2-D velocity model five times. The resulting model is 18000 ft long in x direction, 240 ft long in y direction and 8000 ft deep. We migrated only one line out of this volume, corresponding to the 2-D velocity model used to generate 2-D VSP synthetics and traveltimes.

We present a 3-D view of the 2.5-D P-wave velocity model in Figure 2.5.1. We first tested the program using shot no. 2, vertical and horizontal components, which contains PP reflections only. We display the result of the PP scalar Kirchhoff pre-stack depth migration in Figure 5.2.2.

In our data aliasing test, we started by migrating the group of 14 synthetic shot-gathers, vertical and horizontal components, PP reflections only. We display the PP depth images for both, vertical and horizontal components, in Figure 2.5.3. We mark with an arrow the location of the common-image gather displayed in Figure 2.5.4. As we can see, the aliasing effect is quite strong in both depth images. Since the shots are located too coarse and the subsurface illumination is concentrated around the well location, the constructive interference did not take place successfully.

We can remove the aliasing effect by combining two methods:

a) semblance weighting during stacking;

b) reducing shot spacing.

Semblance weighting

The similarity between two traces can be determined by the cross-correlation function. If we stack several channels together, the resulting amplitude is generally large when the individual channels are similar or coherent so that they stack in phase, and small where they are dissimilar or incoherent. The average amplitude of J stacked traces is given by

$$m_j\left(k\Delta z\right) \equiv m_{avg}\left(k\Delta z\right) = \frac{1}{J}\sum_{j=1}^{J} m_j\left(k\Delta z\right) \qquad (2.5.6)$$

where m_j is the amplitude of an j^{th} migrated trace at depth $k\Delta z$,

m_{avg} is the average amplitude at depth $k\Delta z$,

J is number of samples.

The energy of the stacked trace within a vertical window (-w, +w) is given by

$$E = \sum_{\zeta=z-w}^{z+w} m_{avg}\left(\zeta\right). \qquad (2.5.7)$$

where E is the energy of the stacked trace within a window,

ζ is the length of the window.

The semblance within that window, $\sigma(z)$, is given by

$$\sigma\left(z\right) = \frac{\sum_{k=-K}^{+K}\left(\sum_{j=1}^{J} m_j\left(k\Delta z\right)\right)^2}{\left(2K+1\right)\sum_{k=-K}^{+K}\sum_{j=1}^{J} m_j^2\left(k\Delta z\right)}. \qquad (2.5.8)$$

where $m_j(k\Delta z)$ is the migrated sample for bin j and depth sample k,

K is the number of depth samples in the window.

In our algorithm, we first calculate the semblance inside a running window of, let's say 7 traces and 5 samples in depth, for a common-image gather. Then, we reject the data that have a semblance smaller than a predefined minimum value and keep those for which semblance value exceeds a predefined passing semblance value. The semblance will not only tend to be large when a coherent event is present, but the magnitude of the semblance will be sensitive to the amplitude of event. Semblance values approach 1 for highly coherent events while for incoherent events they approach 0.

Gardner *et al*. (1974) have described a similar method based on coherency to remove the migration tails. The difference is that they applied the filter to the data prior to the migration. In the future, we recommend implementing the semblance weighting factor inside the migration algorithm, before the inner migration loop.

We show a comparison between the common-image gathers, obtained by migrating the group of 14 shots vertical component, before and after semblance weighting (Figure 2.5.4). Note how most parts of the migration smiles are removed after applying semblance weighting. The migration output, for this 2-D scalar migration algorithm, is sorted in offset-azimuth bins. We applied a bandpass filter to the common-image gather (CIG) before applying the semblance weighting to remove very low frequency noise.

We display the images presented in Figure 2.5.3 after applying semblance weighting in Figure 2.5.5. Next, we migrated the synthetic shot-gathers, vertical and horizontal components, PP reflections only for 65 shots. We display the PP depth images after bandpass filter and semblance weighting in Figure 2.5.6.

After calibrating the PP prestack depth migration algorithm, we moved on to the PS scalar prestack depth migration algorithm. The algorithm remains the same like for the PP case. We used the same source traveltime calculated with the P-wave velocity but we used the receiver traveltime obtained using the S-wave velocity.

We followed a similar workflow analogous to that for PP migration. We started by migrating shot no. 2, vertical and horizontal components PS reflections only, and display the resulting PS depth images in Figure 2.5.7. Next, we generated the PS depth images for groups of 14 and 65 shots, both vertical and horizontal components. We show the PS depth image for group of 14 shots, both vertical and horizontal components, before applying the bandpass filter and semblance weighting in Figure 2.5.8. The arrow marks the location of the common-image gather, before and after semblance weighting, shown in Figure 2.5.9. In Figure 2.5.10, we present the resulting staked image for 14 shots after bandpass and semblance weighting. Next, we present the PS depth images obtained for 65 shots after applying semblance weighting in Figure 2.5.11.

Analysis of the 2-D PS VSP images confirms the observation that PS waves do not provide as good a lateral subsurface illumination of the sedimentary interfaces as PP waves. This small lateral subsurface illumination does not allow the constructive interference and semblance weighting during stacking to take place properly so, the PS depth images have more residual noise than PP depth images.

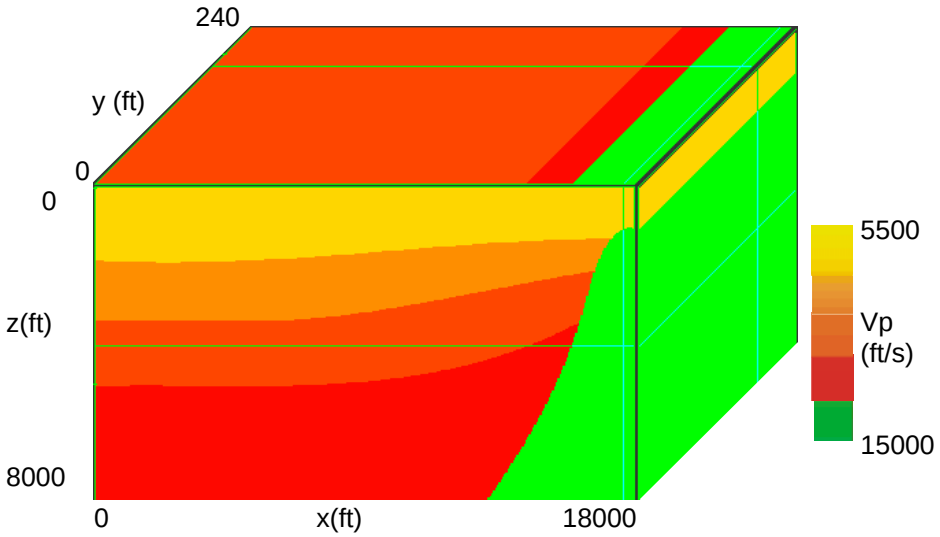

FIG. 2.5.1. 2.5-D velocity model used in migration. I only migrated one line corresponding to the 2-D velocity model used to generate the VSP synthetic data.

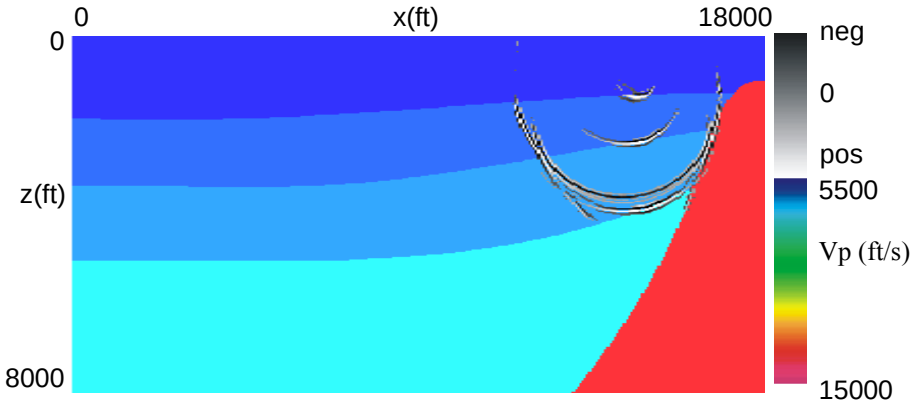

FIG. 2.5.2.(a). 2-D scalar PP pre-stack depth image, shot no.2, vertical component, overlying the P-wave velocity model.

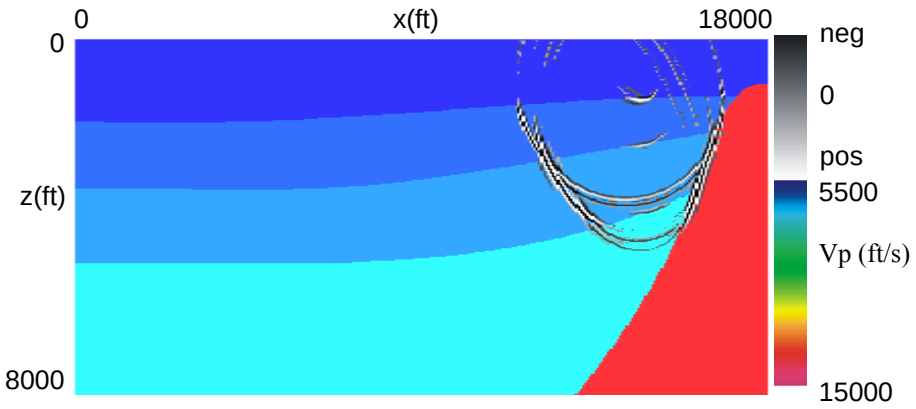

FIG. 2.5.2.(b). 2-D scalar PP pre-stack depth image, shot no.2, horizontal component, overlying the P-wave velocity model.

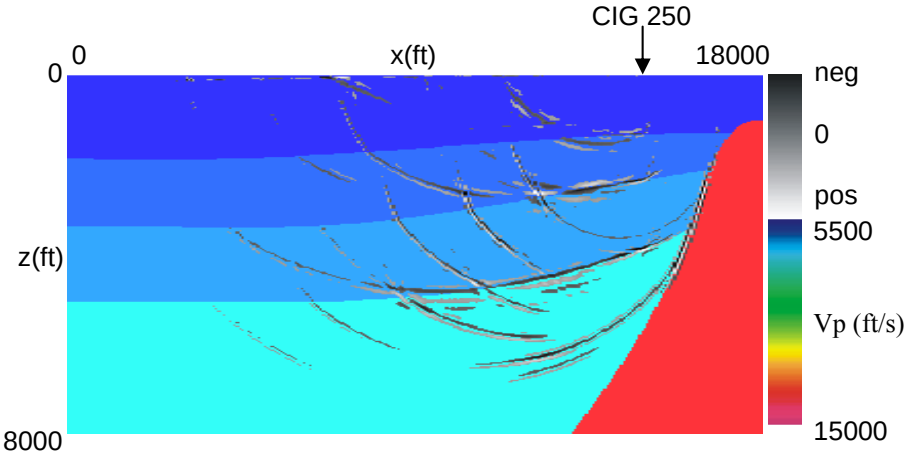

FIG. 2.5.3.(a). 2-D scalar PP pre-stack depth image, 14 shots, vertical component, overlying the P-wave velocity model. No semblance weighting applied. The arrow marks the location of the common-image gather presented in Figure 2.5.8.

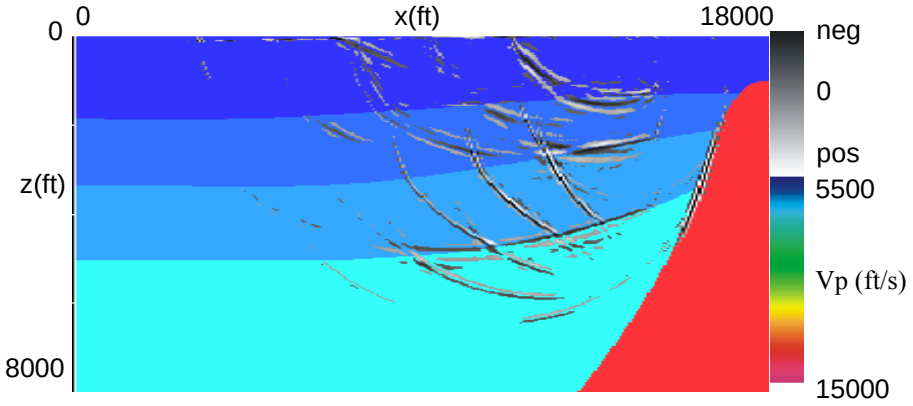

FIG. 2.5.3.(b). 2-D scalar PP pre-stack depth image, 14 shots, horizontal component, overlying the P-wave velocity model. No semblance weighting applied.

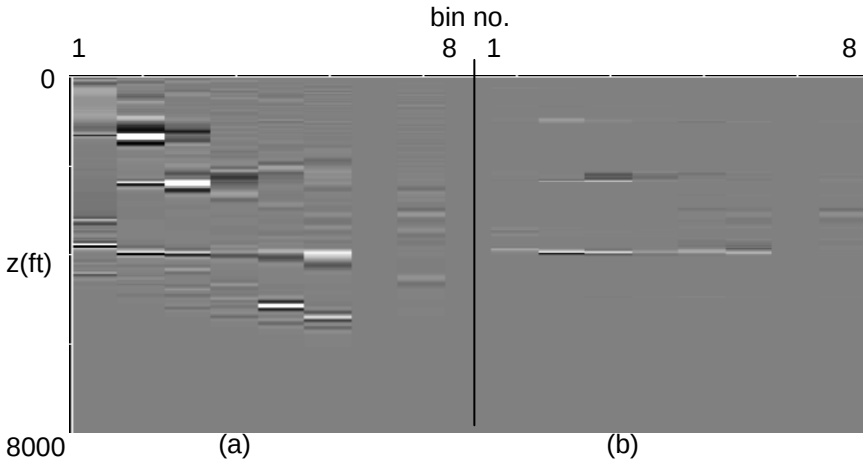

FIG. 2.5.4. Common-image gathers generated by migrating 14 shots, vertical component, PP events only. (a) before semblance weighting; (b) after BandPass and semblance weighting.

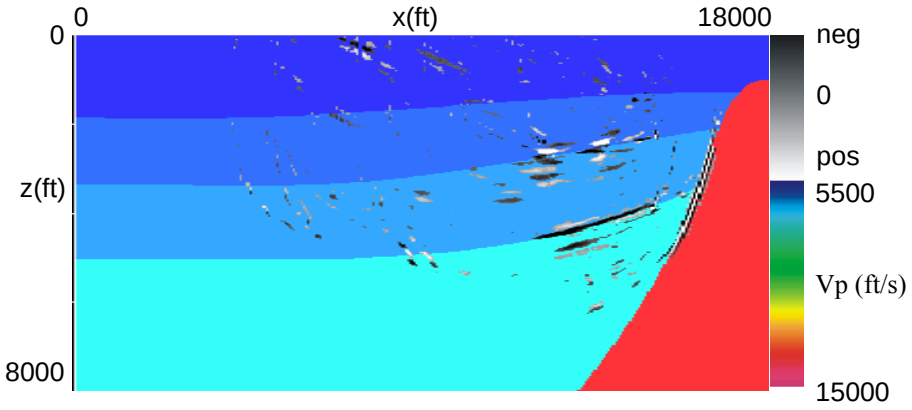

FIG. 2.5.5.(a). 2-D scalar PP pre-stack depth image, 14 shots, vertical component, overlying the P-wave velocity model. Semblance weighting applied.

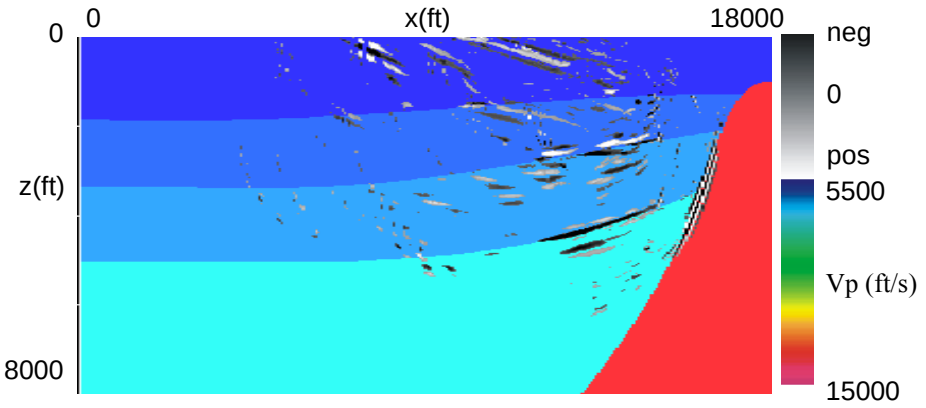

FIG. 2.5.5.(b). 2-D scalar PP pre-stack depth image, 14 shots, horizontal component, overlying the P-wave velocity model. Semblance weighting applied.

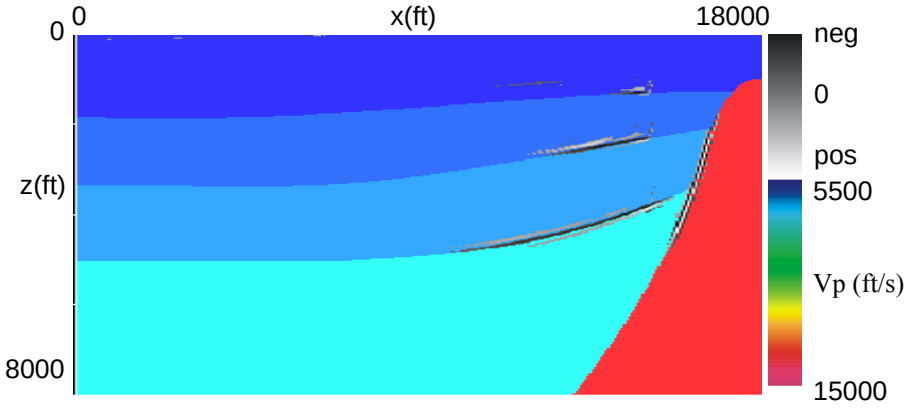

FIG. 2.5.6.(a). 2-D scalar PP pre-stack depth image, 65 shots, vertical component, overlying the P-wave velocity model. Semblance weighting applied.

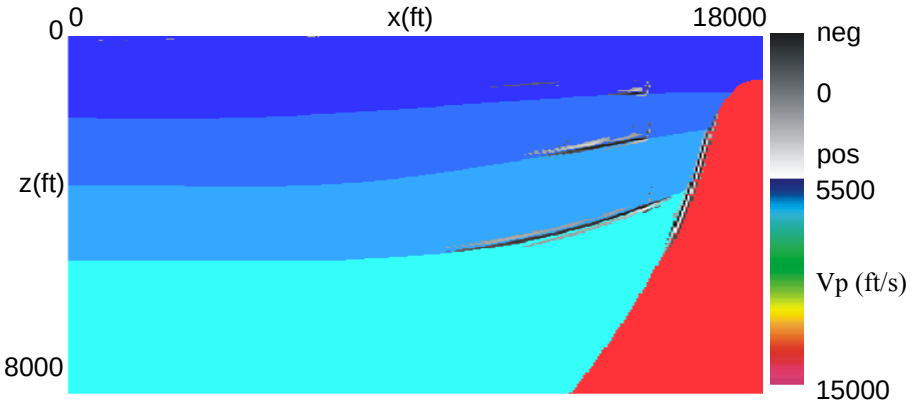

FIG. 2.5.6.(b). 2-D scalar PP pre-stack depth image, 65 shots, horizontal component, overlying the P-wave velocity model. Semblance weighting applied.

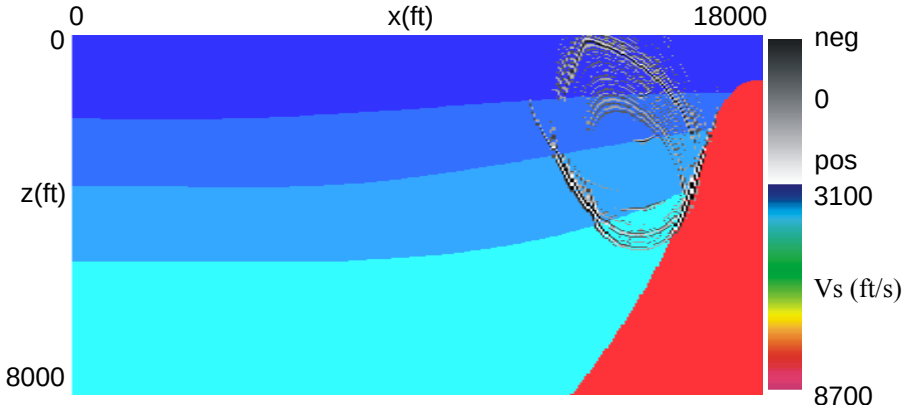

FIG. 2.5.7.(a). 2-D scalar PS pre-stack depth image, shot no.2, vertical component, overlying the S-wave velocity model.

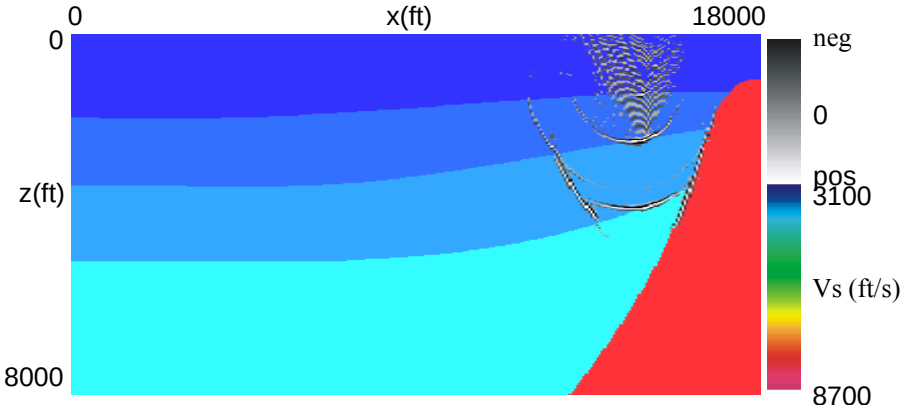

FIG. 2.5.7.(b). 2-D scalar PS pre-stack depth image, shot no.2, horizontal component, overlying the S-wave velocity model.

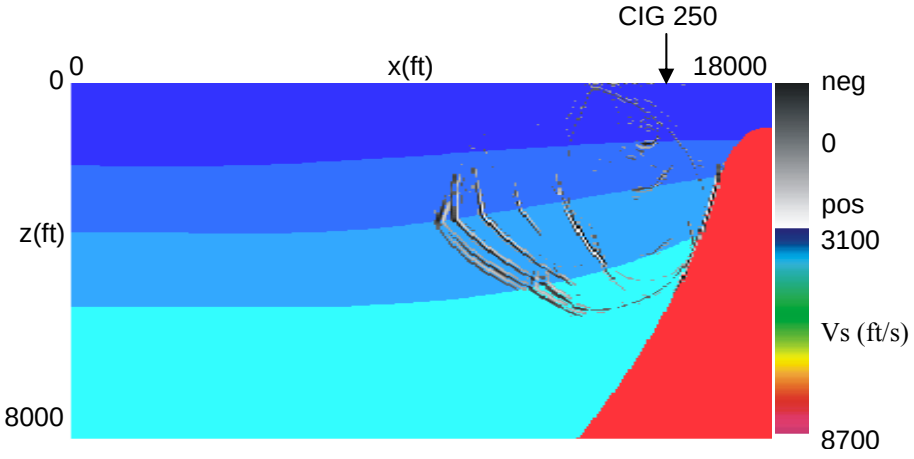

FIG. 2.5.8.(a). 2-D scalar PS pre-stack depth image, 14 shots, vertical component, overlying the S-wave velocity model. No semblance weighting applied. The arrow marks the location of the common-image gather presented in Figure 2.5.9.

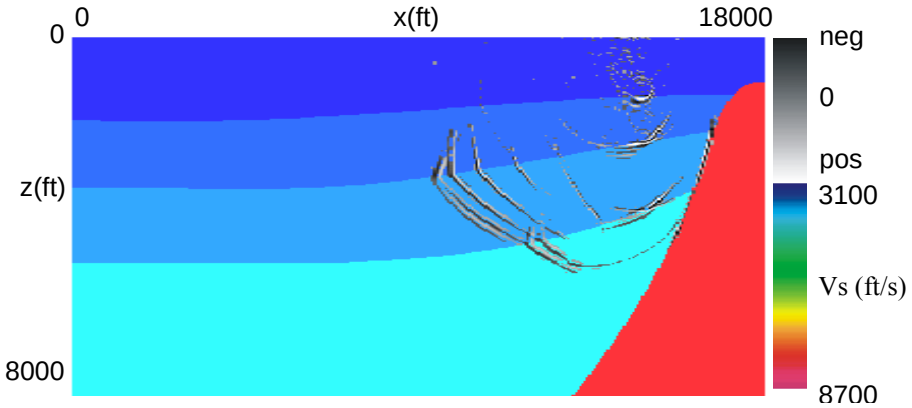

FIG. 2.5.8.(b). 2-D scalar PS pre-stack depth image, 14 shots, horizontal component, overlying the S-wave velocity model. No semblance weighting applied.

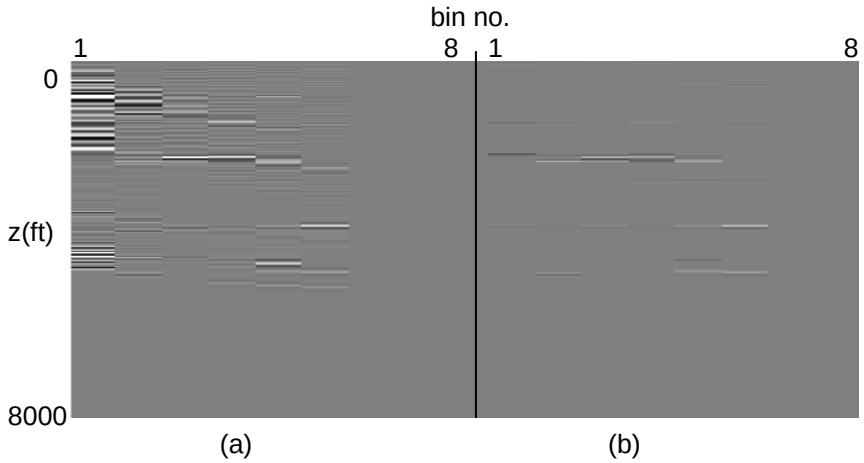

FIG. 2.5.9. Common-image gathers generated by migrating 14 shots, vertical component, PS events only. (a) before semblance weighting; (b) after BandPass and semblance weighting.

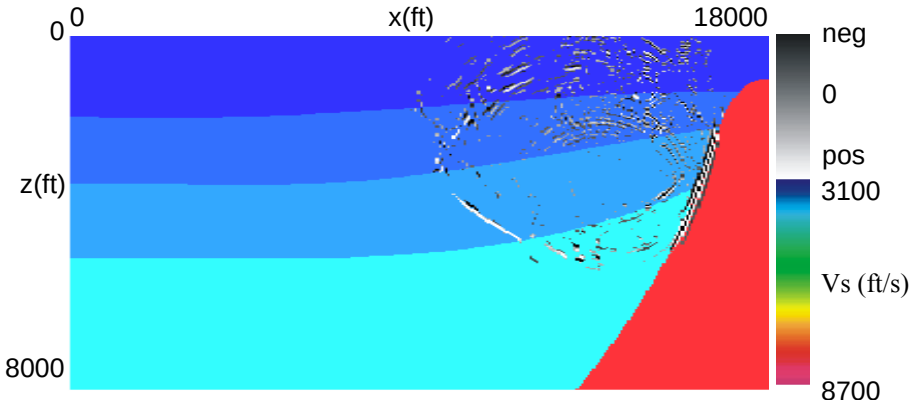

FIG. 2.5.10.(a). 2-D scalar PS pre-stack depth image, 14 shots, vertical component, overlying the S-wave velocity model. Semblance weighting applied.

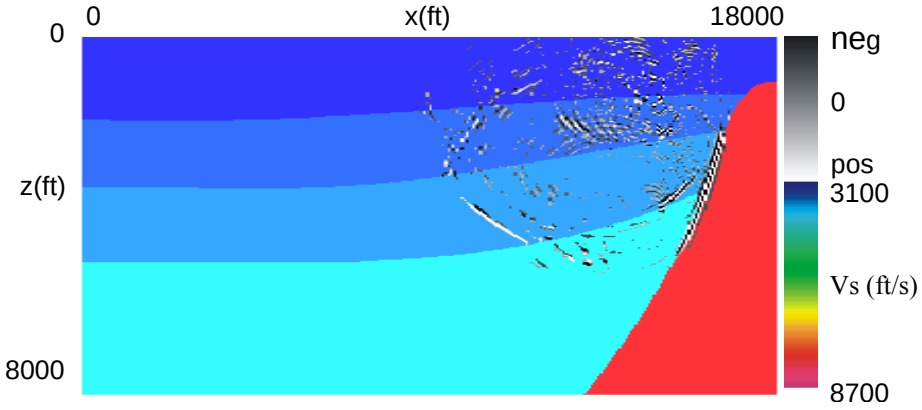

FIG. 2.5.10.(b). 2-D scalar PS pre-stack depth image, 14 shots, horizontal component, overlying the S-wave velocity model. Semblance weighting applied.

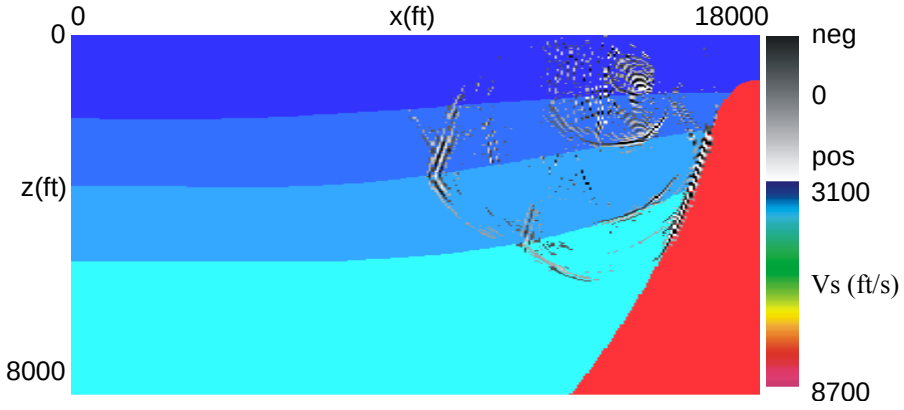

FIG. 2.5.11.(a). 2-D scalar PS pre-stack depth image, 65 shots, vertical component, overlying the S-wave velocity model. Semblance weighting applied.

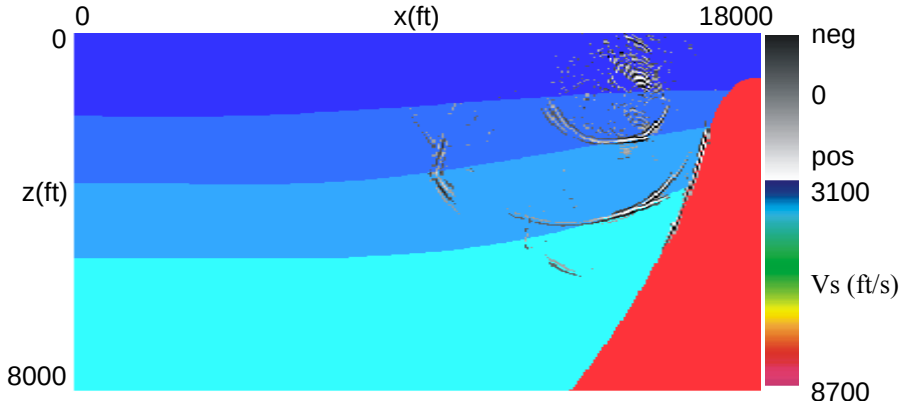

FIG. 2.5.11.(b). 2-D scalar PS pre-stack depth image, 65 shots, horizontal component, overlying the S-wave velocity model. Semblance weighting applied.

2-D VSP synthetic elastic Kirchhoff pre-stack depth migration

We used the same 2-D velocity model (Figure 2.5.12) to generate 2-D elastic VSP synthetic data via an in-house elastic pseudo-spectral modeling algorithm. We started by modeling one shot only, shot no.2 (Figure 2.5.13).

Synthetic VSP data have a reasonably high frequency, which is due to the small cell size of the velocity model. We used 15 ft (4.5 m) cell size that ensured a frequency of 75 Hz. The only pre-processing step we performed before elastic migration is muting the first-breaks. Based on the previous modeling results, the up-going/down-going wave separation prior to migration is not suitable for our project. We show the synthetic shot-gather displayed in Figure 2.5.13 after muting the first-breaks in Figure 2.5.14.

Based on the synthetic data, we observe that the salt flank reflection has a hyperbolic moveout in contrast to the linear moveout of the sedimentary boundaries. The PP salt flank reflection is stronger on the horizontal component than on the vertical component. The PS salt flank reflection appears to be stronger on the vertical component than on the horizontal component. In contrast the PP sediment reflections appear stronger on the vertical phone while PS sediment reflections appear stronger on the horizontal phone.

The VSP synthetic data obtained by elastic pseudo-spectral modeling are perturbed by artificial salt flank reflections that are stronger on the horizontal phone. These reflections are due to solving the wave equation at each grid point, which consider the salt flank having a “stair-step” shape instead of a smooth one (Figure 2.5.15).

In order to evaluate migration aliasing, we generated synthetic shot-gathers (vertical and horizontal components) for groups of 14 and 65 shots. We obtained the

groups of shots by maintaining the same minimum and maximum x source coordinates and decreasing the shot spacing from 1000 ft (304 m) to 200 ft (61 m).

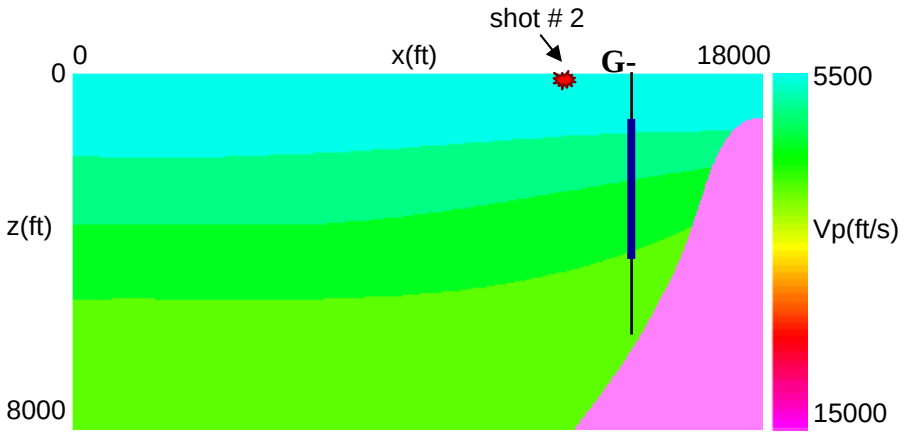

FIG. 2.5.12. Source location used to generate the synthetics. The red star indicates the shot location, offset = 1565 ft (477 m), which corresponds to shot no. 2 presented in the ray-traced data. The solid blue line indicates the VSP receiver array located between 943 and 3943 ft, with 50 ft receiver spacing.

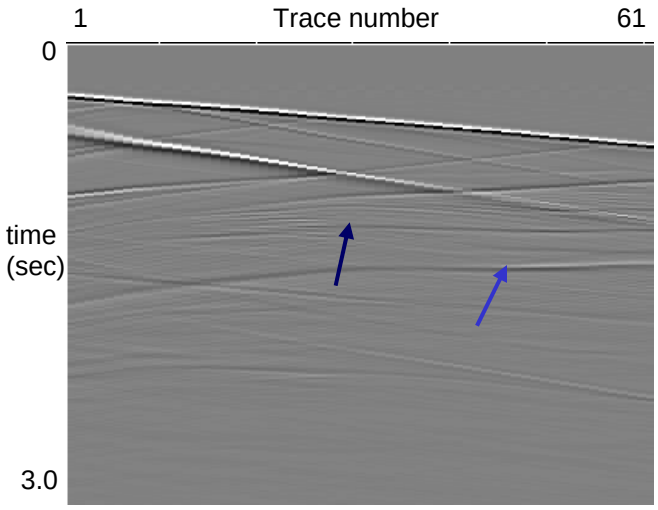

FIG. 2.5.13.(a). Synthetic shot-gather, vertical component, shot no. 2, offset = 1565 ft (477 m). Dark blue arrow points to the PP salt flank reflection, light blue arrow points to the PS salt flank reflection. Trace no. 1 corresponds to receiver no. 1 located at depth = 943 ft (287 m), trace no. 61 corresponds to receiver no. 61 located at depth = 3943 ft (1202 m), with receiver depth spacing = 50 ft (15 m).

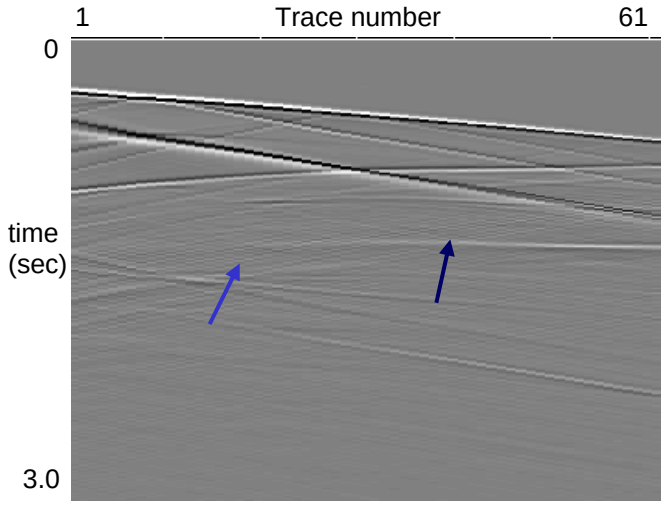

FIG. 2.5.13.(b). Synthetic shot-gather, horizontal component, shot no. 2, offset = 1565 ft (477 m). Dark blue arrow points to the PP salt flank reflection, light blue arrow points to the PS salt flank reflection. Trace no. 1 corresponds to receiver no. 1 located at depth = 943 ft (287 m), trace no. 61 corresponds to receiver no. 61 located at depth = 3943 ft (1202 m), with receiver depth spacing = 50 ft (15 m).

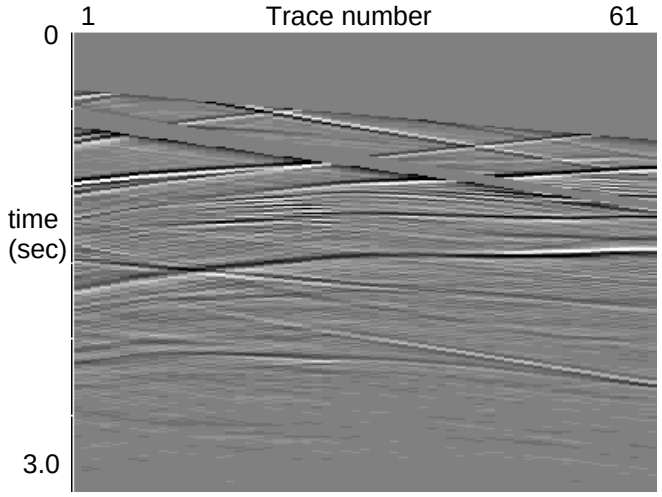

FIG. 2.5.14.(a). Synthetic shot-gather, vertical component, shot no. 2, offset = 1565 ft (477 m). First breaks muted. Trace no. 1 corresponds to receiver no. 1 located at depth = 943 ft (287 m), trace no. 61 corresponds to receiver no. 61 located at depth = 3943 ft (1202 m), with receiver depth spacing = 50 ft (15 m).

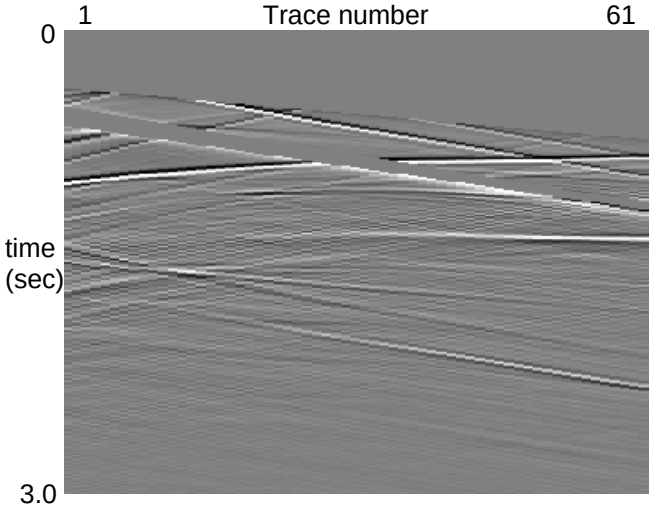

FIG. 2.5.14.(b). Synthetic shot-gather, horizontal component, shot no. 2, offset = 1565 ft (477 m). First breaks muted. Trace no. 1 corresponds to receiver no. 1 located at depth = 943 ft (287 m), trace no. 61 corresponds to receiver no. 61 located at depth = 3943 ft (1202 m), with receiver depth spacing = 50 ft (15 m).

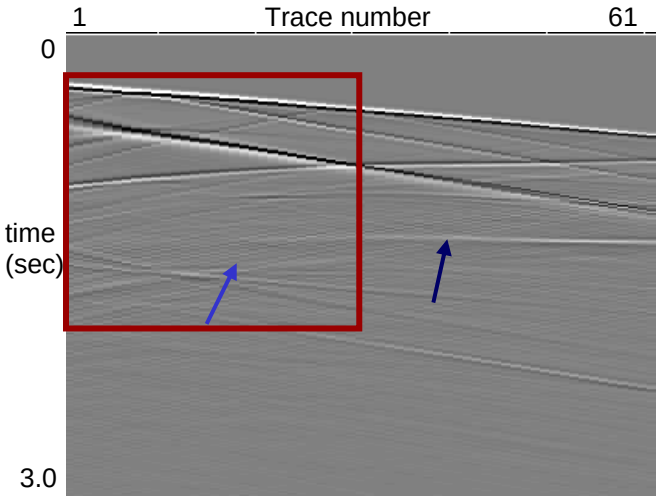

(a)

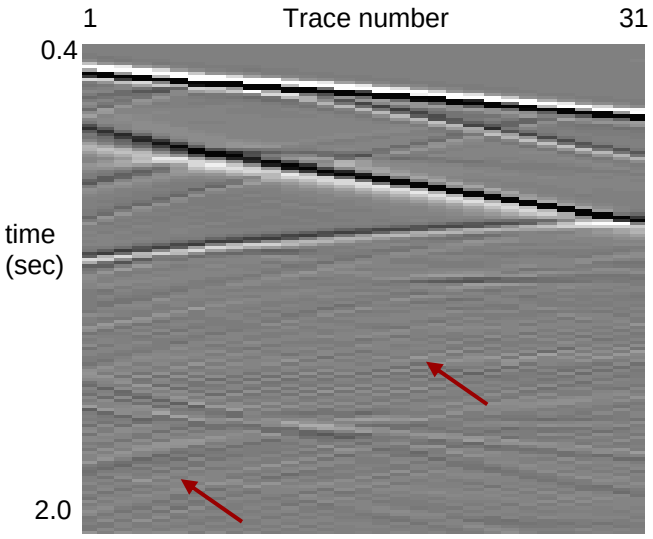

(b)

FIG. 2.5.15. (a) Synthetic shot-gather, horizontal component, shot no. 2, offset = 1565 ft (477 m). Dark blue arrow points to the PP salt flank reflection, light blue arrow points to the PS salt flank reflection. Red rectangle marks the zoomed area shown in Figure 5.2.2.1.4.b. Trace no. 1 corresponds to receiver no. 1 located at depth = 943 ft (287 m), trace no. 61 corresponds to receiver no. 61 located at depth = 3943 ft (1202 m), with receiver depth spacing = 50 ft (15 m).

(b) Zoomed area from (a), red arrows point to the artificial salt flank reflections.

Gherasim built her elastic migration algorithm based on Jackson's (1991) method who assumes the interaction between the wavefields occurs only once in the far-field of both source and receiver. Extraction of P, SV and SH wavefields is achieved within the depth migration (if we assume isotropy in the neighborhood of the downhole receiver) by a projection onto the polarization for the desired mode. The extraction of the desired mode is performed for each depth migration bin after the separate scalar migration of each receiver gather component. He obtained the expected polarization necessary for the post-migration projection via ray-tracing.

Gherasim also performed the elastic migration by projecting the data onto the expected polarization to separate the P- and S-waves. The difference is that, in her case, she performed the projection during the prestack depth migration.

We explain the idea of elastic migration in Figure 2.5.16. The red arrow represents the migration ray unit vector calculated using the direction cosines. The dot product between this migration ray vector and the VSP vector data give the P-waves, which are waves with particle displacement along the propagation direction, and the cross-product gives the S-waves, which are waves with particle displacement normal to the direction of propagation.

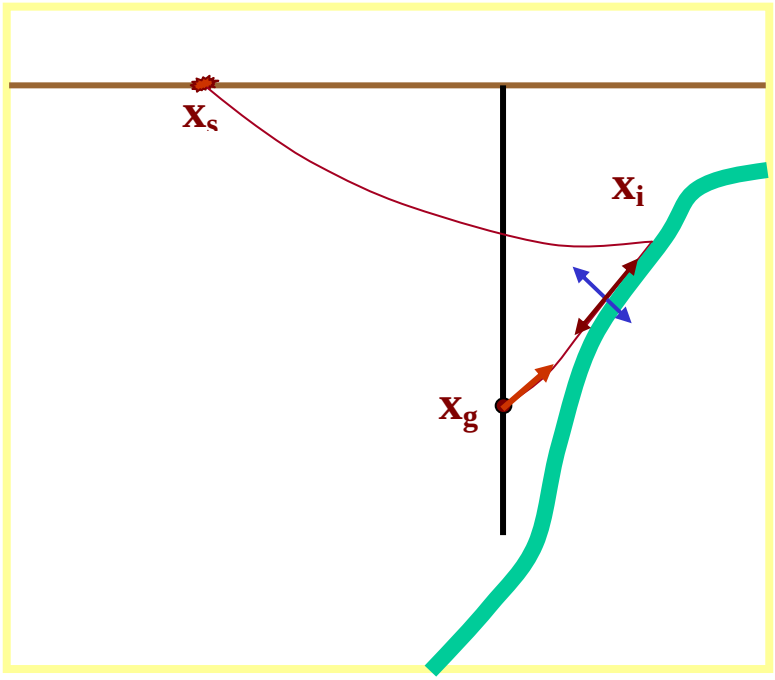

FIG. 2.5.16. Elastic migration using direction cosines. Red arrow represents the migration ray unit vector calculated using the direction cosines. Maroon double arrow represents the P polarization (along the direction of propagation) and the blue double arrow represents the S-wave polarization (perpendicular to the direction of propagation).

Gherasim used the same 3-D Kirchhoff pre-stack depth migration algorithm given by equation (2.5.9):

$$M_P(x) = \sum_{x_s, x_r} W(x_s, x_r, x) P(x_s, x_r, x) \qquad (2.5.9)$$

but where I have replace D_{sr} by P where P is given by:

$$P(x_s, x_r, x) = \hat{a} \bullet \overrightarrow{D_{sr}}\left(t_s(x_s, x) + t_r(x, x_r)\right). \qquad (2.5.10)$$

In these equations, $M_P(x)$ represents the PP-wave image at location x, $W(x_s, x_r, x)$ represents the same weighting factor used in the scalar migration, $\overrightarrow{D_{sr}}\left(t_s\left(x_s, x\right)+t_r\left(x, x_r\right)\right)$ represents the seismic data, and **â** represents the migration ray vector calculated using the direction cosines (Figure 2.5.17).

Gherasim calculated the direction cosines using the x, y and z coordinates of the image point and receivers, an approach that doesn't take into account any ray bending. An improvement is to incorporate a 3-D ray-tracing algorithm to obtain the ray take-off angle at the receivers. We expect less leakage of the S-waves into PP image and P-waves into PS image when using take-off angles computed via ray-tracing.

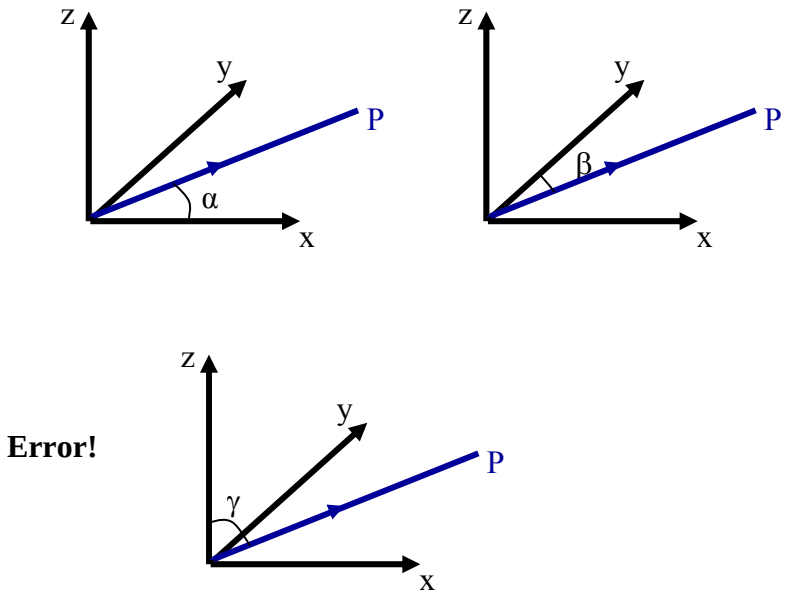

FIG. 2.5.17. Direction cosines of a vector in 3-D domain.

For PS image case, Gherasim use the following migration formula:

$$M_S(x) = \sum_{x_s, x_r} W(x_s, x_r, x) S(x_s, x_r, x) \qquad (2.5.11)$$

where

$$S(x_s, x_r, x) = \hat{a} \times \overrightarrow{D_{sr}}\left(t_s(x_s, x) + t_r(x, x_r)\right) \qquad (2.5.12)$$

and where $M_S(x)$ represents the PS-image at location x, $W(x_s, x_r, x)$ represents the same weighting factor used in the scalar migration, $\overrightarrow{D_{sr}}\left(t_s(x_s, x) + t_r(x, x_r)\right)$ represents the seismic data, and **â** represents the migration ray vector calculated using the direction cosines.

Wang (2004) has presented a 3-D 3-C VSP pre-stack Kirchhoff migration, which also uses the dot product inside the migration loop. His algorithm uses a dynamic, vector energy mapping method to image a reflection position and maps each time sample only to its reflected image point. An advantage of this method is that it doesn't require a rotation of the data to a preferred orientation prior migration. The dynamic rotation of the data allows the migration to use directional mapping and therefore distribute the reflection energy only to its true reflection position. This enhances reflection images and reduces noise in the image.

To calibrate the elastic Kirchhoff migration algorithm, we followed a workflow analogous to the scalar migration case. The advantage of Kirchhoff pre-stack depth migration is that we can use the same traveltime sections that we already calculated for the scalar migration case.

We first tested the program using shot no. 2, vertical and horizontal components, and generate PP and PS elastic depth images. We display the images in Figure 2.5.18. The elastic pre-stack depth migration suffers from similar types of aliasing like the pre-stack scalar depth migration. Since earlier we provided a detailed explanation of "Data Aliasing" and "Operator Aliasing" for the 2-D scalar pre-stack depth migration case, we will directly present the results of the elastic pre-stack depth imaging of groups of 14 and 65 shots. The migration output, for this 2-D elastic migration algorithm, is sorted in offset-azimuth bins.

We show the PP and PS elastic depth images generated for the group of 14, before applying the bandpass filter and semblance weighthing, in Figure 2.5.19. The arrows mark the location of the common-image gathers presented in Figure 2.5.20 – 2.5.21. As we can see from these figures, the incoherent noise seen in common-image gathers before using the bandpass filter and the semblance weighting is suppressed. In Figure 2.5.22, I present the 2-D elastic PP and PS depth images for 14 shots after bandpass filter and semblance weighting.

Next, we show depth images obtained for the group of 65 shots before bandpass and semblance weighting (Figure 2.5.23). The arrow marks the location of the common-image gathers presented in Figures 2.5.24 – 2.5.25, before and after bandpass and

semblance weighting. In Figure 2.5.26, we show the final 2-D PP and PS elastic depth images for 65 shots, after bandpass and semblance weighting.

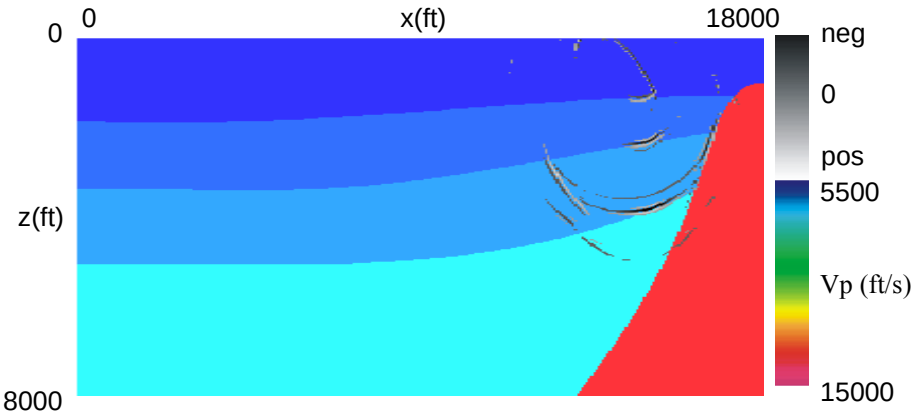

FIG. 2.5.18.(a). 2-D elastic PP pre-stack depth image, shot no.2, overlying the P-wave velocity model.

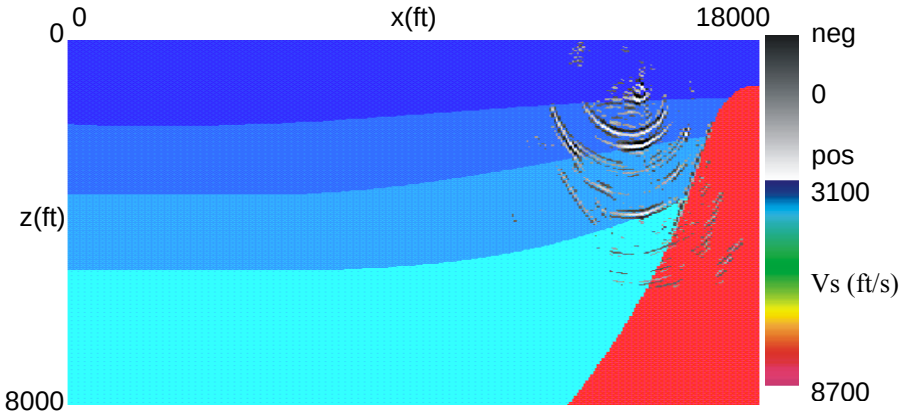

FIG. 2.5.18.(b). 2-D elastic PS pre-stack depth image, shot no.2, overlying the S-wave velocity model.

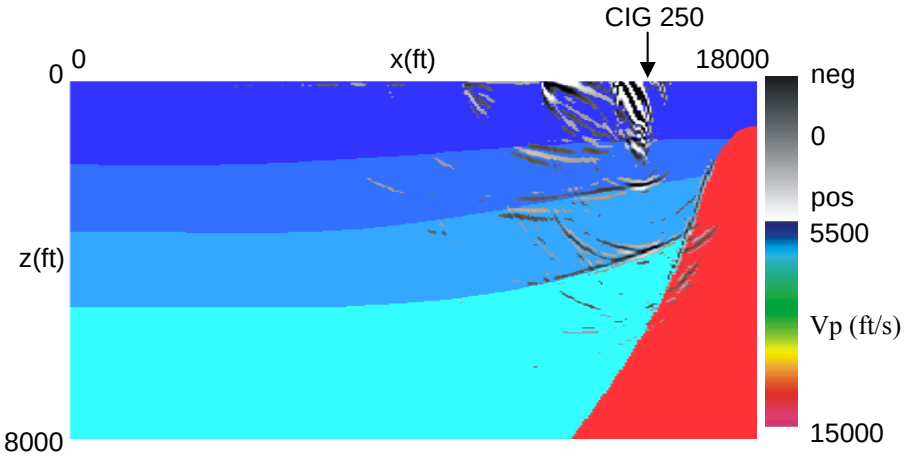

FIG. 2.5.19.(a). 2-D elastic PP pre-stack depth image, 14 shots, overlying the P-wave velocity model. No bandpass and semblance weighting applied.

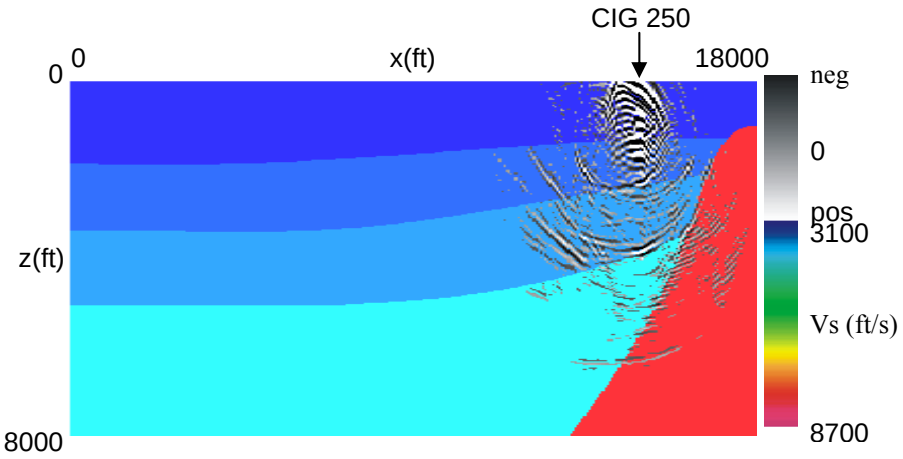

FIG. 2.5.19.(b). 2-D elastic PS pre-stack depth image, 14 shots, overlying the S-wave velocity model. No bandpass and semblance weighting applied. Note the high-frequency migration artifacts located along the salt flank, generated by the artificial salt flank reflection.

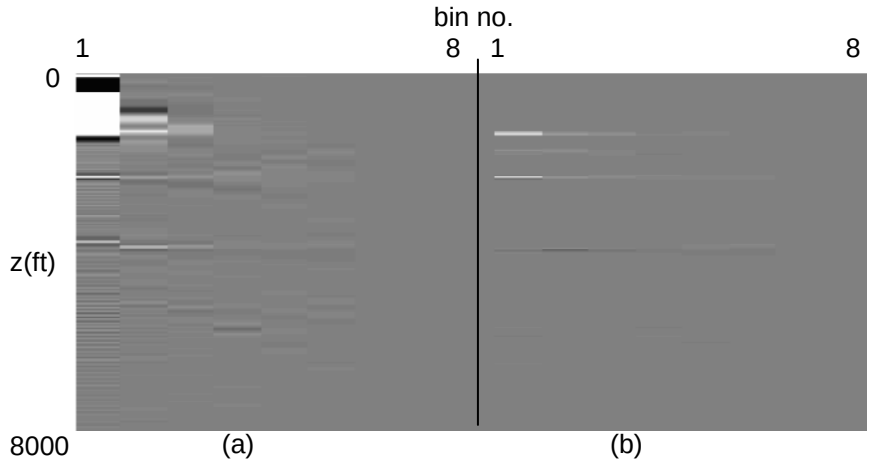

FIG. 2.5.20. Common-image gathers before and after bandpass and semblance weighting generated by elastic PP migration of 14 shots. (a) before bandpass and semblance weighting, (b) after bandpass and semblance weighting

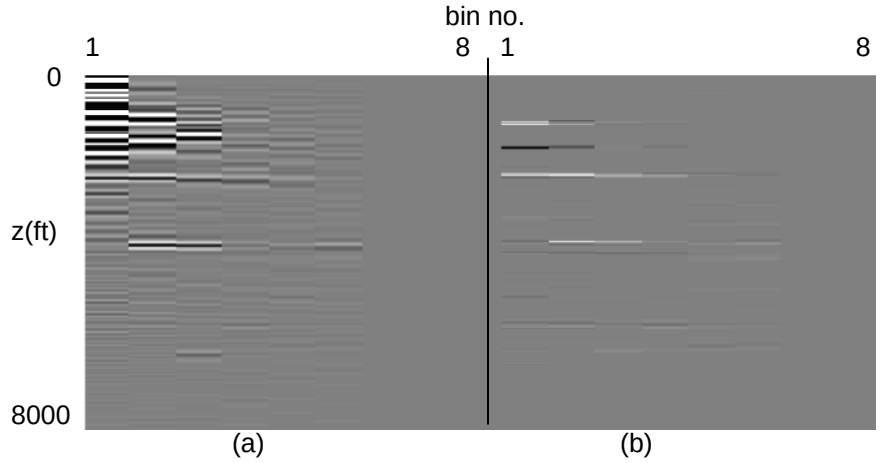

FIG. 2.5.21. Common-image gathers before and after bandpass and semblance weighting generated by elastic PS migration of 14 shots. (a) before bandpass and semblance weighting, (b) after bandpass and semblance weighting

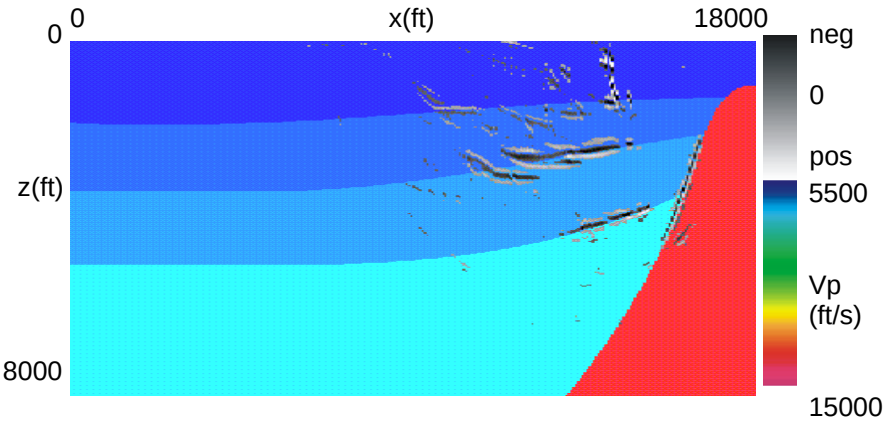

FIG. 2.5.22.(a). 2-D elastic PP pre-stack depth image, 14 shots, overlying the P-wave velocity model. Bandpass and semblance weighting applied.

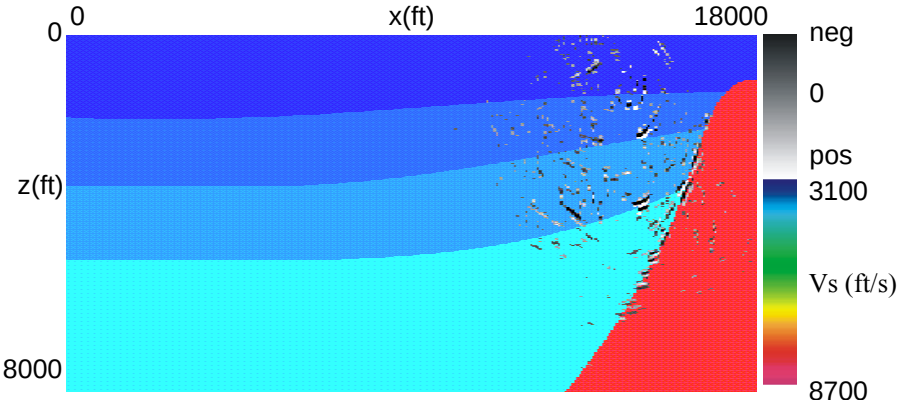

FIG. 2.5.22.(b). 2-D elastic PS pre-stack depth image, 14 shots, overlying the S-wave velocity model. Bandpass and semblance weighting applied.

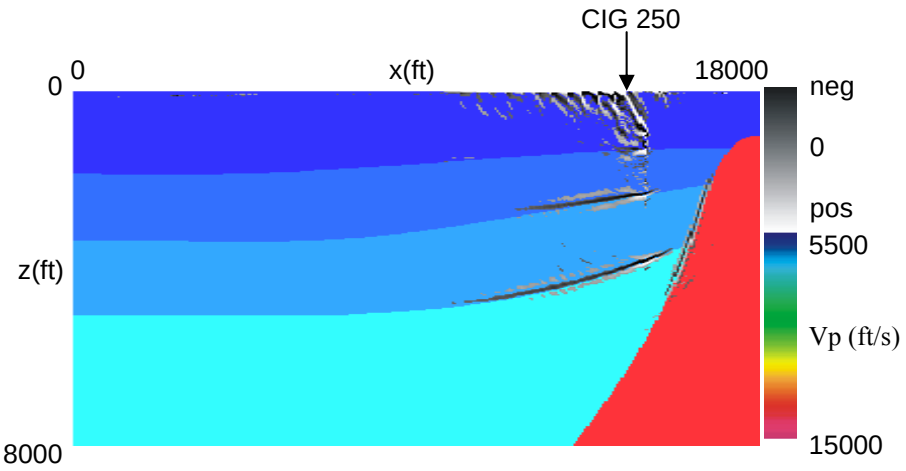

FIG. 2.5.23.(a). Elastic 2-D PP depth image, 65 shots, overlying P-wave velocity model. No semblance weighting applied. Note the migration artifacts present in the shallow part of the image, which are due to parts of first breaks left in the common-shot gathers.

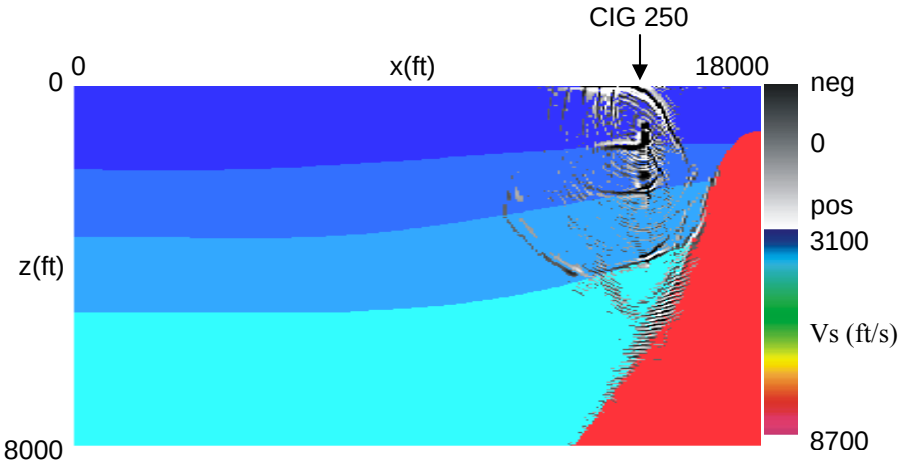

FIG. 2.5.23.(b). Elastic 2-D PS depth image, 65 shots, overlying S-wave velocity model. No semblance weighting applied. Note the migration artifacts present in the shallow part of the image, which are due to parts of first breaks left in the common-shot gathers. Note the high-frequency artifacts due to the artificial salt flank reflections. The arrow marks the location of the common-image gather displayed in Figure 2.5.24.

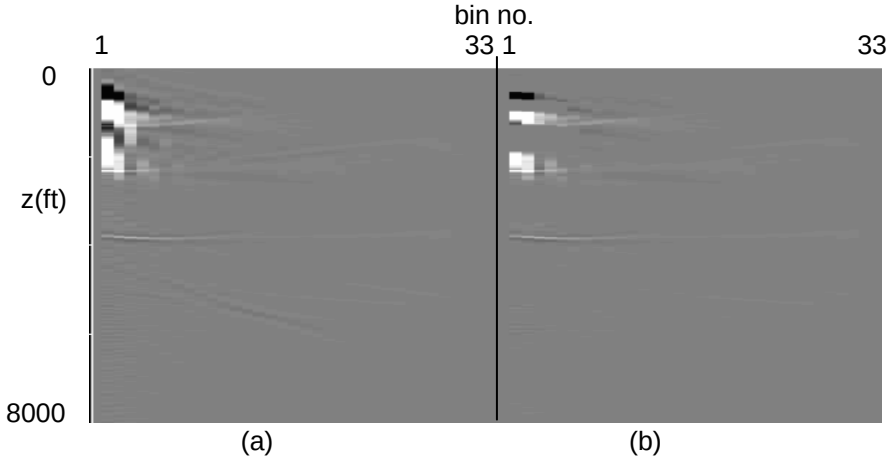

FIG. 2.5.24. Common-image gathers resulting from the elastic PP migration of 65 shots, before and after bandpass filter and semblance weighting. The migration artifacts present in the shallow part of the gather and small offsets are due to parts of first breaks left in common-shot gathers. Note the absence of the incoherent events from the common-image gather obtained after applying semblance weighting.

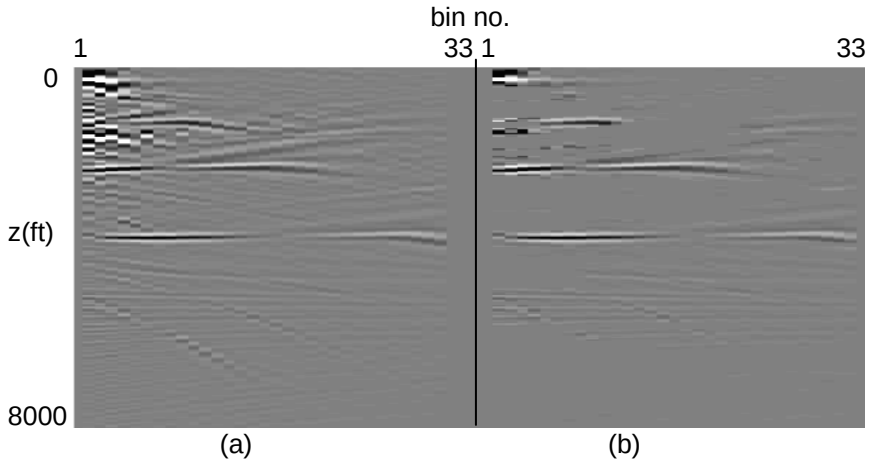

FIG. 2.5.25. Common-image gathers resulting from the elastic PS migration of 65 shots, before and after bandpass filter and semblance weighting. The migration artifacts present in the shallow part of the gather and small offsets are due to parts of first breaks left in common-shot gathers. Note the absence of the incoherent events from the common-image gather obtained after semblance weighting.

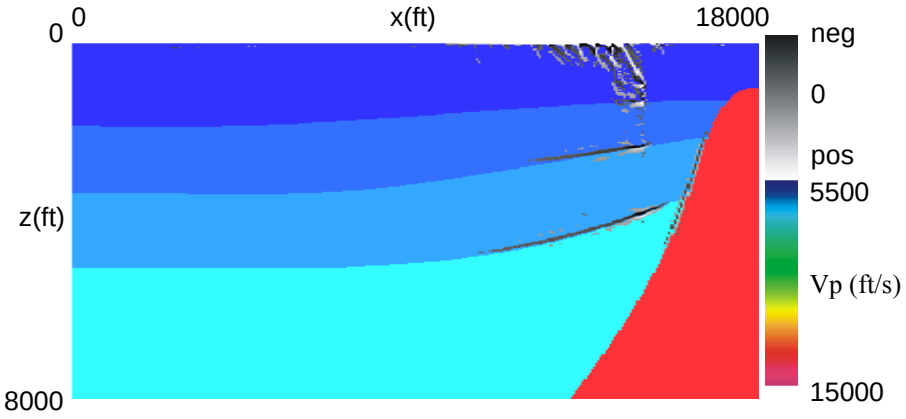

FIG. 2.5.26.(a). Elastic 2-D PP depth image, 65 shots, overlying P-wave velocity model. Note the migration artifacts present in the shallow part of the image, which are due to parts of first breaks left in the common-shot gathers. Band pass and semblance weighting applied.

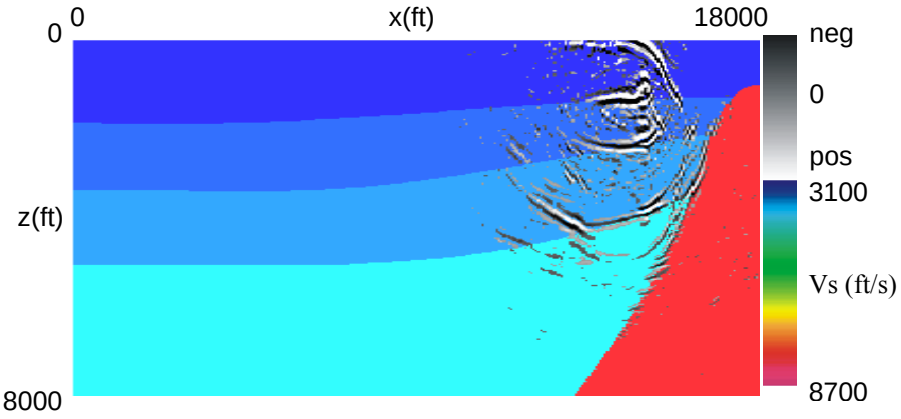

FIG. 2.5.26.(b). Elastic 2-D PS depth image, 65 shots, overlying S-wave velocity model. Note that the high-frequency migration artifacts are removed. Bandpass and semblance weighting applied.

3-D 3-C VSP Kirchhoff pre-stack depth migration – Vinton Dome, Louisiana

We followed the same workflow like for the synthetic case. We started by performing elastic PP and PS depth migration on a single common-shot gather, shot no. 3068. We present the elastic PP and PS depth images in Figure 2.5.27. We also chose to sort the migration output with respect to the receiver depth, grouping 5 receivers into one bin.

Based on the 2-D and 3-D modeling results, we know that the VSP subsurface illumination concentrates around the well location, so we created the depth images only for a small cube located around the VSP well. The dimensions of the VSP velocity model are 21600 ft x 21000 ft x 8000 ft (6585 x 6402 x 2439 m), while the dimensions of the output image volume are 12600 x 4800 x 8000 ft (3840 x 1463 x 2439 m). Since the subsurface illumination doesn't extend too much laterally, we expect a low constructive interference away from the well that allows the presence of the migration smiles in the final image.

To test the data aliasing problem, we selected a group of shots located along a radial line and a concentric arc marked by red stars in Figures 2.5.28 – 2.5.29. We generated elastic PP and PS depth images without (Figure 2.5.30 – 2.5.31) and with semblance-weighting factor (Figure 2.5.32 – 2.5.33). We also show an example of PP and PS common-image gathers before and after semblance weighting (Figure 2.5.34). Analysis of the depth images indicated that the PP and PS depth images generated for the concentric arc case shows a better continuity of the reflectors than in 2-D radial line case.

Next, we selected a group of 600 shots marked by the red polygon in Figure 2.5.35 with offset varying between 500 ft (152 m) and 15000 ft (4573 m) and generated elastic PP and PS depth images (Figure 2.5.36). The thin green lines mark the location of the inline, crossline and depth slices intersecting at the level of the first receiver in the well.

As specified in the previous sections, semblance weighting factor proves to be efficient in removing parts of the migration smiles. We can remove more or less incoherent energy from the image-gathers by selecting different values for the "semb_cut" and "semb_pass" parameters. "Semb_cut" represent the minimum semblance value of the removed data and "semb_pass" represents the minimum semblance value of the preserved data. The events with a lower semblance value than "semb_cut" will be removed and with a higher semblance values than "semb_pass" will be preserved. We present an example of common-image gathers before and after semblance weighting in Figure 2.5.37 and the final elastic PP and PS depth images, after semblance weighting, in Figure 2.5.38.

The elastic PP depth image shows a better continuity of the reflectors compared to the elastic PS depth image. One problem we noticed in the final depth image is the lack of continuity of the shallow reflectors, which is due to muting the first breaks. One way to improve the quality of the depth images is using another solution to first break removal instead of muting. The first break removal does not pose a problem when applying up-going/down-going separation filter. We performed the wavefield separation on the field common-shot gathers via f-k filter. We present the PP and PS depth images for the group

of 600 shots, up-going events only, after semblance weighting, in Figure 2.5.39. We noticed an improved image of the shallow reflectors.

To calibrate my VSP depth images we checked the similarity between my PP VSP elastic depth migrated volume with Warren Duncan's PP scalar depth migrated volume generated using surface data (Duncan, 2005). We noticed quite a good similarity at the VSP well location between those two depth migrated volumes. We also interpreted a few horizons on the surface migrated volume and plotted the picks on the VSP migrated volume, picks that matched perfectly with the surface migrated volume. We display a section through the surface and VSP depth migrated volumes, located at the VSP well, showing the interpreted horizons in Figure 2.5.40.

An extra piece of information present on the VSP images represents the reflectors marked by the red arrows, which might indicate the salt flank image. Previous information (Duncan, 2005) suggest a "Christmas-tree" shape of the salt dome, shape that We consider is confirmed by the portion of the image located around 3000 - 4000 ft (915 – 1220 m). If accurate, this "Christmas-tree" shape of the salt dome will make the salt flank imaging more difficult.

a)

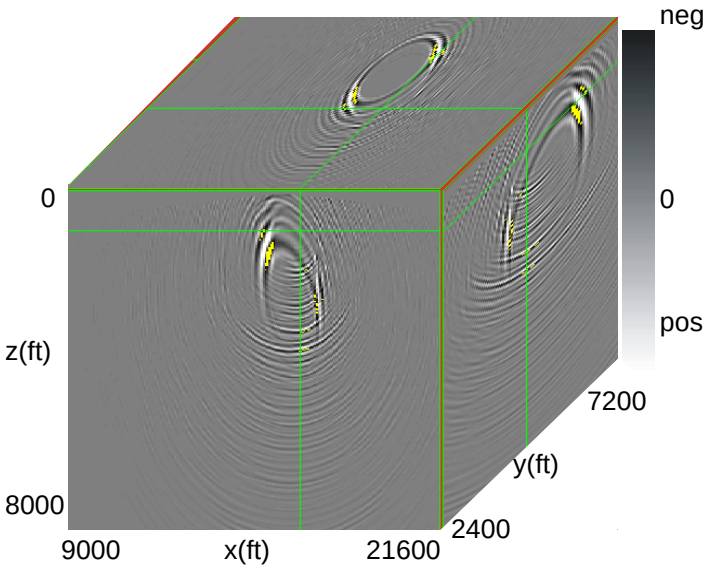

b)

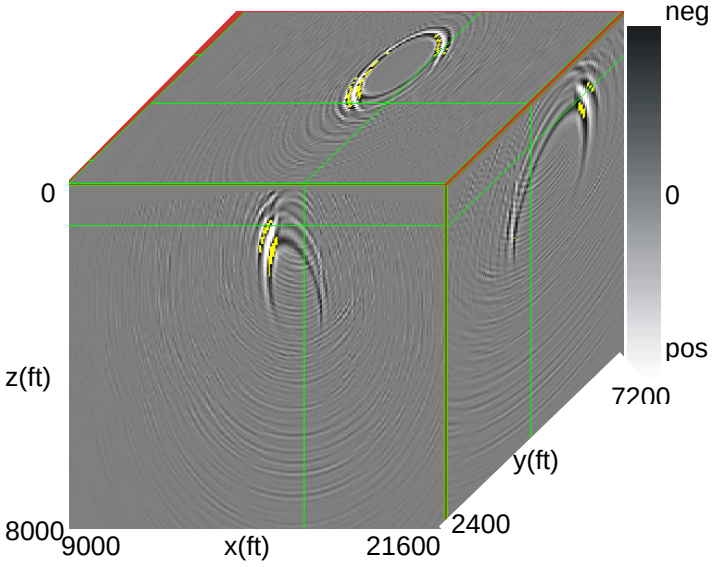

FIG. 2.5.27. a) 3-D PP elastic depth image; b) 3-D PS elastic depth image. Shot no. 3068, offset = 1989 ft (606 m). No semblance weighting applied. The migration artifacts present in the shallow part of the image, relatively closed to the well location, are due to multiples and leaks of first breaks. Green lines represent the inline, crossline and depth slices intersecting at the receiver no. 1 location.

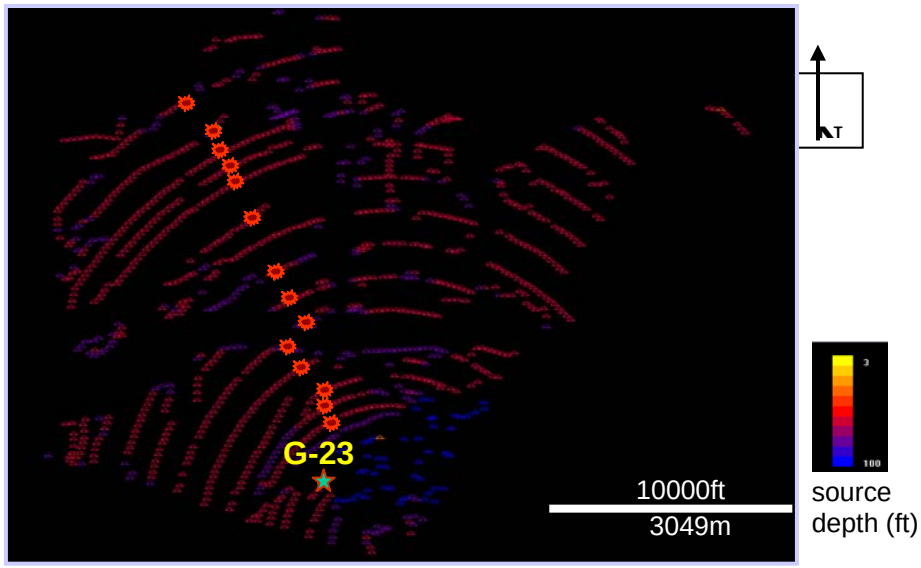

FIG. 2.5.28. Mapview of field sources recorded by the G-23 VSP well. Red stars mark a group of 14 shots located along a radial line used in migration.

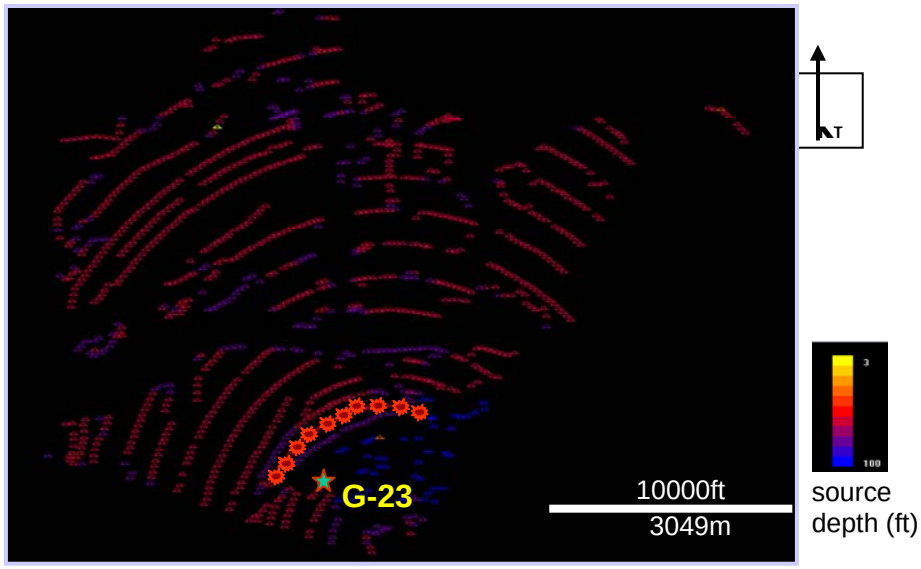

FIG. 2.5.29. Mapview of field sources recorded by the G-23 VSP well. Red stars mark a group of 36 shots located along a concentric arc used in migration.

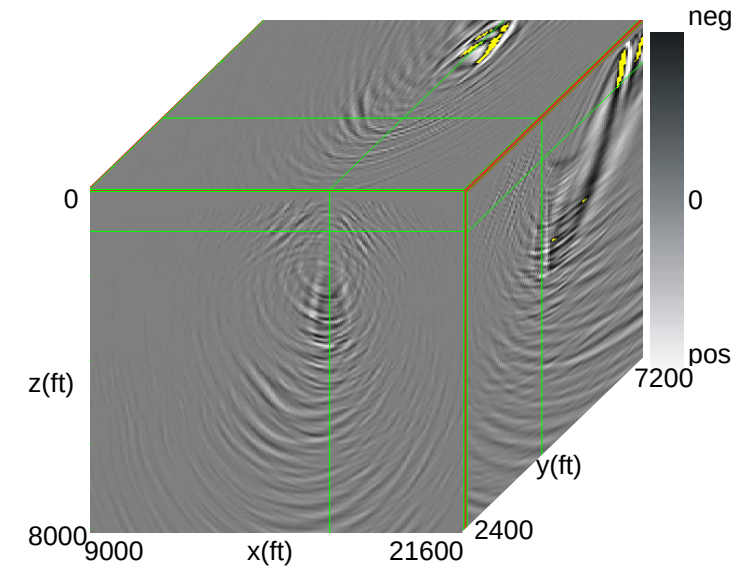

(a)

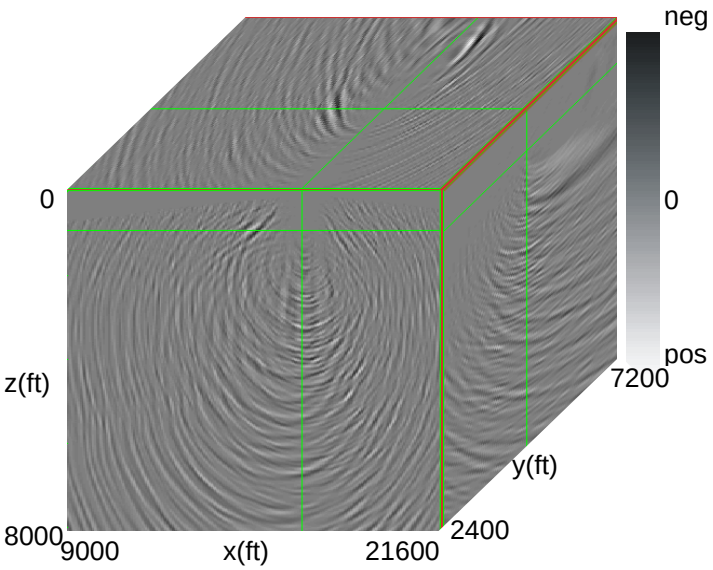

(b)

FIG. 2.5.30. (a) 3-D PP elastic depth image; (b) 3-D PS elastic depth image. 14 shots migrated. Green lines represent the inline, crossline and depth slices intersecting at the receiver no. 1 location. No semblance weighting applied.

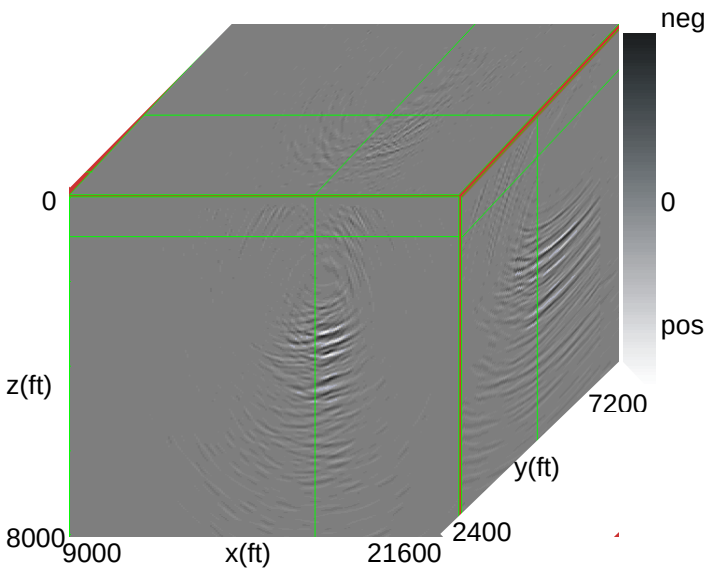

(a)

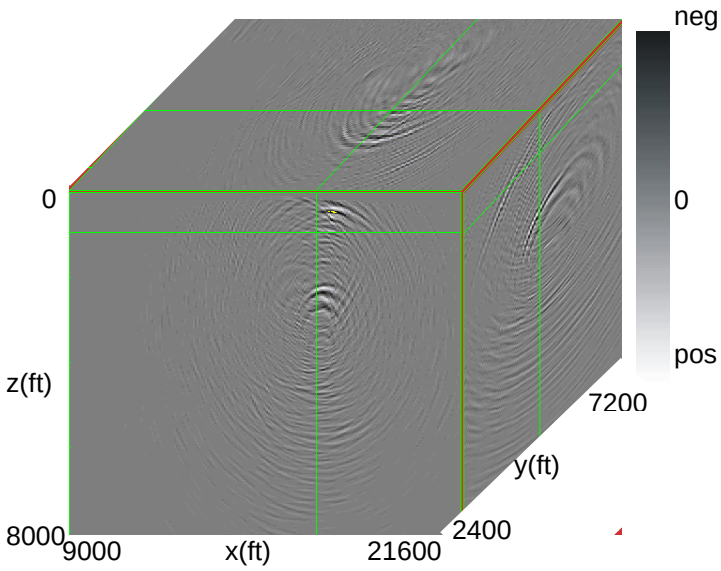

(b)

FIG. 2.5.31. (a) 3-D PP elastic depth image; (b) 3-D PS elastic depth image. 36 shots migrated. Green lines represent the inline, crossline and depth slices intersecting at the receiver no. 1 location. No semblance weighting applied.

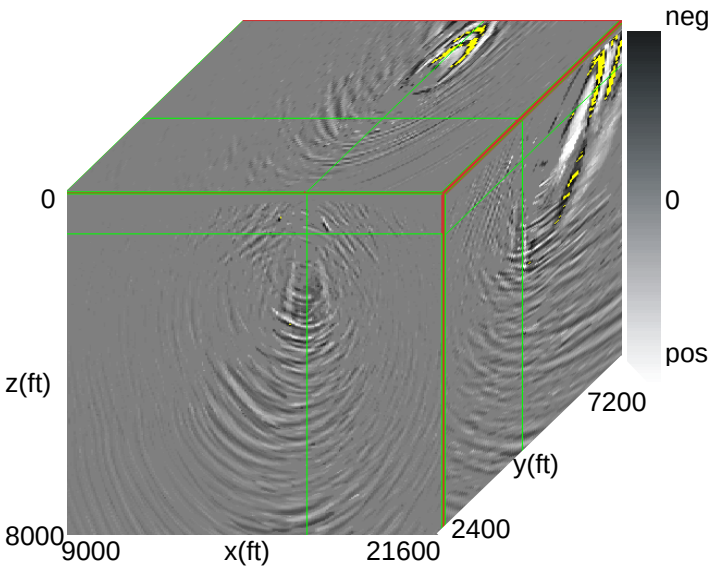

(a)

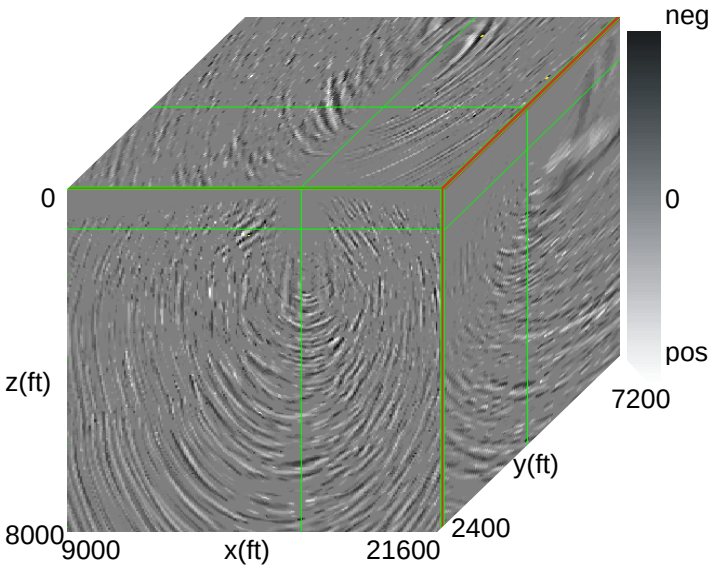

(b)

FIG. 2.5.32. (a) 3-D PP elastic depth image; (b) 3-D PS elastic depth image. 14 shots migrated. Green lines represent the inline, crossline and depth slices intersecting at the receiver no. 1 location. Semblance weighting applied.

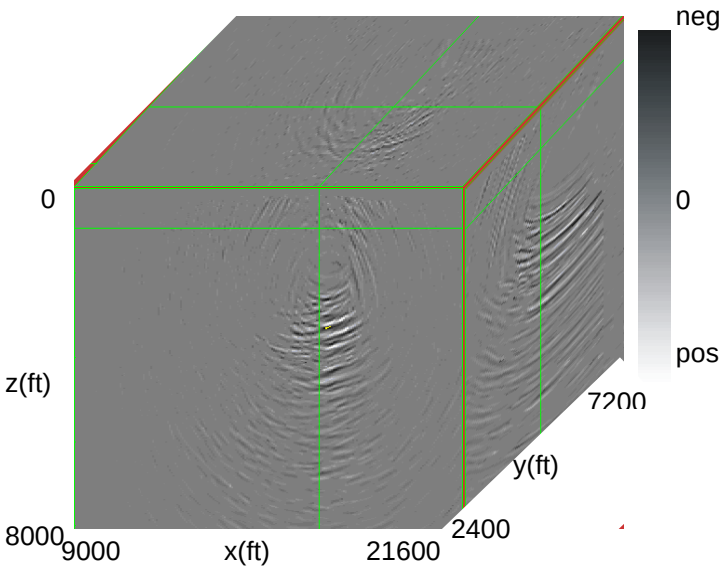

(a)

b)

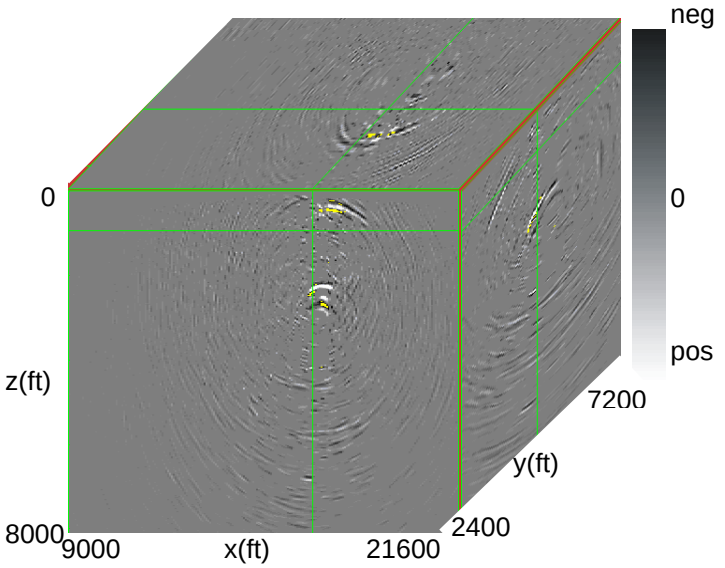

(b)

FIG. 2.5.33. (a) 3-D PP elastic depth image; (b) 3-D PS elastic depth image. 36 shots migrated. Green lines represent the inline, crossline and depth slices intersecting at the receiver no. 1 location. Semblance weighting applied.

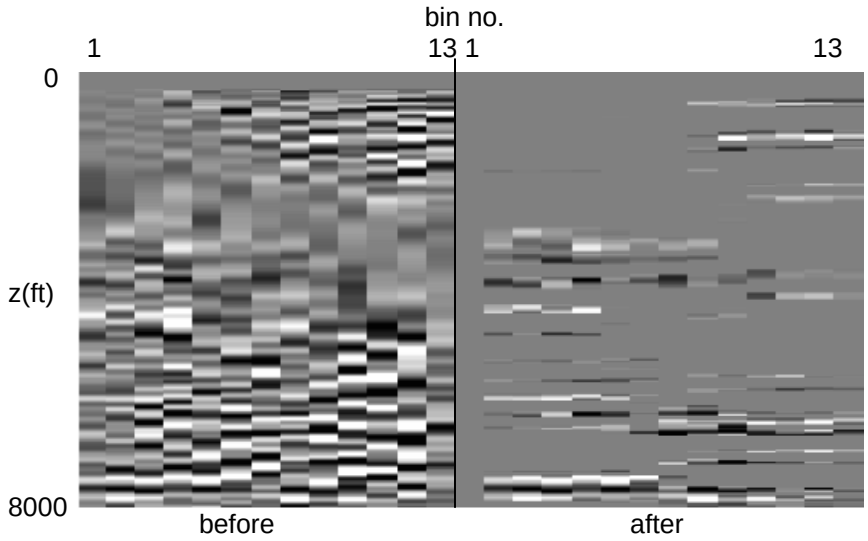

(a)

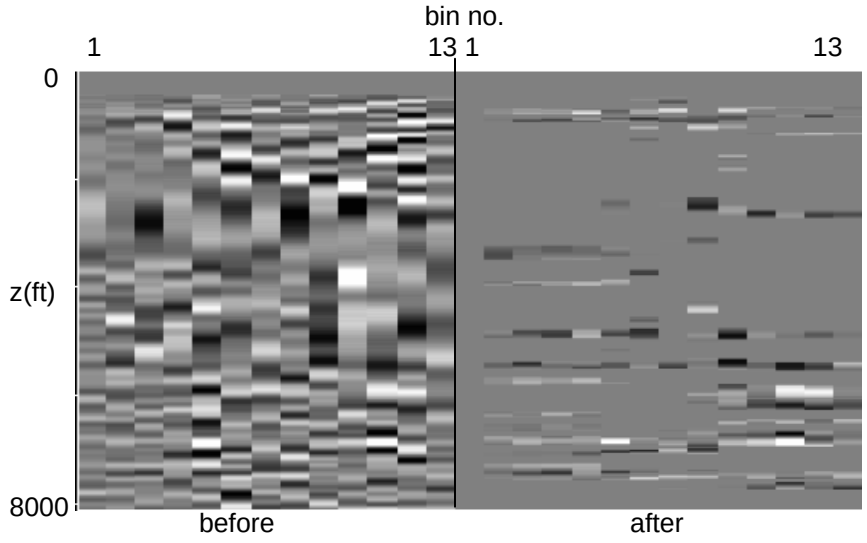

(b)

FIG. 2.5.34. (a) PP common-image gathers; (b) PS common-image gathers before and after applying semblance weighting stacking. 14 shots migrated. Note how most of the incoherent events are removed.

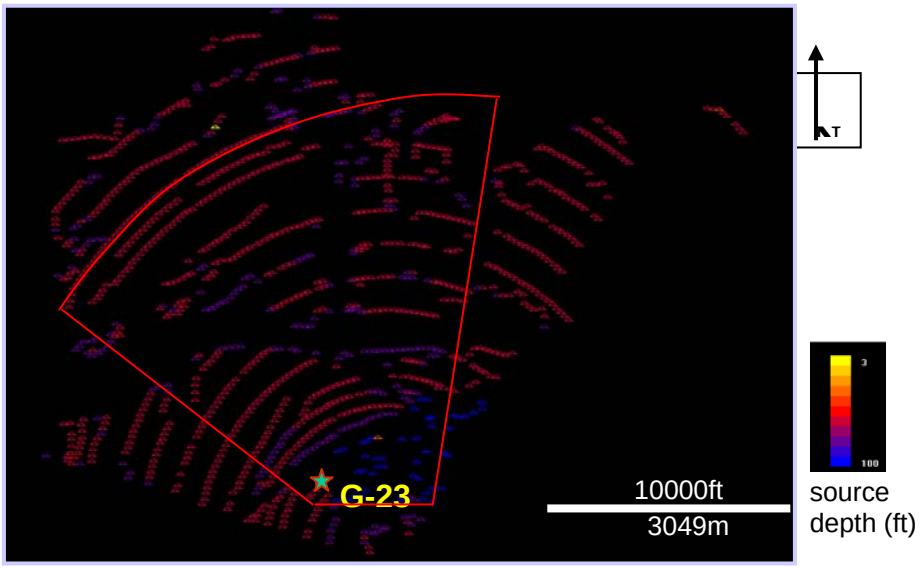

FIG. 2.5.35. Mapview of field sources recorded by the G-23 VSP well. Red polygon mark a group of 600 shots used in migration.

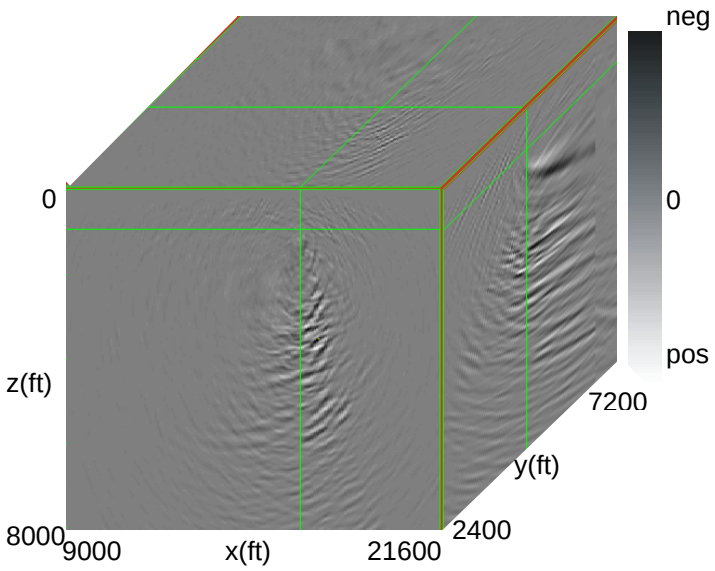

(a)

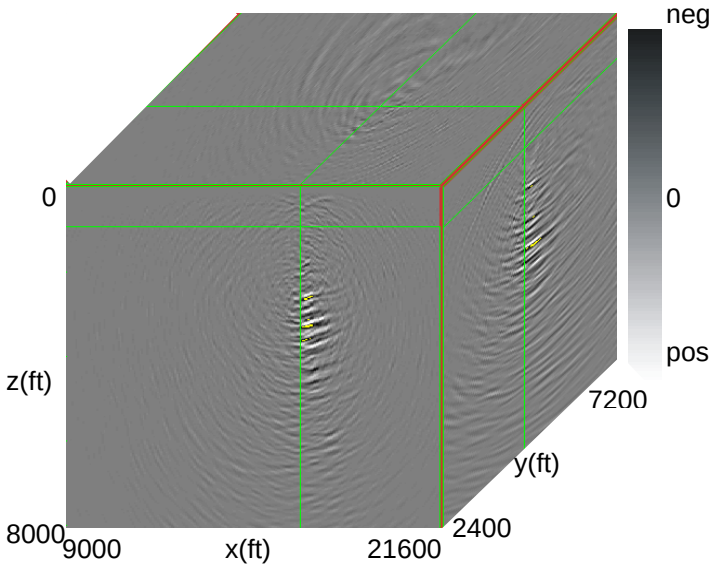

(b)

FIG. 2.5.36. (a) 3-D PP elastic depth image; (b) 3-D PS elastic depth image obtained by migrating 600 shots. Green lines represent the inline, crossline and depth slices intersecting at the receiver no. 1 location. No semblance weighting applied.

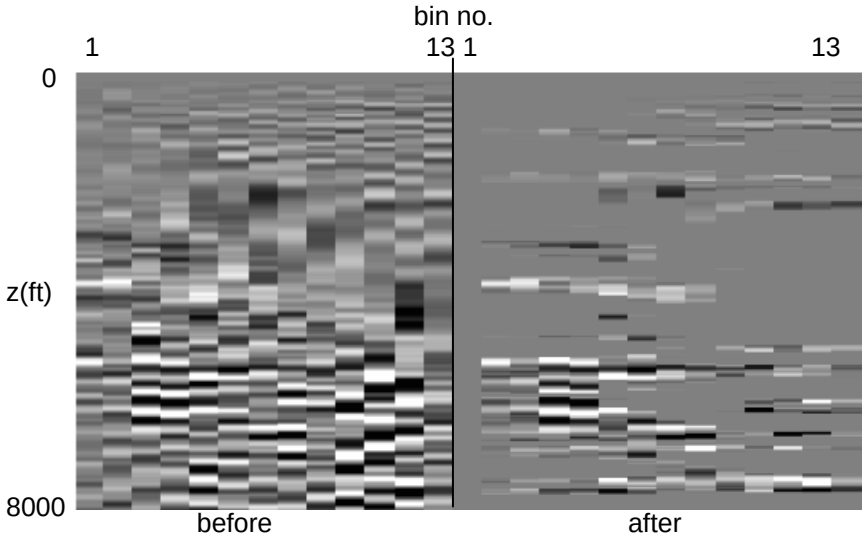

(a)

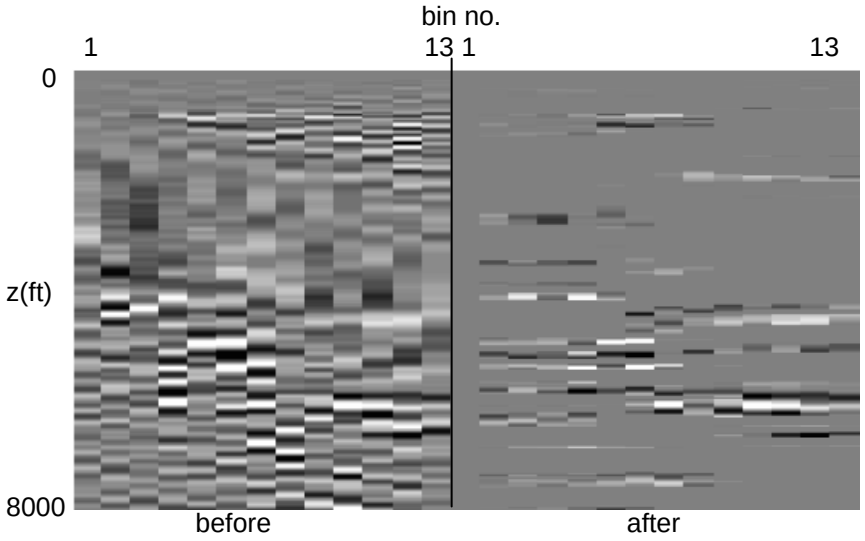

(b)

FIG. 2.5.37. (a) PP common-image gathers; (b) PS common-image gathers before and after applying semblance weighting stacking. 600 shots migrated. Note how most of the incoherent events are removed.

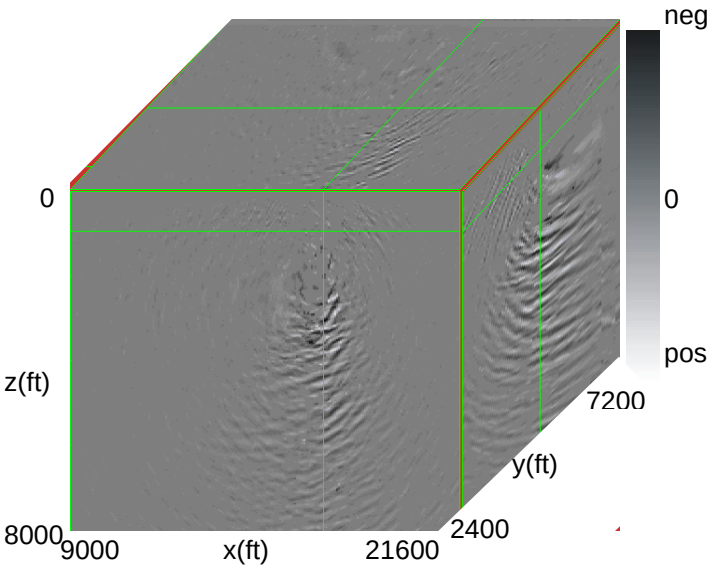

(a)

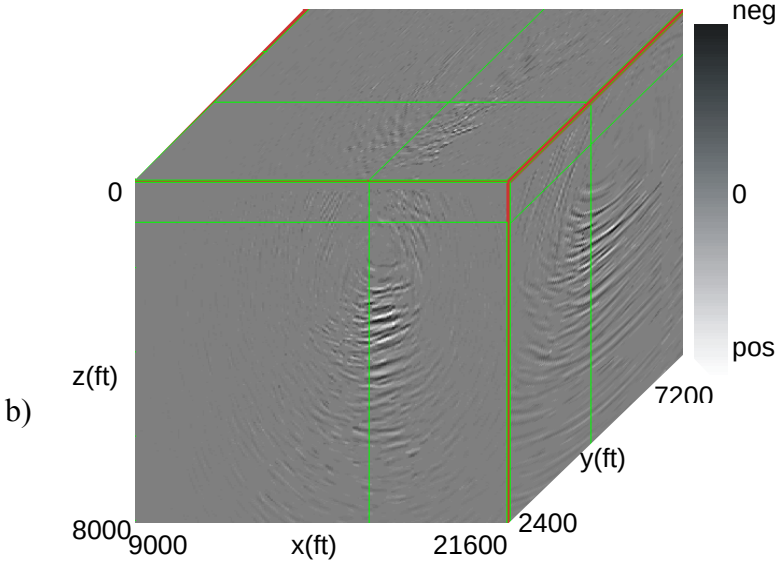

b)

(b)

FIG. 2.5.38. (a) 3-D PP elastic depth image; (b) 3-D PS elastic depth image obtained by migrating 600 shots. Green lines represent the inline, crossline and depth slices intersecting at the receiver no. 1 location. Semblance weighting applied.

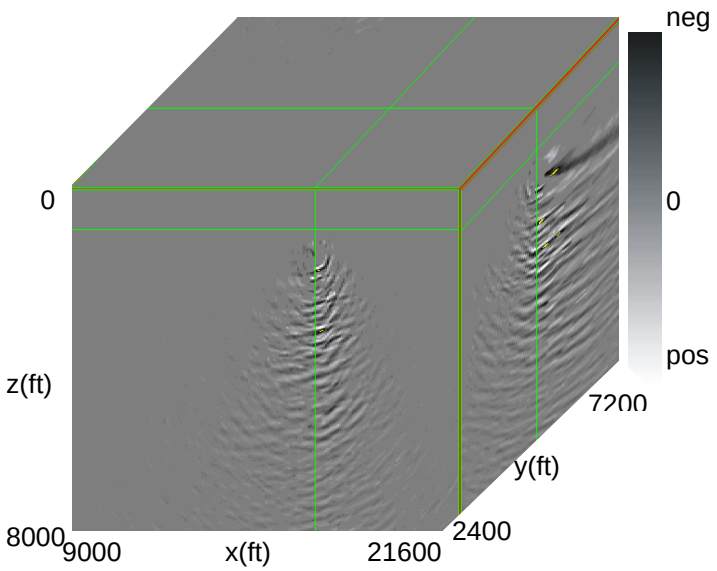

(a)

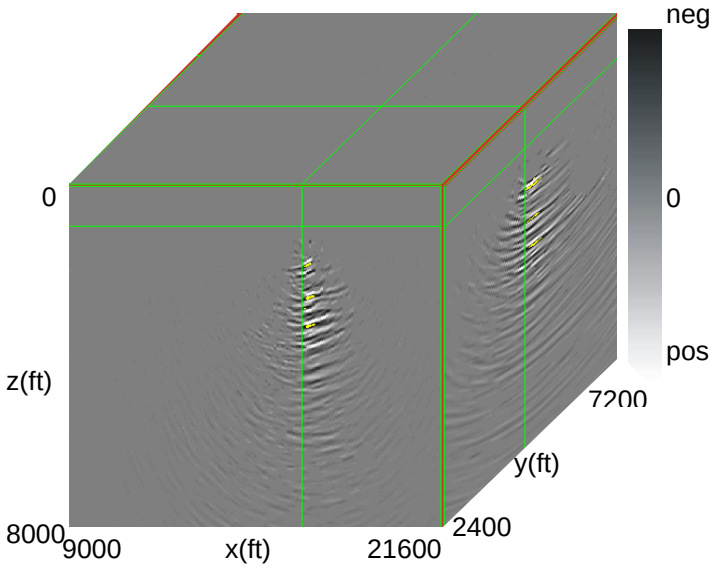

(b)

FIG. 2.5.39. (a) 3-D PP elastic depth image; (b) 3-D PS elastic depth image obtained by migrating 600 shots, up-going events only. Green lines represent the inline,

crossline and depth slices intersecting at the receiver no. 1 location. Semblance weighting applied.

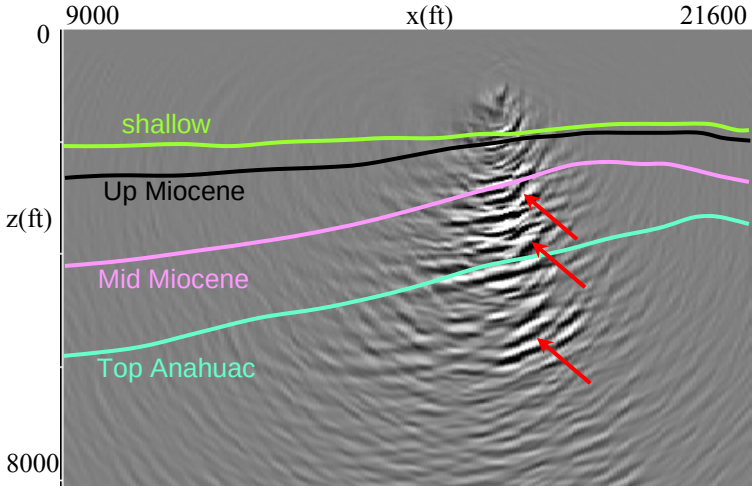

(a)

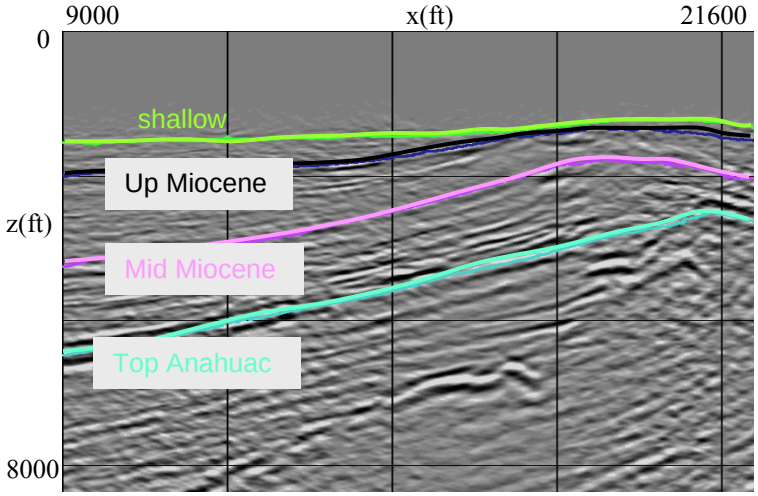

(b)

FIG. 2.5.40. a) 2-D section through the 3-D VSP PP elastic depth image located at the VSP well location; b) 2-D section through the 3-D surface PP acoustic depth image located at the VSP well location. VSP depth image obtained when migrating 600 shots, up-going events only. Both sections show the interpreted sedimentary boundaries that match perfect on both, VSP and surface images. Red arrows mark the probable image of the "Christmas-tree" shape of the salt flank. Note the higher frequency and better continuity of the reflectors in the VSP image compared to the surface image.

2.6 Processing of Surface 3-D Seismic Data

Early in the project we realized that since the VSP imaging will best be done using a depth migration algorithm, that we needed to broaden our objectives to include prestack depth migration of the surface data as well. The innovative Vinton Dome acquisition program included a radial receiver grid on the surface, two multilevel downhole 3-C arrays, and concentric source lines, as shown previously in Figure 2.1.1. This survey was designed to accomplish maximum fold and generate a survey aperture that would focus on the salt structure (Gibson and Tzimeas, 2002). As stated earlier, seismic sources were 5.5 pound pentolite charges detonated at a depth of 60 feet (18m). The survey consisted of seventy-two receiver lines, with half of the lines extending from the predicted perimeter of the salt dome to the distal edges of the survey, and the other half extending from about half the length of the long lines to the distal edge of the survey. Each line was separated by five degrees, with the long line and short lines separated by ten degrees. Receiver stations consisted of a six-element array of 10-Hz geophones and were spaced 165 feet (50m) along each line segment. Source locations approximated concentric circles with a shot spacing of 165 feet (50m) along the arc. Most disruptions in the shot pattern were due to cultural obstacles located in the north and west portions of the survey (Constance et al., 1999).

Each shot had a 90º coverage with 19 active receiver lines per shot, and between 1400 and 2000 active channels. For each active 90º receiver sector the center rack of source locations formed an arc through the receiver lines. Because the entire receiver line was

active, there was no radial roll. After each shot the active receiver spread advanced two receiver lines (10º). In addition to enhancing illumination of steeply dipping beds, this acquisition design kept raypaths from passing through the salt in an attempt to avert the need for depth imaging (Constance et al., 1999).

The surface seismic data were prestack time migrated (PSTM), and prestack depth migrated (PSDM) by Duncan (2005) as a major part of his dissertation research. Our objective was to find an effective pre-migration processing flow that was easily implemented and reduced noise without drastically affecting the data, especially the bandwidth of the data.

Coherence of brute stacks and uniform moveout on super shot gathers provided a QC for geometry and field statics. Duncan (2005) applied common mid-point (CMP) sorted shot data with datum static shift and spherical divergence, and ran these data through deconvolution. He tested several band pass filters to determine the best one to remove the ground roll, and then used the data that maintained the broadest bandwidth, the 16-17-70-80 filter to calculate the residual static. This required using a detailed velocity field. In order to maintain continuity with the commercially processed PSTM data, he used the velocities from the PSTM for calculating the residual static. Duncan then developed a second processing flow to improve the signal-to-noise ratio for migration. The new processing flow consists of applying both the field static and the residual static to the CMP sorted data and boosting the gain using spherical divergence. At this stage, Duncan (2005) applied a surface consistent deconvolution and filter resulting in a different

deconvolution operator for each the source and receiver location. After each processing step, he applied NMO, along with a mute, using the same velocity used to calculate the residual static. At this stage, brute stacks of the data showed attenuation, especially in the eastern half of the survey.

Table 2.6.1.

Flow chart of initial processing to calculate residual static

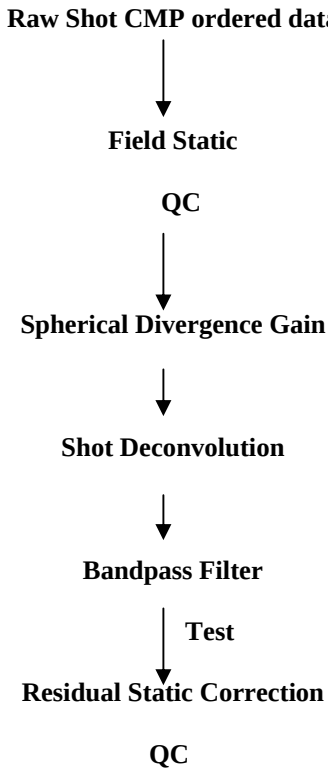

Duncan (2005) balanced the amplitudes with long window automatic gain control (AGC), applied after the data were filtered. He also applied long window AGC before migration. By balancing the amplitudes, the stack eliminated the higher amplitude low frequency noise caused by ground roll before the second application of AGC. Improvement of the signal justified opening the filter to 5-6-70-80, increasing the bandwidth and further improving fidelity. High amplitude first breaks created artifacts that Duncan (2005) muted before application of the filter. This processing flow (Table 2.6.1) reduced migration smiles. Remaining "smiles" may be the result of lack of detail in the sedimentary velocity model at the salt/sediment interface. A comparison of data processed with the minimal parameters and those with the more aggressive approach

show differences in both the vertical sections (Figure 2.6.1) and in the depth slices (Figure 2.6.2). Insights from these comparisons were used to select the processing flow

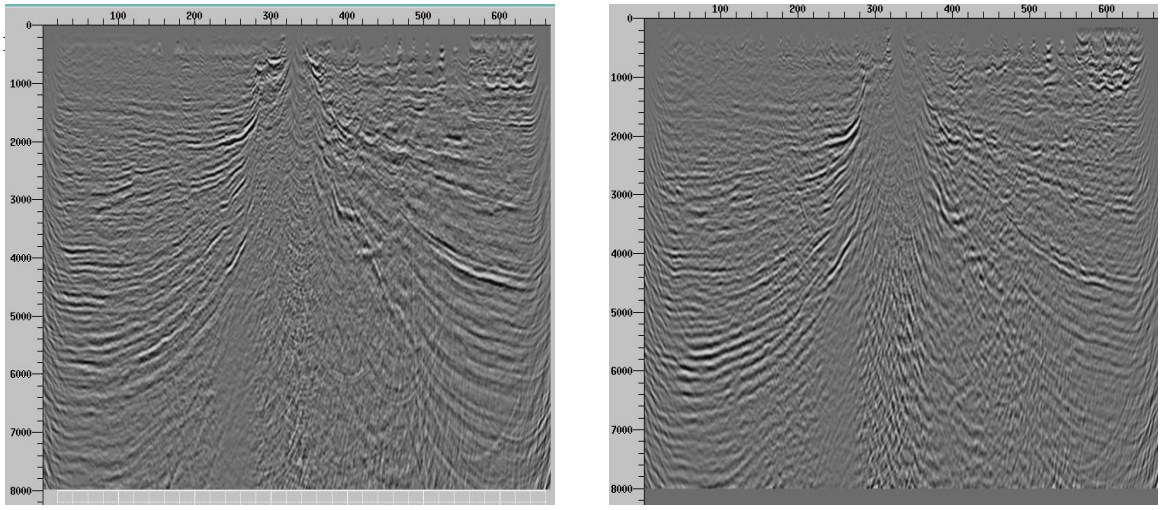

(a) **(b)**

Figure 2.6.1. Sections comparing the processing flows with (a) minimal processing Table 2.6.1 and (b) more aggressive processing shown in Table 2.6.2.

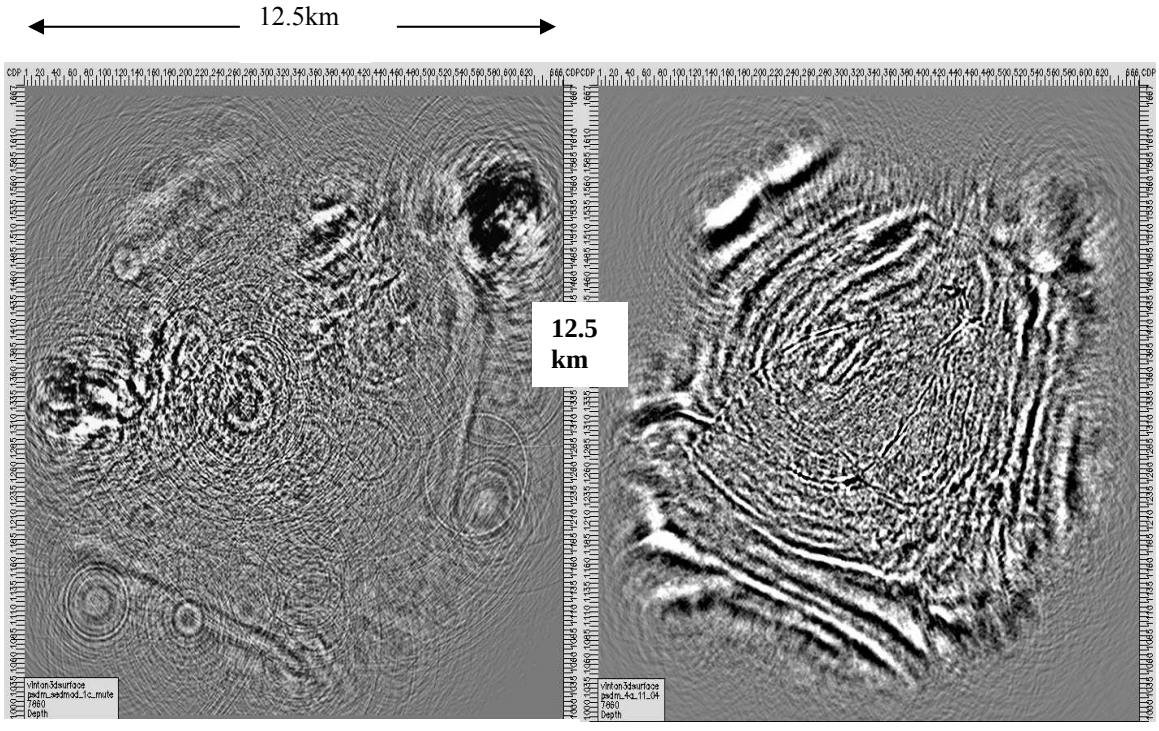

(a) **(b**

Figure 2.6.2. Depth slices used for comparing processing flows with (a) minimal processing and with (b) the more aggressive processing described in Table 2.6.2.

Table 2.6.2

Final processing flow

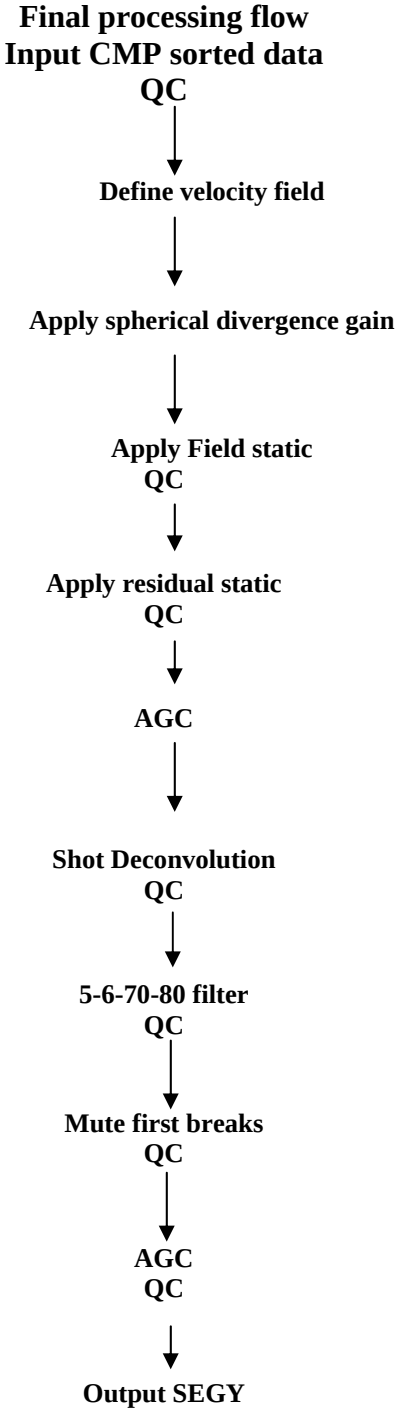

2.7 Velocity Modeling and PreStack Depth Migration (PSDM)

Pre-stack depth migration (PSDM) and associated velocity models have been widely used for large, 3-D seismic marine surveys. Many of the problems in marine seismic data using PSDM exist in 3-D land surveys, but differences between 3-D marine data and 3-D land data warrant a reevaluation of methodology used to generate land data velocity models.

Fidelity problems resolved by PSDM in marine seismic data are present in the pre-stack time migrated (PSTM) data in the 3-D Vinton Dome seismic survey. These issues include misplaced salt, poor well ties, and the inability to image small fault blocks. Two reasons for this lack of fidelity include strong lateral velocity variations caused by salt, along with effects of salt movement on sediment and seismic anisotropy, primarily associated with shale bodies. Given an accurate interval velocity model, PSDM can generate high fidelity subsurface images in the presence of lateral velocity variations (Liu et al., 2001; Schultz, 1999), such as those that occur at Vinton Dome. In this situation, estimation of an accurate interval velocity model is key to improving the fidelity of the subsurface image (Guo and Fagin, 2002a, 2002b). Duncan (2005) built a well-based, sediment velocity model ("well based model") using sonic logs, and compared it to an initial sediment model based on seismic migration velocities ("prestack time migrated velocity model"). The well-based model helps to compensate for the fact that seismic land data tend to be noisy as a result of variable receiver coupling, cultural noise, and static problems. Much of this noise is coherent and difficult to eliminate. An additional advantage in using sonic logs to build the initial velocity model is that it results in

minimal manipulation of the velocity data. Sonic logs record velocities as depth interval velocities, and we used these depth interval velocities directly for the PSDM velocity model. In contrast, seismic velocities are RMS time velocities, and it is a two-step process to convert RMS time velocities to interval velocities in depth.

Velocity Model Building

There are two basic approaches in velocity model building, a grid-based approach and a layer-based approach (Guo and Fagin, 2002a, 2002b). The grid-based approach uses seismic data to model the velocity field and velocity modeling using geologic information such as geologic horizons and structures characterizes the layer-based approach. Layer-based velocity modeling uses seismic data and requires *a prior* knowledge of the subsurface. In situations were there is little geologic information, a grid approach is the only applicable tool.

Grid-based velocity modeling begins by converting RMS velocities to time interval velocities. Converting RMS velocities to time interval velocities requires an x, y location, often referred to as a velocity location. The velocity location is typically associated with a reference horizon that serves to identify the interval. Reference horizons include the water bottom in a marine survey or seismic horizons that are spaced evenly at increasing intervals with depth. Interpreted seismic horizons are commonly used for determination of the time interval velocity. Once the time interval velocity has been determined, application of the Dix formula (Dix, 1955) converts it to a depth interval velocity for use in migration.

The layer-based approach involves identifying the shallowest layer, usually from an interval between two geologic horizons. Conversion of the seismic RMS velocities to depth interval velocities in the layer-based approach is restricted to one layer at a time. Restricting the velocity model to a single layer allows modeling of detailed velocities by incorporating *a priori* geologic knowledge, often from well logs, into the model. Increased detail in the shallow layers helps minimize the impact of spurious data that will propagate through the seismic volume. This procedure is repeated for successive layers until completion of the velocity model to the targeted depth and the application of a full PSDM to the entire survey (Guo and Fagin, 2002a, 2002b).

Velocity Modeling of Vinton Dome

Our goal was to design a detailed velocity model that was as efficient to build as a grid-based model. Typically, in areas containing salt such as the upper Gulf of Mexico Basin, the focus of the velocity modeling is to image the shape of the salt. The first step in this iterative process begins with an initial sediment velocity model. With this model, data are PSDM and used to update the velocity model by picking a top of salt horizon. Salt velocities are flooded beneath the salt and the data are re-migrated. Using the new PSDM volume allows for focusing details in the salt by iteratively updating and detailing the velocity model. The iterative nature of this process requires that the initial sediment velocity model be as accurate as possible. Duncan (2005) used sonic logs to build the initial sediment velocity model instead of seismically derived velocities. Issues of velocity differences between well logs and seismic velocities typically preclude their exclusive use to build an initial velocity model. In this survey he used eighteen sonic

logs from vertical wells close to the salt flank to build an initial sediment velocity model, and generated a 1-D, V_z velocity gradient from the sonic logs biasing the farthest log from the salt to derive the gradient. He weighted this log assuming the velocities from it reflected the regional velocity trend.

To fill gaps created by the throw of faults and to bridge the gap created by the salt Duncan (2005) picked, interpolated, and smoothed seven horizons on the PSTM data. Smoothing the horizons allowed the creation of a reference with a basis in geology and depth, and maintained the relative position and spacing of each horizon. The horizons were then converted to depth using the V_z velocity gradient. Using points of known depth from the sonic logs, Duncan (2005) flexed the horizons to match the sonic logs, keeping the relative spacing between horizons, and applied the sonic log velocities at the point of intersection between each horizon and log. He then calculated a sloped interval velocity between horizons by using the velocity at the intersection from the top horizon to the next lower horizon. The velocity cube was then built by extrapolating velocities from the wells. The variations in layer thickness resulted in a nonlinear extrapolation.
The initial QC of the model by comparison with known structures helped validate the model. Smoothing and extrapolation initially removed all structure from the horizons used to build the model, yet the faults could be observed in the velocity cube (Figure 2.7.1).. A comparison of the velocity model and the PSTM seismic volume confirmed that the structures were real. Even with sparse sampling of well logs, this technique was sensitive enough to include structure into the initial sediment velocity model, and provided a QC of the model.

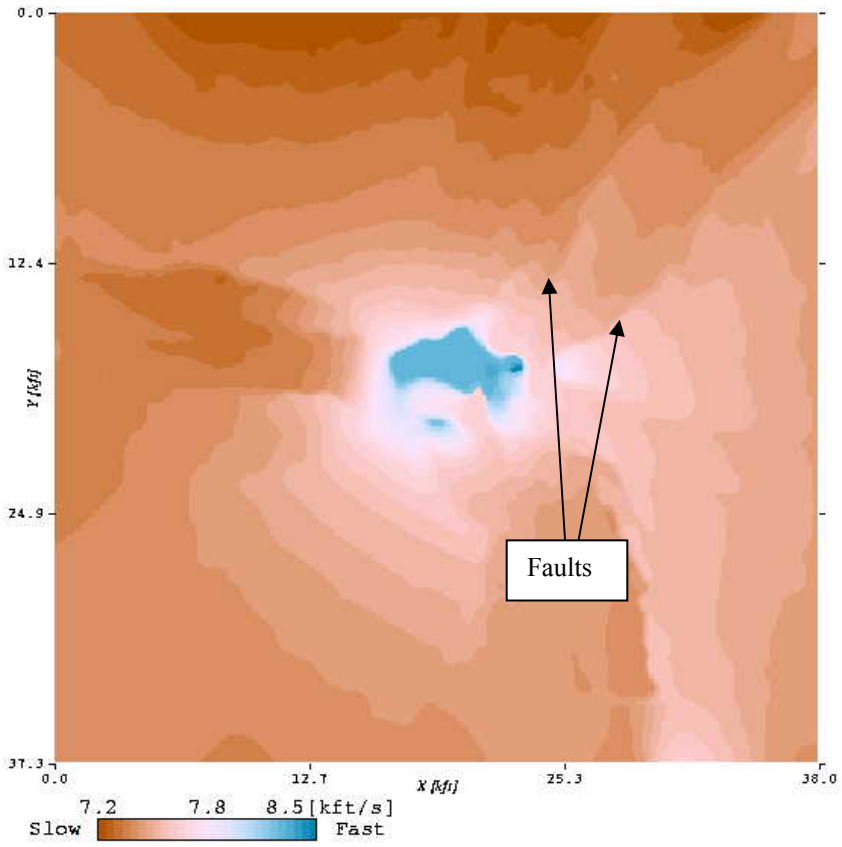

Figure 2.7.1. Depth slice from the velocity model showing that details including faults appear in the sediment velocity model (From Duncan, 2005).

Duncan (2005) tested differences between the seismically derived velocity models and his well-log velocity derived models by building a prestack time migrated velocity model and applying PSDM. Stacking velocities were converted to depth interval velocities with the same horizons used to create the well log velocity model. Building the prestack time migrated velocity model followed an industry standard workflow using commercial software. Surface seismic data were PSDM with the prestack time migrated velocity model, smoothed and compared to the PSDM volume generated with the velocity model derived from well logs.

PSDM Migration

Duncan (2005) used a Kirchhoff PSDM to migrate the surface seismic data with commercial software; processing parameters were determined from vendor supplied software for acquisition analysis. He determined the migration aperture parameters from the acquisition, and generated histograms showing offset in the inline direction and crossline direction for determination of parameters for migration. Output parameters were also based on acquisition, a 0 - 180° radius was set because of the radial acquisition.

PSDM Migration Results

A comparison of the results from the initial sediment model migration with the PSTM seismic volume indicated improved resolution in the PSDM especially in imaging the salt flanks (Figure 2.7.2). One of the benchmarks used to assess the value of this method was the ability to image small compartmentalized reservoirs. In the PSTM volume, small fault compartments interpreted from log data were not imaged, but in the initial PSDM volume, faults are sharper and smaller faults are more visible. Figure 2.7.3 shows a portion of the survey where small, compartmentalized fault blocks were identified from well logs but are not imaged in the PSTM. In contrast, using the well-based PSDM volume, Duncan interpreted a number of subtle fault blocks (Figure 2.7.4) in the same portion of the survey, validated by coincidence with missing sections in the Anahuac section on well logs.

In addition to better definition of small fault blocks, the prestack time migrated velocity model PSDM data places events about 200 feet shallower, indicating a slower prestack time migrated velocity model, or a faster well-based model. Fault planes are more

coherent in the well-based data, indicating they are more correctly placed in x, y, and z space. Faults and the salt body are more coherent in depth slices from the well-based PSDM volume than from the prestack time migrated velocity model PSDM volume. Examination of dip lines through the fault blocks indicate that although the well-based PSDM is higher frequency and images the faults and salt flanks better, the PSTM images the shallower faults almost as well. This further demonstrates the most powerful advantage of the PSDM is in areas of strong lateral velocity changes.

Finally, a comparison of synthetic seismic derived from well logs to the two types of PSDM data showed that in most cases, the well-based PSDM most closely matched the synthetics.

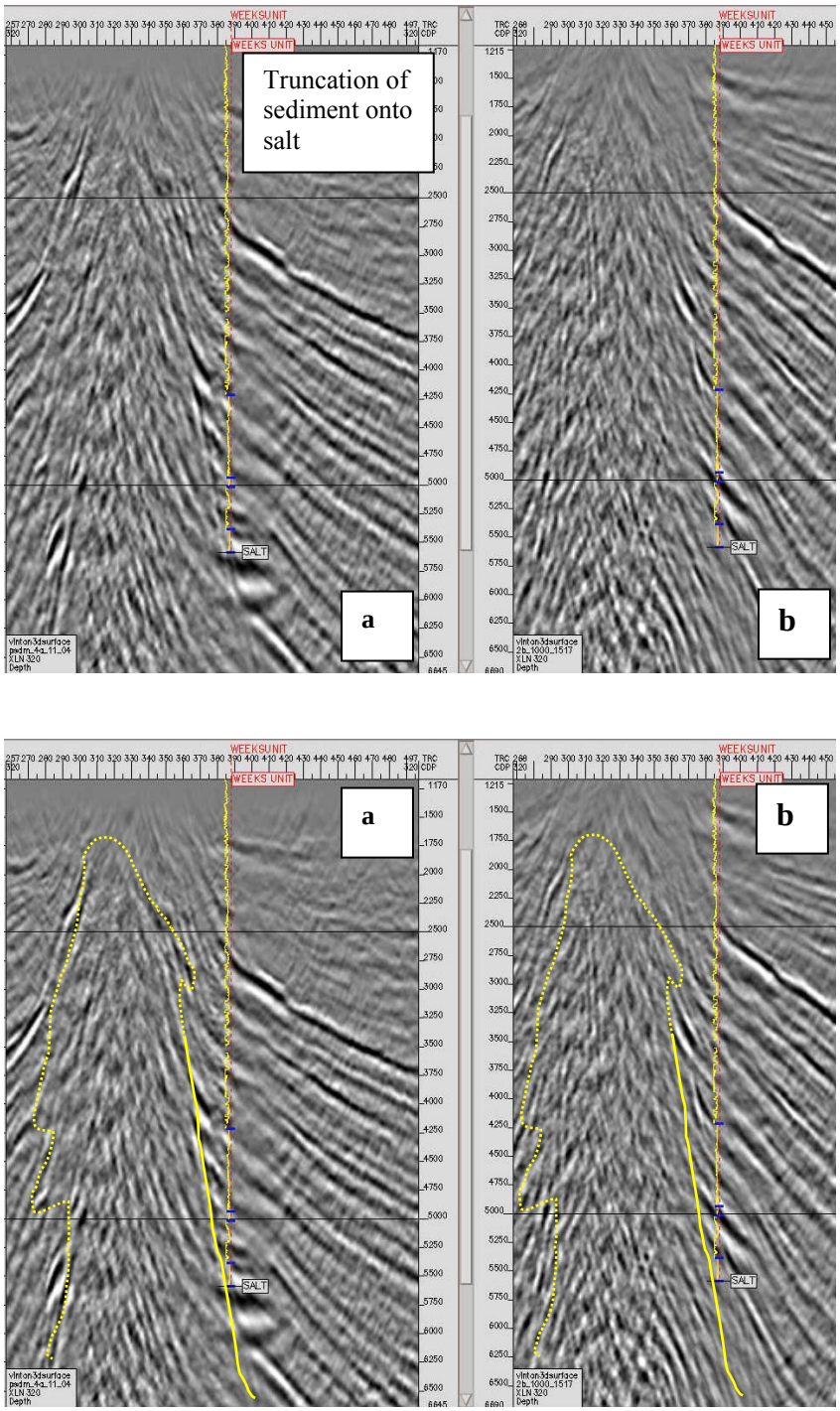

Figure 2.7.2. Seismic section (xline 320) from (a) the well-based velocity model PSDM, and from (b) the prestack time migrated model PSDM used to compare the resolution of salt flank. Interpretation based on well tie and truncation of sediments (from Duncan, 2005).

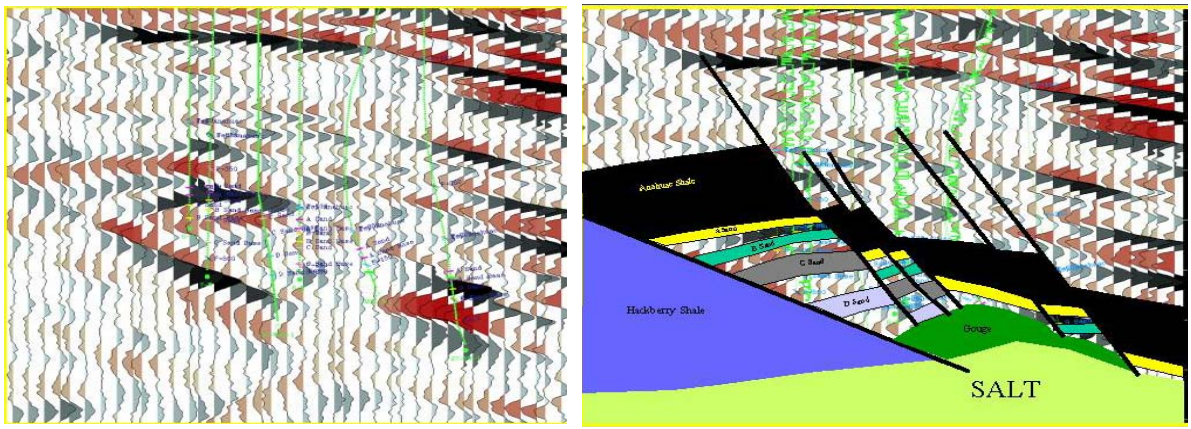

(a) **(b)**

Figure 2.7.3. PSTM section in area with compartmentalized faults (a) uninterpreted and (b) well log interpretation of structure, suggesting very poor fidelity of fault imaging by PSTM (from Duncan, 2005).

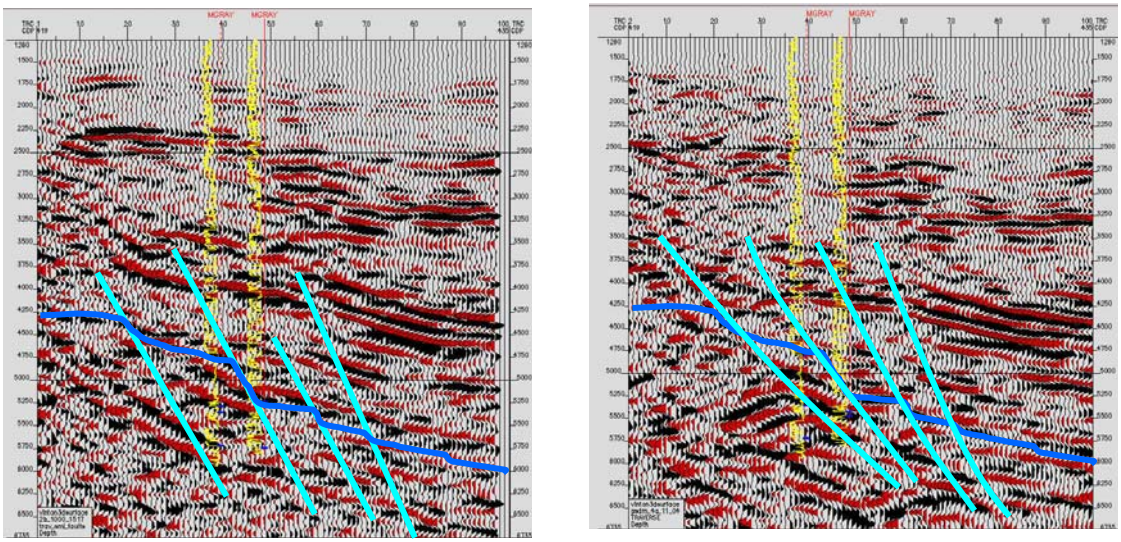

(a) **(b)**

Figure 2.7.4. Interpreted fault blocks in (a) the migrated velocity model PSDM and (b) the well-based velocity model PSDM. Blue horizon is top Anahuac (from Duncan, 2005).

2.8 3-D multi-trace, geometric seismic attributes

While seismic attributes such as acoustic impedance and spectral decomposition are directly related to porosity and reservoir thickness, geometric attributes are only indirectly related to these reservoir properties. By use of geologic models and paleo and modern geologic analogues, geometric attributes provide a means of unraveling the history of depositional environment and tectonic deformation, thereby allowing us to infer petrophysical properties such as sand/shale ratios, diagenetic alteration, and the likelihood of fractures.

Structure-oriented filtering

Most seismic volumes, and land data in particular, are plagued by overprinted noise. In the case of Vinton Dome, this noise is due primarily to backscattered surface waves, but also to traffic and pump jack noise. Missing shots and receivers in the migration aperture also contribute to artifacts in the image. Driven by data quality issues in the Vinton Dome surface data, we perfected a new structure-oriented filter that replaces the original seismic data with its principal component, or most coherent part. By using multiple overlapping windows (described by Marfurt, 2005), this filter avoids smearing across faults or other discontinuities. In Figure 2.8.1 we display time slices through coherence volumes at t=1.0 and t=1.5 s generated from seismic before and after structure-oriented filtering. The impact of this filtering is a cleaner image of the faults and other discrete discontinuities. However, while structure-oriented filtering will sharpen edges seen by coherence, it will not move reflectors that have been improperly migrated. We see this effect in Figure

2.8.2. While the fault plane terminations are sharper, the fault planes do not properly align, giving rise to the staggered fault plane segments seen in Figure 2.8.3.

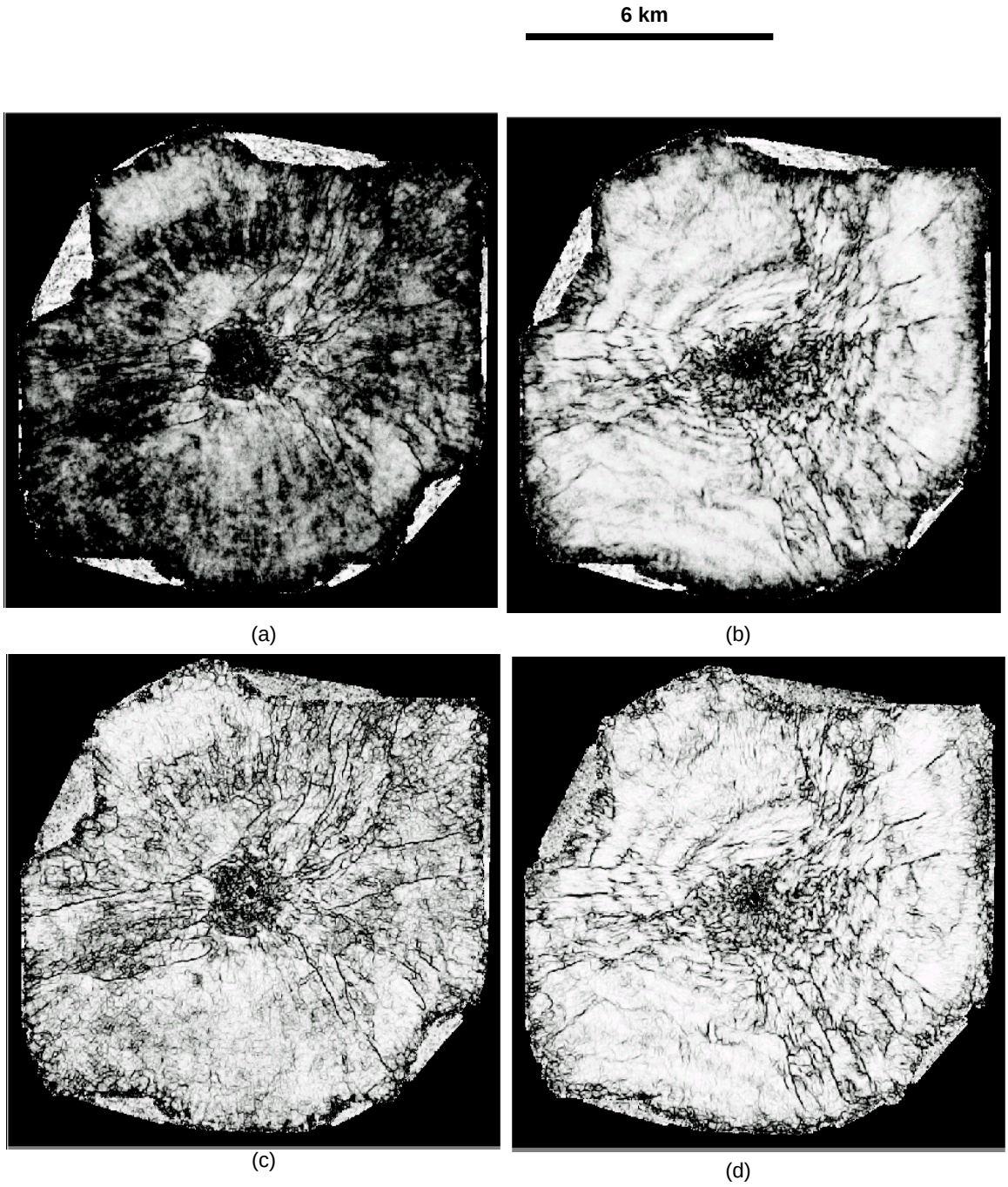

Figure 2.8.1. Time slices through coherence volumes generated for the Vinton Dome survey at 1.0 s (a) before and (b) after structure-oriented principal component filtering, and at 1.5 s (c) before and (d) after structure-oriented principal component filtering. (From Marfurt, 2005).

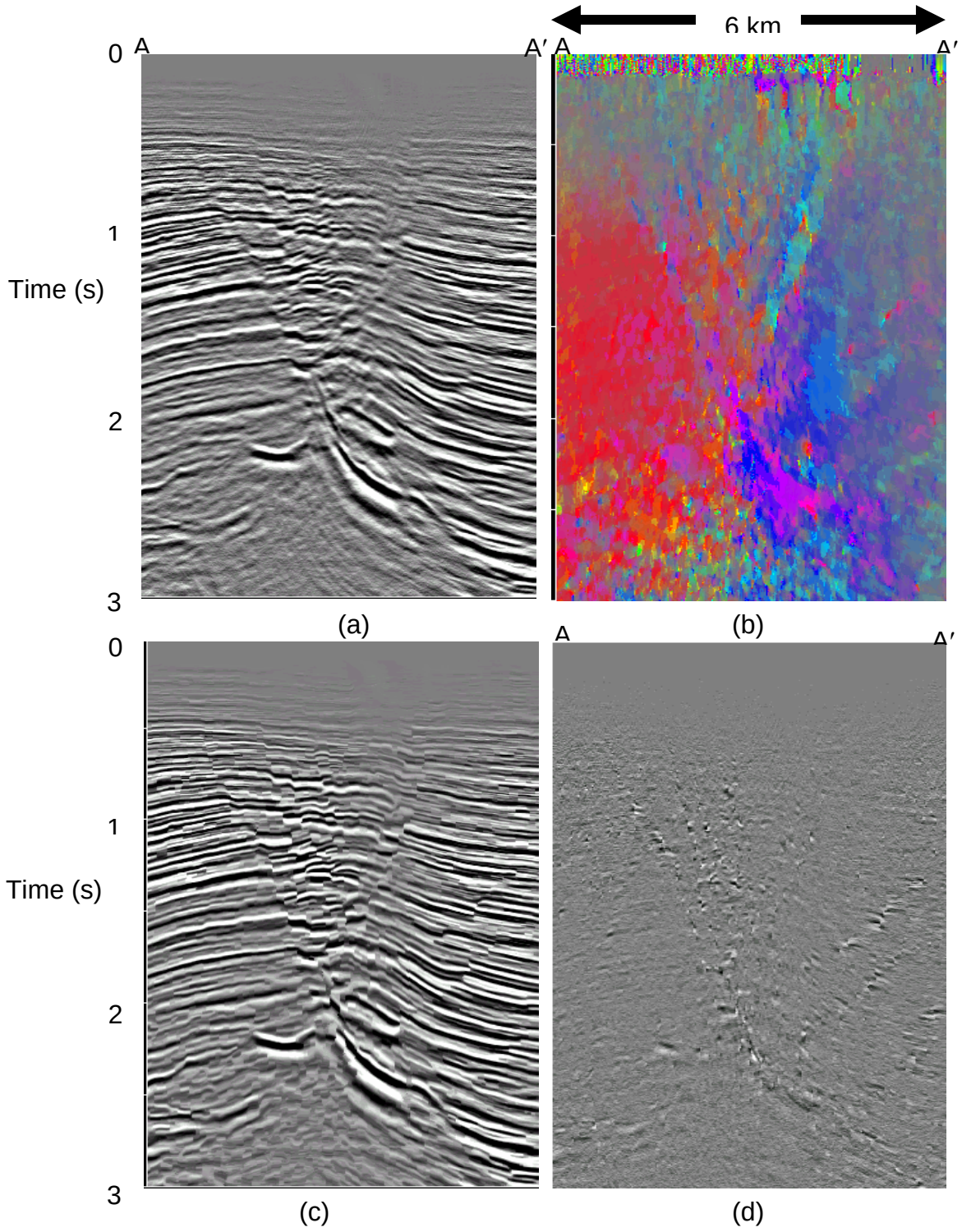

Figure 2.8.2. Vertical slice through (a) seismic amplitude and (b) dip/azimuth volumes at Vinton Dome before principle component structure-oriented filtering. (c) Filtered data and (d) rejected noise. Note how the fault terminations are sharper, but that that the fault planes are still misaligned. This misalignment is due to an inaccurate migration and cannot be repaired by structure-oriented filtering. (After al-Dossary et al., 2002).

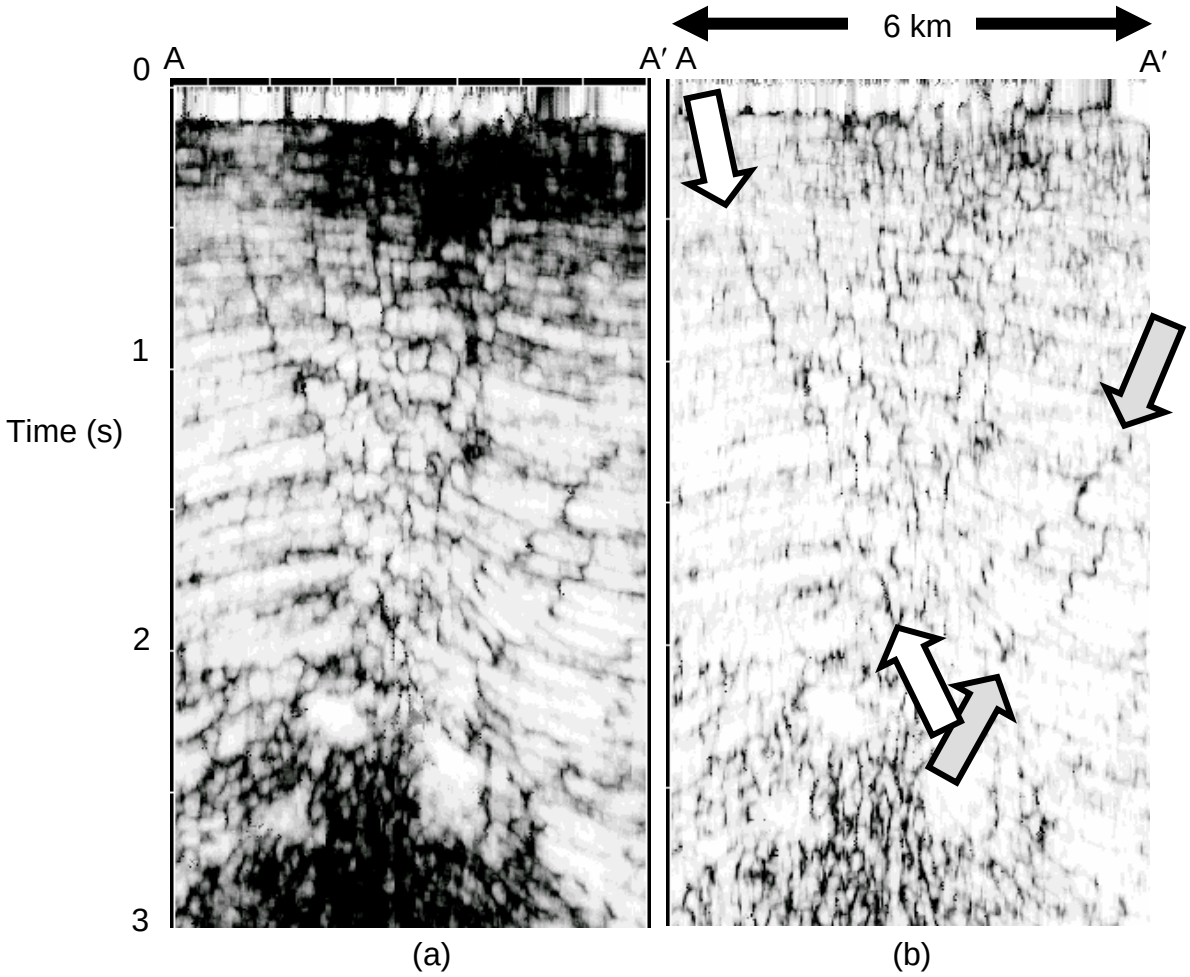

Figure 2.8.3. Vertical slice through the coherence volume (a) before and (b) after structure-oriented filtering. Note that the fault plane indicated by the gray arrow is poorly aligned. This misalignment is due to an inaccurate migration velocity model. (After al-Dossary et al., 2002).

Multiattribute display

One challenge with multiple attributes is how to convey the information they contain. We address this issue by designing 2-D and 3-D colorbars. These 2-D and 3-D colorabars are then to the 1-D color bars used by conventional seismic display algorithms. In Figure 2.8.4a we display a time slice at t=1.0s through dip magnitude and dip azimuth volumes. We map dip magnitude against saturation and dip azimuth against hue. In this manner, reflectors dipping steeply to the north appear as a pure blue color, reflectors dipping to the south appear as pure yellow, and so forth. Flat-lying reflectors have no well-defined azimuth and appear with no color saturation, or gray. In Figure 2.8.4b we display a time slice through the coherence volume plotted against a conventional single gradational 1-D gray scale color bar. In Figure 2.8.4c we display the contents of Figures 2.8.4a and b using a 3-D color bar. In this image, dip magnitude and dip azimuth are plotted as in Figure 2.8.4a, but coherence is plotted against lightness. In this manner we are able to observe rotation of reflectors about the salt dome and about faults on time slices.

In Figures 2.8.5a and b we display a vertical slice through the coherence and seismic amplitude volumes respectively. In Figure 2.8.5c we display the two attributes together using a 2-D colorbar, where coherence modulates the lightness, and seismic amplitude modulates a conventional dual gradational red-white-blue 1-D colorbar.

In Figure 2.8.6a we display the same seismic line as shown in Figure 2.8.5b, but now plotted against a single gradational gray scale. In Figure 2.8.6b, we plot the dip/azimuth using the same color bar used in Figure 2.8.4a. In Figure 2.8.6c we display the seismic

and the dip/azimuth in the same image. This latter image allows an interpreter the ability to visualize how each reflector dips not only within but also in and out of the plane of view.

Coherence vs. coherent energy gradients

While coherence is an excellent indicator of faults and thick channels, it does not show channels that fall below the ¼ wavelength of thin bed tuning. In this situation, the waveform does not change and only the amplitude varies laterally. In Figure 2.8.7 we display a vertical slice through the seismic amplitude volume with both mid Miocene and Hackberry picks. In Figure 2.8.8 we display horizon slices along these two horizons through the coherence volume. The faults are clearly seen at the mid Miocene level but are more diffuse at the Hackberry level. The major reason for this loss in lateral resolution is the inaccurate migration velocity. We note some relatively featureless 'bright' areas at the Hackberry level.

In Figure 2.8.9 we display horizon slices along the same two horizons through the coherent energy gradient (described by Marfurt, 2005). This attribute displays lateral changes through the coherent energy and is therefore quite sensitive to amplitude effects associated with thin bed tuning. We note several channels (arrows) in the zone that appeared to be featureless in the coherence images.

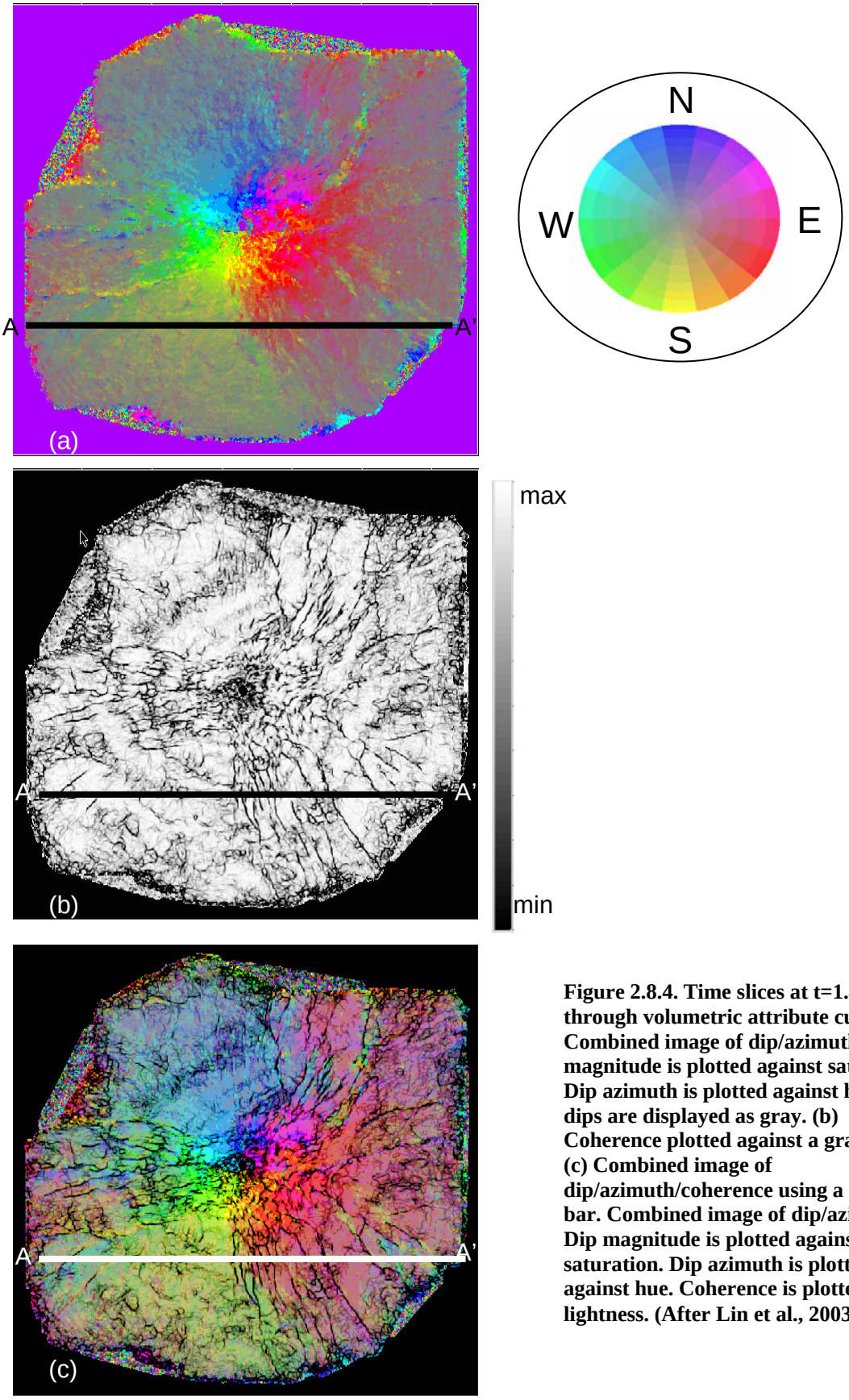

Figure 2.8.4. Time slices at t=1.4 s through volumetric attribute cubes: (a) Combined image of dip/azimuth. Dip magnitude is plotted against saturation. Dip azimuth is plotted against hue. Flat dips are displayed as gray. (b) Coherence plotted against a gray scale. (c) Combined image of dip/azimuth/coherence using a 3-D color bar. Combined image of dip/azimuth. Dip magnitude is plotted against saturation. Dip azimuth is plotted against hue. Coherence is plotted against lightness. (After Lin et al., 2003).

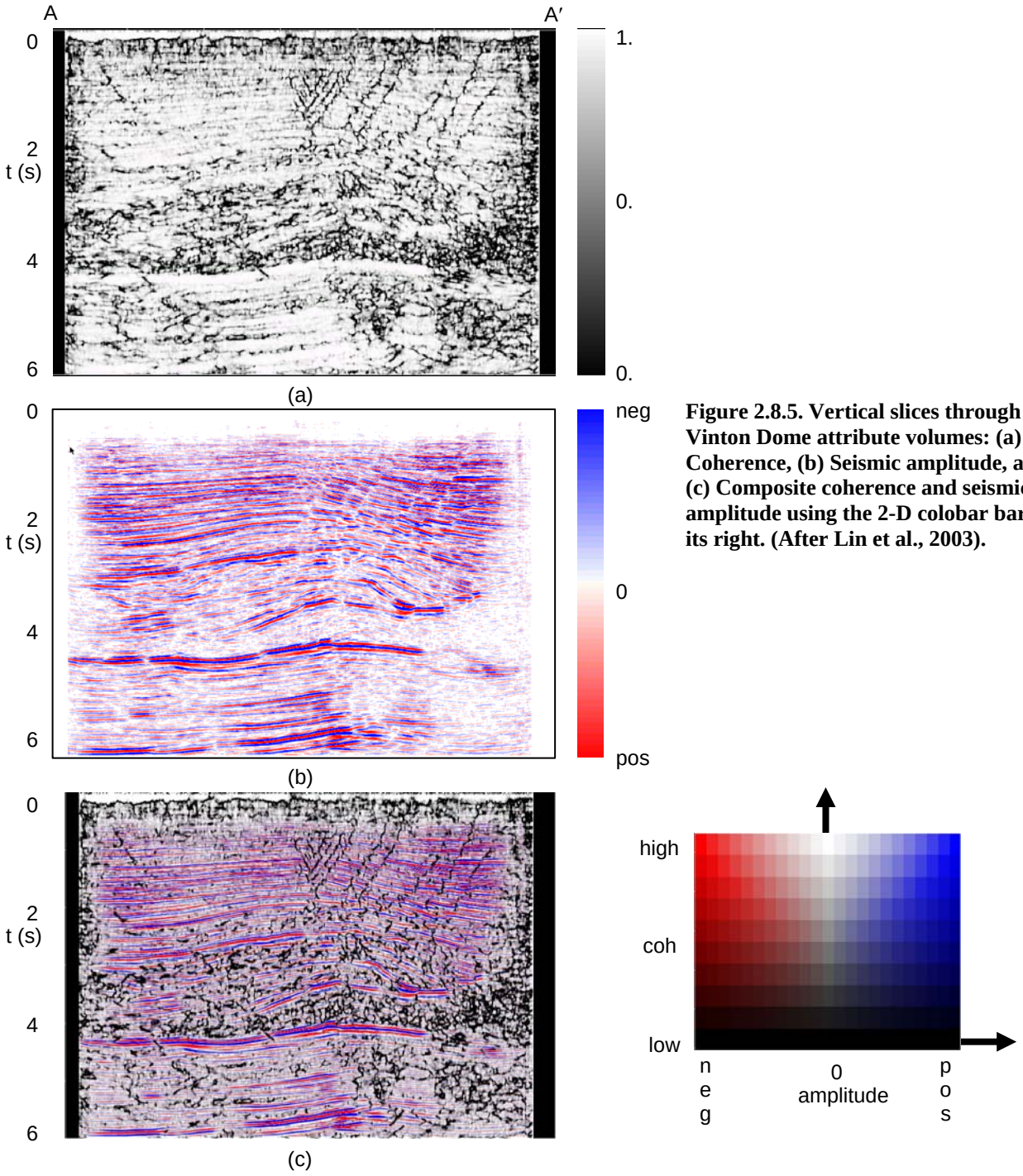

Figure 2.8.5. Vertical slices through Vinton Dome attribute volumes: (a) Coherence, (b) Seismic amplitude, and (c) Composite coherence and seismic amplitude using the 2-D colobar bar to its right. (After Lin et al., 2003).

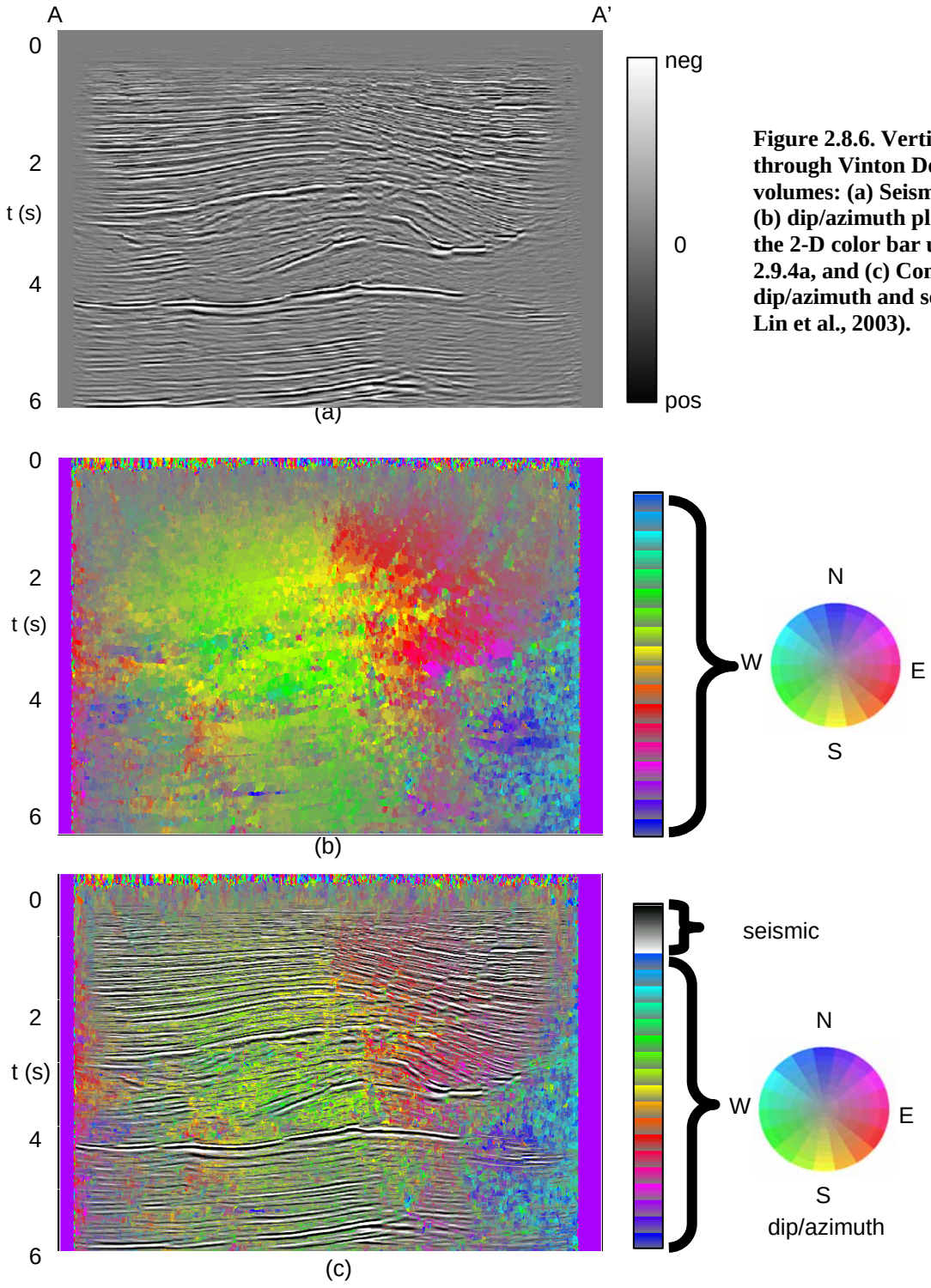

Figure 2.8.6. Vertical slices through Vinton Dome attribute volumes: (a) Seismic amplitude, (b) dip/azimuth plotted against the 2-D color bar used in Figure 2.9.4a, and (c) Composite image of dip/azimuth and seismic. (After Lin et al., 2003).

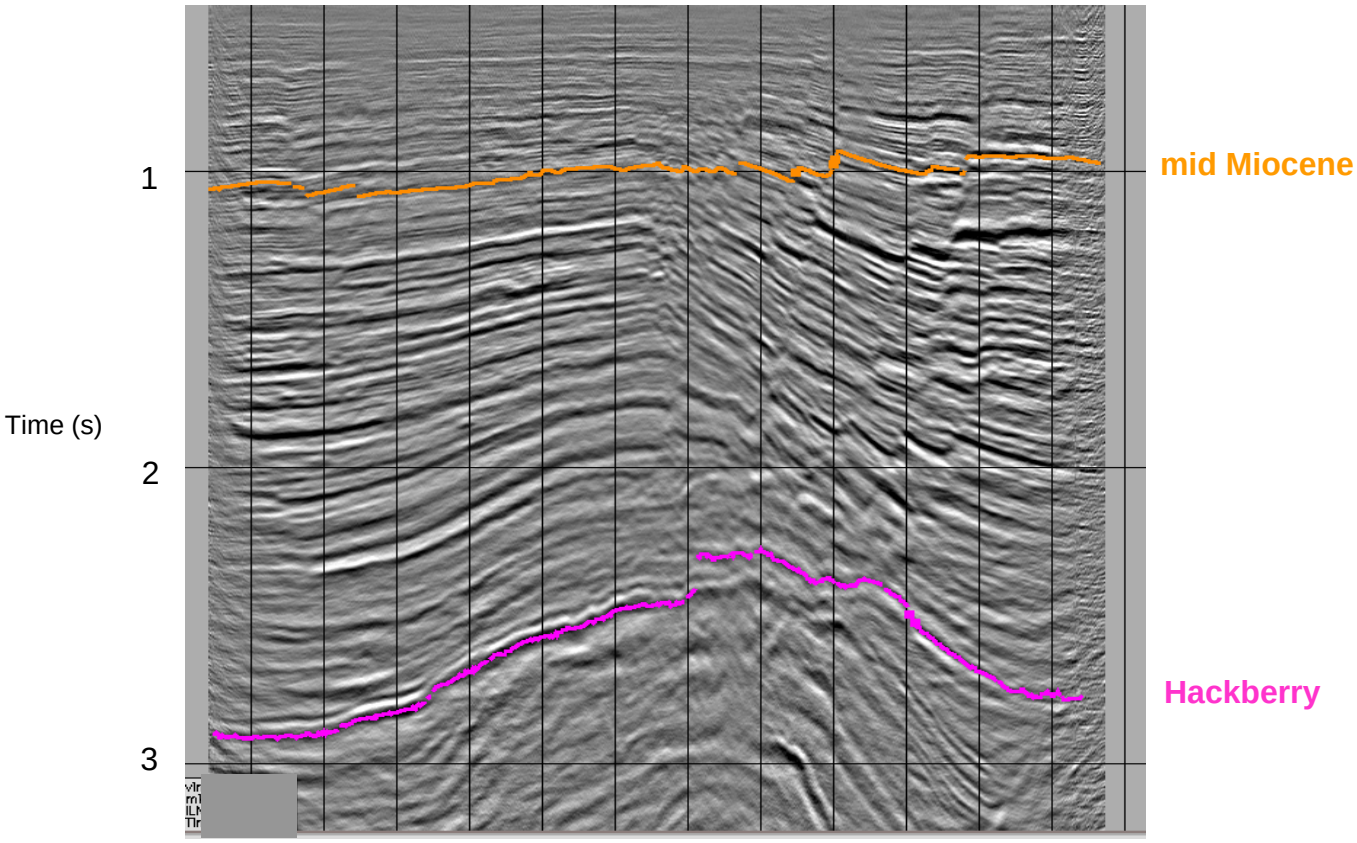

Figure 2.8.7. Vertical line through seismic amplitude volume showing the mid Miocene and Hackberry picks. Note the lower resolution at the Hackberry level.

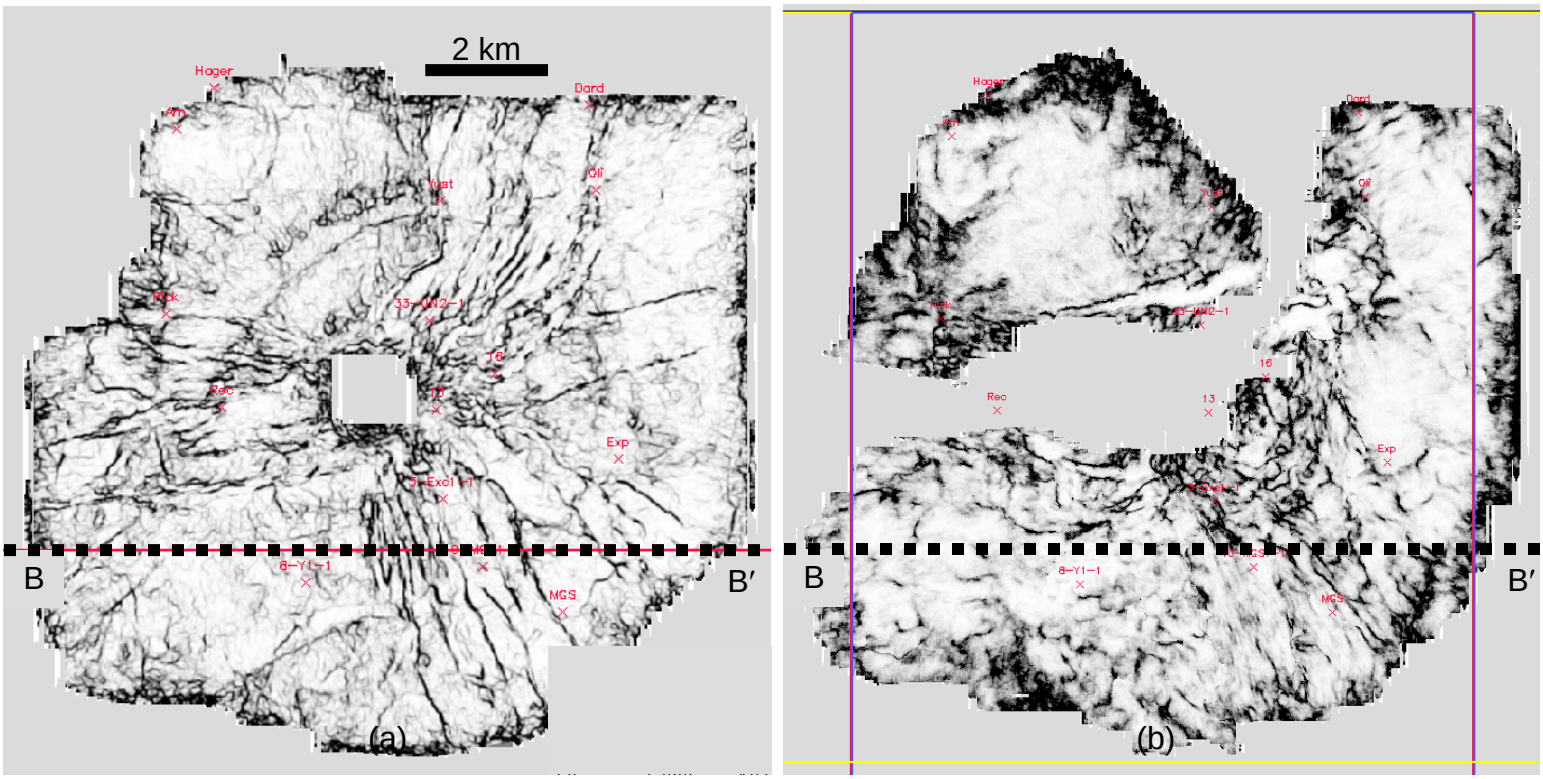

Figure 2.8.8. Horizon slice through the coherence volumes along (a) the Mid Miocene and (b) Hackberry levels shown in Figure 2.8.7.

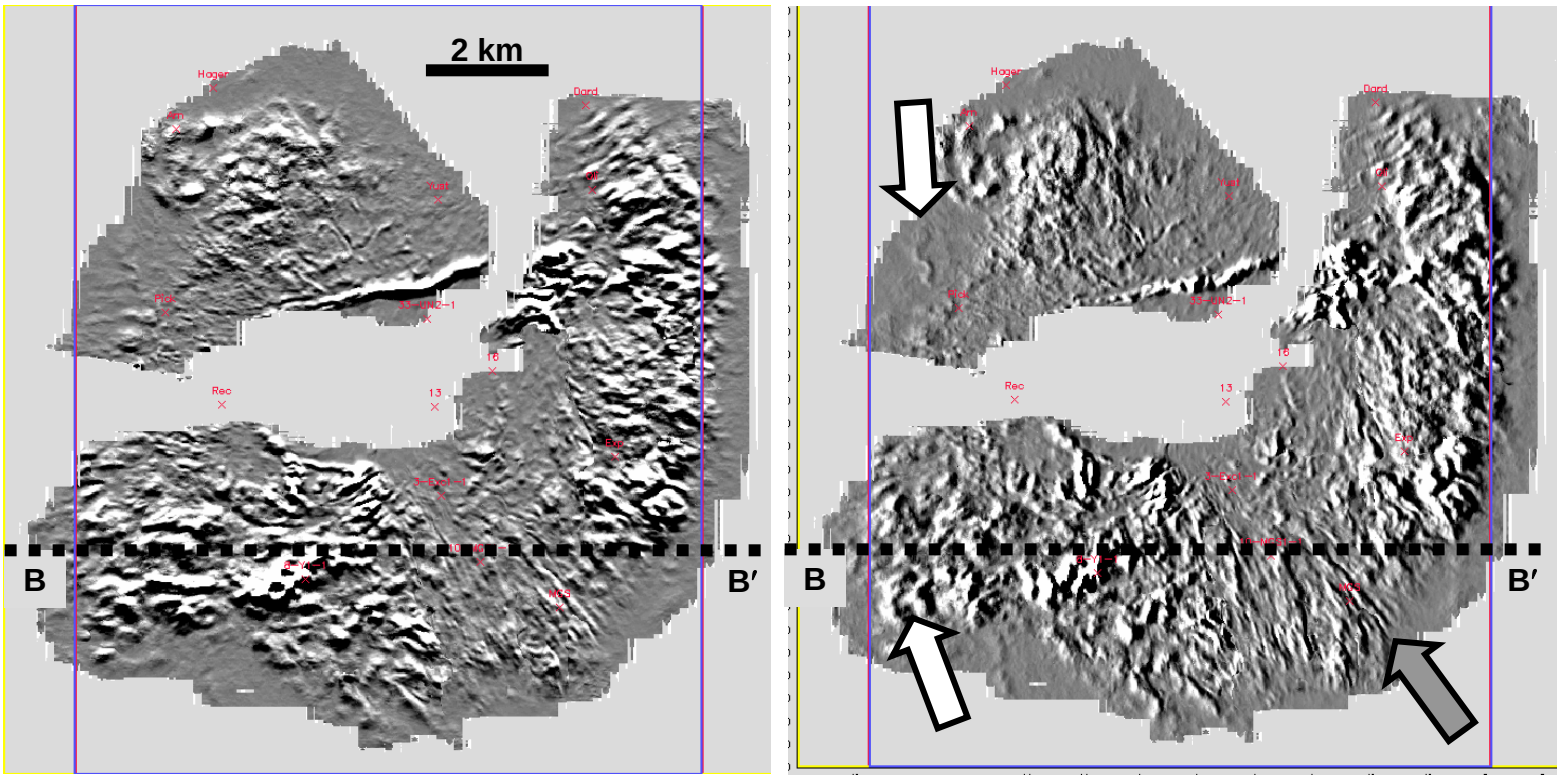

Figure 2.8.9. Horizon slice through the coherent energy gradient volumes along (a) the Mid Miocene and (b) Hackberry levels shown in Figure 2.8.7.

Curvature

Reflector curvature is one of the best accepted geologic models for the prediction of cracks or fractures. Such cracks, as well as other small discontinuities, are relatively small and below the imaging range of conventional seismic data. Reflector curvature is fractal in nature, with different tectonic and lithologic effects being illuminated at the 50 m and 1000 m scales. Until recently, such curvature estimates have been limited to the analysis of picked horizons. We define 2-D curvature in Figure 2.8.10. 3-D curvature is obtained by fitting a quadratic to the reflector at each surface, giving rise to two orthogonal curvatures. Mathematically we tend to compute the principal curvatures (Roberts, 2001) but for interpretation the most negative and most positive curvatures are more useful (Figure 2.8.11).

In Figure 2.8.12 we show a time slice at t=1.0 s through the coherence volume generated over Vinton Dome. We can see several faults radiating from the piercement dome. However, some of these faults fade out as we approach line AA'. In Figure 2.8.13 we display time slices at t=1.0s through the most negative and most positive curvature volumes. While the images clearly represent the same geology as the coherence image, many of these faults are significantly clearer on the curvature slices. We can see why this is the case by examining the vertical slice AA' in Figure 2.8.14. While several of the faults do indeed appear as discrete discontinuities (and show up on coherence), others appear to have fault drag or are possibly over- or under-migrated. While the seismic waveform measured by coherence appears continuous, curvature measures these longer wavelength changes in dip and azimuth.

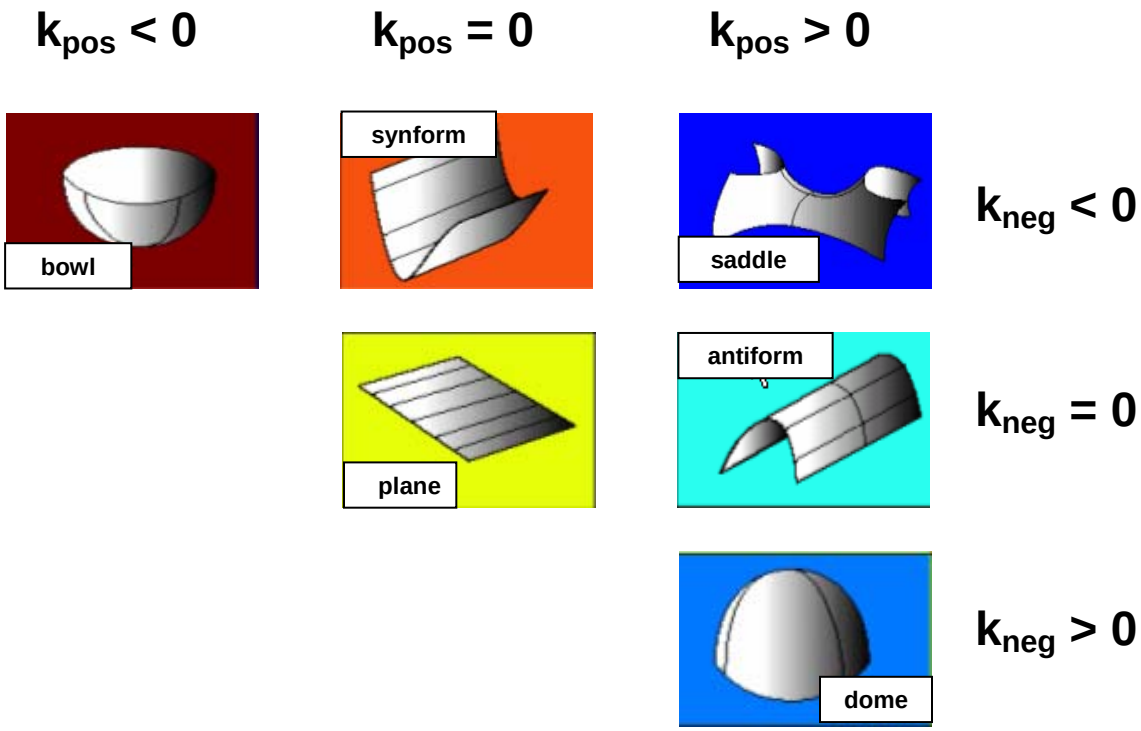

Figure 2.8.11. Definition of 3-D curvature. The most negative curvature, kneg, is always less than or equal to the most positive curvature, kpos. Thus, if the value of the most negative curvature is positive, we have a dome. If the value of the most positive curvature is negative, we have a bowl. If one of the curvatures is zero, we have a ridge or a valley. If both are zero, we have a plane. (After Bergbauer, 2003).

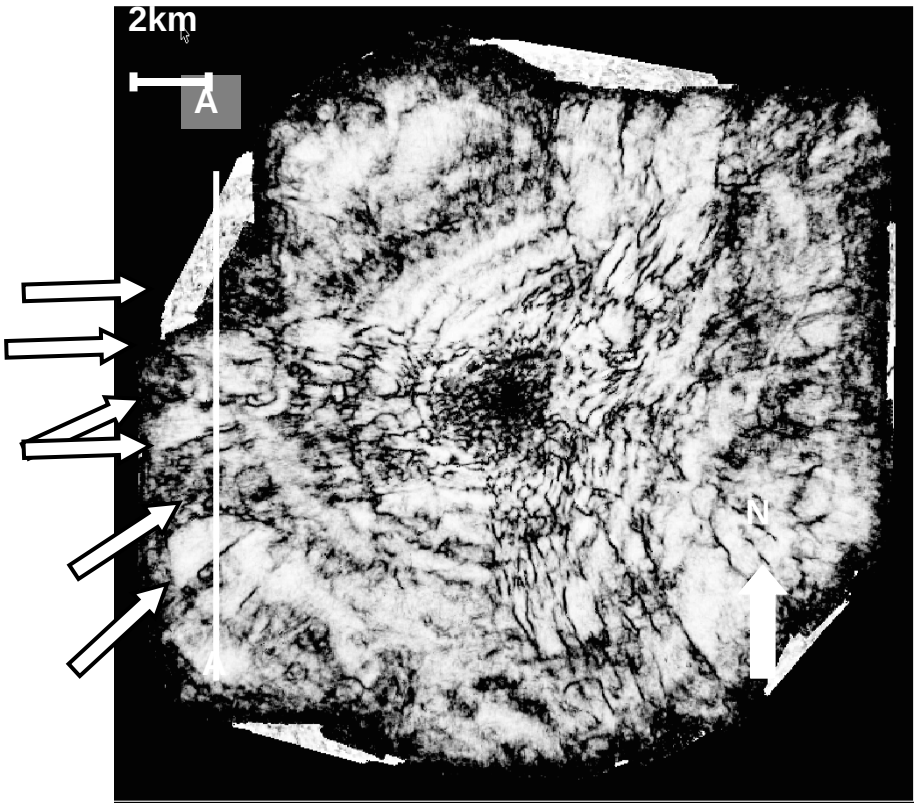

Figure 2.8.12. Time slice through the coherence volume over Vinton Dome at t=1.0s. White arrows indicate faults, not all of which are clear on the coherence time slice. (After al-Dossary and Marfurt, 2005).

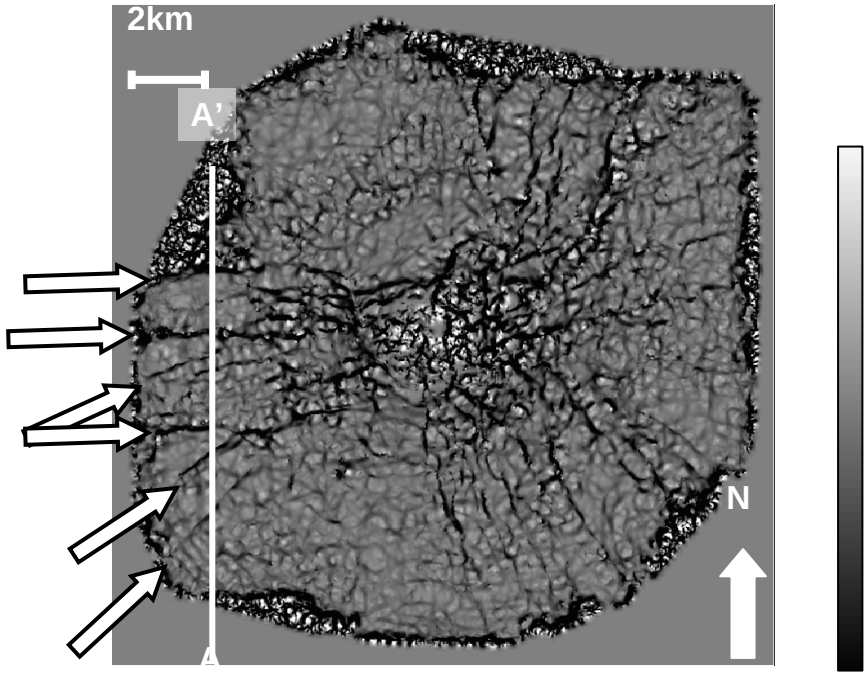

(a)

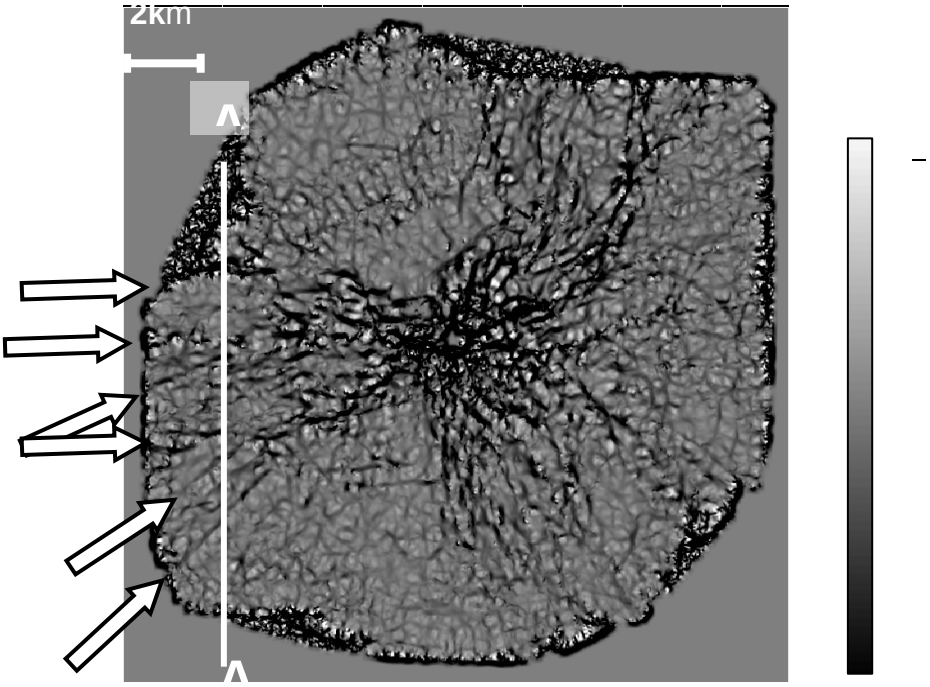

(b)

Figure 2.8.13. Time slice through the (a) Most negative curvature and (b) Most positive curvature volumes over Vinton Dome at t=1.0s. White arrows indicate faults, which are more clearly seen on the curvature time slices than on the coherence slice in Figure 2.8.12. (After al-Dossary and Marfurt, 2005).

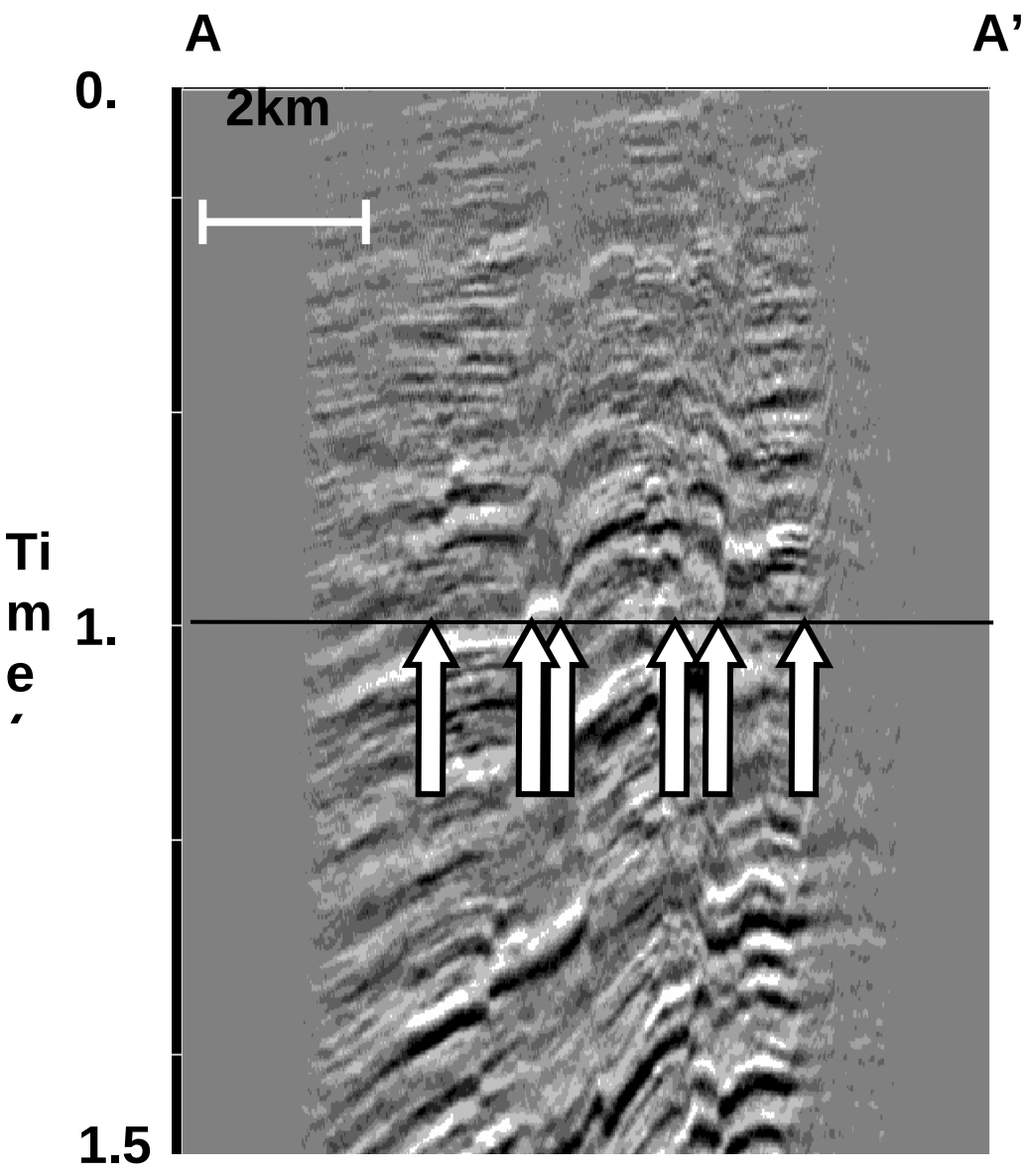

Figure 2.8.14. Vertical slice AA’ shown indicated on Figure 2.8.12-13. White arrows indicate faults shown on the times slices at t=1.0 s. Those faults which correspond to discrete discontinuities show up well on the coherence slice. Those that correspond to reflector drag or under- or over-migration show up better on the curvature slices. (After al-Dossary and Marfurt, 2005).

3.0 RESULTS AND DISCUSSION:

Our goal is to develop and calibrate new processing and interpretation technology to exploit the rich and largely untapped information content of a radial 3-D seismic survey and vector VSPs permanently cemented in boreholes in order to better image salt bodies and small scale geologic features. Our data included 3-D 3-C VSP data for two wells that was acquired simultaneous with the surface seismic, a time-migrated surface data cube, and well logs from the Vinton Dome Field in southwestern Louisiana. We used a variety of commercial software and AGL-developed algorithms to experimentally develop processing and interpretation technologies and workflows for better imaging of geologic features.

VSP data processing

We experimented with both Focus and Seisup commercial processing packages and adapted rotation algorithms written by graduate student Claudio d'Agosto for multicomponent surface seismic to the VSP geometry. Current production imaging algorithms, based on application of the adjoint of forward modeling equations, produce high fidelity subsurface images when they are applied to data with sufficiently large aperture and sufficiently high fold. Because the 3-D, 3-C VSP survey has severely limited receiver aperture, we reviewed adjoint-based imaging techniques and developed own modified technique, which is based on a data-derived dip constraint. Because our technique does not require us to solve an inverse problem, it may be used to precondition several inversion-based, alternate imaging techniques. We still need to “fine tune” the interaction between the migration constraints and the user-defined dip matching

tolerance. Once this is done, we anticipate that we will be able to better integrate our VSP image with the surface image. VSP images appear to have higher frequency than surface images, and should enable us to perform a more accurate reservoir characterization near the VSP well.

The results of our **VSP modeling study** contain two important implications for converted-wave/vector VSP salt flank imaging. **Firstly,** the salt flank reflections can closely parallel reflections from horizontal interfaces, as seen in the 2D SEG/EAGE salt structure, and often contain both up-going and down-going energy. Therefore, we must take great care not to remove this reflected energy in preprocessing before migration. **Secondly,** most PP reflection energy is recorded on the horizontal component for vertical interfaces and on the vertical component for horizontal interfaces and vice versa for PS reflections. Therefore, reverse time vector migration might be the most effective way of producing an image from the elastic wavefield suitable for fluid description (i.e., where we want a 'true amplitude' image containing both horizontal and vertical reflectors).

Our work indicates that **processing** of 3-D surface seismic land data can be improved with data specific workflows. We feel that in the case of Vinton Dome, designing a processing workflow specifically for radial acquisition could improve the premigration processing results.

We used a variety of new **seismic attributes**, both in interpretation and as an effective means for QC of data. In particular, we used coherence attributes for testing the two

different velocity models used to PSDM and for comparison of the PSTM to the PSDM volumes. Faults provide especially good features for testing. Fault boundaries are sharp discontinuities in properly migrated data and conversely, poorly migrated fault edge diffractions generate coherent events.

One of our most useful attributes for QC of data is a multitrace coherence measure that uses eigenvalues from the covariance matrix formed from traces in the analysis cube (Gersztenkorn and Marfurt, 1999). We ran coherence after structurally-oriented filtering. Our new edge preserving smoothing (al-Dossary, et al., 2002) appears to be superior to other methods of edge preservation such as fx-decon and operates on coherence data as well as conventional seismic data (Marfurt, et al., 2002).

Among our major accomplishments was the **tech transfer session** at the 2003 SEG meeting. Through coordination with the SEG, we initiated a special session at the 2003 SEG meeting on Vinton Dome, which integrated work by AGL, colleagues at Texas A&M, and at the University of Texas at Dallas. Together with poster presentations and papers that were put into other sections, AGL presented ***thirteen*** papers at the 2003 SEG, and obtained a great deal of interest not only from small independents, but also from technology providers like Schlumberger and Halliburton, and from researchers at major oil companies including ExxonMobil. This success is directly relevant to technology development of the future. In addition we have developed a publicly accessible website under www.agl.uh.edu to disseminate our findings to the exploration and scientific community at large. We have all our Vinton Dome presentations from SEG meetings on

this web site, and will ultimately have links to all theses. We now have incorporated the Vinton Dome survey, well logs, and a full suite of attributes into our graduate level course entitled **'3-D seismic interpretation I: Structure and stratigraphy'**. The new geometric attributes calibrated during this study are now being used to reduce geologic and mechanical risk in petroleum exploration across the state of Texas, especially in the Fort Worth Basin, where the State of Texas is benefiting from increased revenue from application of our attribute technology to the unconventional shale gas play. In addition, members of our team have recently submitted a proposal to the DOE to apply this technology to sequestration of CO_2.

Student theses and dissertations

An advantage of a large research project such as the Vinton Dome DOE project is that many students can build on the basic and applied science. The Vinton Dome project provided thesis projects for six graduate students, about two dozen publications, and is expected to result in at least four additional peer-reviewed publications. Following the conclusions in this report, we list twenty nine publications that resulted from this project to date.

4.0 CONCLUSIONS:

We achieved our goal to use data from a radial 3-D seismic survey and from permanent borehole based vector VSPs to develop and calibrate new processing and interpretation technology. A major part of the project was a subsurface illumination study that included 2-D/3-D multicomponent VSP modeling, 3-D 3-C VSP processing and 2-D/3-D scalar and elastic imaging. We developed a 3-D elastic VSP imaging algorithm that avoids some of the assumptions present in the current algorithms. We designed a new method of stacking common-image gathers based on semblance weighting to replace the common "mute" operation applied to the VSP images to remove the migration artifacts.
The Vinton Dome 3-D, 3-C VSP survey has severely limited receiver aperture, and we are developing our own modified adjoint-based imaging technique, which is based on a data-derived dip constraint. This methodology does not require us to solve an inverse problem, and may be useful in preconditioning inversion-based, alternate imaging techniques.

At Vinton Dome, the typical land survey processing challenges of noise, ground roll are compounded by the nontraditional acquisition parameters. We improved the fidelity of the 3-D seismic data by using an innovative method to model the velocity field for a 3-D PSDM. We used a simple pre-migration processing approach that allowed us to maintain a high bandwidth and eliminate noise.

Our well-based velocity model PSDM provided better definition of small fault blocks, and improved fidelity in imaging salt and faults planes. Although the well-based PSDM

is higher frequency and images faults and salt flanks better, the PSTM images the shallower faults almost as well, and demonstrates that the most powerful advantage of the PSDM is in areas of strong lateral velocity changes.

One of our biggest success stories in this project is in advancement of imaging small scale features through the improvement of edge preserving smoothing and development of a wide variety of multi-trace geometric attributes. Each robust seismic attribute generates an attribute volume that may be analyzed in time-slices or in horizon extractions and thus eliminates the need to interpret and smooth horizons prior to generation of attributes. We find that volumetric curvature attributes are particularly valuable in delineating subtle faults and fractures, as well as channels. Attribute based workflows are site-specific, but are easy to customize for rapid delineation of structure, stress regime and prediction of azimuth of open fractures.

In addition to presenting our work at all stages through local, regional, and international meetings and short courses, we convened a special session at the 2003 SEG meeting on Vinton Dome. This session presented integrated studies by AGL, colleagues at Texas A&M, and the University of Texas at Dallas. In addition to providing thesis and PhD projects for six graduate students, many other students worked part time on the project and together with faculty and industry collaborators, produced almost two dozen publications. Publications and presentations are publicly accessible at the AGL web site www.agl.uh.edu.

5.0 REFERENCES:

Abma, R., J. Sun, and N. Bernitsas, 1999, Antialiasing methods in Kirchhoff migration: Geophysics, **64**, 1783-1792.

Ahmed, H., P. B. Dillon, S. E. Johnstad, and C. D. Johnston, 1986, Northern Viking graben multilevel three-component walkaway VSP – A case history: First Break, **4**, 9-27.

Ahmed, H., 1987, Mode-Converted shear waves in 3-Component VSP data: 57th Annual International Meeting, Society of Exploration Geophysicists, Expanded Abstracts, 700-702.

Ahmed, H., 1990, Investigation of Azimuthal Anisotropy from offset VSP data: First Break, **8**, 449-457.

al-Dossary, S., K, J. Marfurt, and Y. Luo, 2002, Edge preserving smoothing: 72nd Annual International Meeting Society of Exploration Geophysicists, Salt Lake City.

al-Dossary, S, and K. J. Marfurt, 2005, Volume based estimates of spectral curvature, submitted to Geophysics

Alvarez, G., 1995, A comparison of moveout-based approaches to ground-roll and multiple suppression: M.Sc. Thesis, Colorado School of Mines.

Bardan, V., 1987, Trace interpolation in seismic data-processing: Geophysical Prospecting, **35**, 343-358.

Bickel, S. H., 1990, Velocity-depth ambiguity of reflection traveltimes: Geophysics, 55, 266-276.

Biondi, B., 2001, Kirchhoff imaging beyond aliasing: Geophysics, **66**, 654-666.

Bishop, T. N., Bube, K. P., Cutler, R. T., Langan, R. T., Love, P. L., Resnick, R. T., Shuey, R. T., Spindler, D. A., and Wyld, H. W., 1985, Tomographic determination of velocity and depth in laterally varying media: Geophysics, 50, 903-923.

Bleistein, N., 1987, On the imaging of reflectors in the earth: Geophysics, **52**, 931-942.

Bube, K. P. and Langan, R. T., 1994, A continuation approach to regularization for traveltime tomography, Expanded Abstracts of SEG 64th Ann. Internat. Mtg., 980-983.

Bube, K. and Langan, R., 1999, On a continuation approach to regularization for crosswell tomography, Expanded Abstracts of SEG 69th Ann. Internat. Mtg., 1295-1298.

Constance, P. E., S. Roche, P. Bicquart, B. Bryans, S. Gelinsky, J. G. Ralph, and R. Bloor, 1999, Simultaneous acquisition of 3-D surface seismic data and 3-C, 3-D VSP data: 69th Annual International Meeting, Society of Exploration Geophysicists, Expanded Abstracts, 104-107.

Chiu, S.K.L., and Stewart, R.R., 1987, Tomographic determination of three-dimensional seismic velocity structure using well logs, vertical seismic profiles, and surface seismic data: Geophysics, 52, 1085-1098.

D'Agosto, C., 2002, Modeling and removal of ground roll from horizontal component of C-waves: M.Sc. Thesis, University of Houston.

De, G.S., Winsterstein, D.F., and Meadows, M.A., 1994, Comparison of P- and S-wave velocities and Q's from VSP and sonic log data: Geophysics, 59, 1512-1529.

DiSiena, J.P., J. E. Gaiser, and D. Corrigan, 1984, Horizontal components and shear wave analysis of three-component VSP data, in Toksoz, M.N., and Stewart, R.R., Eds., Vertical Seismic Profiling: Advanced concepts: Geophysical Press, 177-188.

Dix, C. H., 1955, Seismic velocities from surface measurements, Geophysics, **20,** 68-86.

Duncan, W. 2005, A deterministic evaluation of seismic fidelity using velocity modeling and attribute analysis to improve surface seismic imaging around Vinton Dome, Louisiana: PhD thesis, University of Houston.

Eubanks, L. G., 1987, North Sabine Lake Field, Complex deformation and reservoir morphology of lower Hackberry (Oligocene), Southwest Louisiana, AAPG Bulletin, **71**, 1162-1170.

Fails, T.G., 1990, Variation in salt dome faulting, Coastal Salt Basin: Transactions, Gulf Coast Association of Geological Societies, **40**, 181-193.

Foster, D. J. and C. C. Mosher, 1988, Up and Downgoing wave field separation for multioffset single level VSP data: 68th Annual International Meeting, Society of Exploration Geophysicists, Expanded Abstracts, 816-818.

Gaiser, J. E., 1999, Application of 3-D vector coordinate systems for 3-D converted wave data: The Leading Edge, **18**, 1290-1300.

Gardner, G. H. F., W. S. French, and T. Matzuk, 1974, Elements of migration and velocity analysis: Geophysics, **39**, 811-825.

Gersztenkorn, A., and K. J. Marfurt, 1999, Eigenstructure-based coherence computations as an aid to 3-D structural and stratigraphic mapping: Geophysics, **64**, 1468-1479

Gherasim, M., 2005, 3-D VSP elastic Kirchhoff pre-stack depth migration - Vinton Dome, Louisiana: Ph.D. Thesis, University of Houston.

Gibson, R. L. and C. Tzimeas, 2002, Quantitative measures of image resolution for seismic survey design: Geophysics, **67**,1844-1852.

Gray, S. H., 1992, Frequency-selective design of the Kirchhoff migration operator: Geophysical Prospecting: **40**, 565-572.

Gray, S. H., 1998, Speed and accuracy of seismic migration methods: Mathematical Geophysics Summer School at Stanford University.

Grech, M.G.K., Lawton, D.C., and Gray, S.H., 2002, A multioffset vertical seismic profiling experiment for anisotropy analysis and depth imaging: Geophysics, 67, 348-354.

Guevara, S. E. and R. R. Stewart, 2001, 3-C geophone orientation and wave modes polarization: 71st Annual International Meeting, Society of Exploration Geophysicists, Expanded Abstracts, 799-801.

Guo, N., and S. Fagin, 2002a, Becoming effective velocity-model builders and depth imagers, part1-the basics of prestack depth migration: The Leading Edge, **21**, 1250-1209.

Guo, N., and S. Fagin, 2002b, Becoming effective velocity-model builders and depth imagers, part2-the basics of velocity-model building, examples and discussion: The Leading Edge, **21**, 1210-1216.

Halbouty, M. T., 1972, Salt Domes Gulf Region, U.N. and Mexico: 2nd Edition, Gulf Publishing Company, Houston.

Hinds, R.C., N. L. Anderson, and R. D. Kuzmiski, 2001, VSP Interpretive Processing: Theory and Practice: Short Course Notes, Open File Publications No.3, SEG.

Hoelting, C., W. Duncan, M. Gherasim, K. Marfurt, and H. Zhou, 2002, A preliminary study of salt flank illumination at Vinton Dome, Louisiana: Do we need lateral wavefield continuation?, 72nd Annual International Meeting, Society of Exploration Geophysicists, Expanded Abstracts, 1368 – 1371.

Hoelting, C., M. Gherasim, W. Duncan, K. Marfurt, and H. Zhou, 2003a, A preliminary study of salt flank illumination at Vinton Dome, Louisiana: Do we need lateral wavefield continuation?: The Leading Edge, **22,** 974-975.

Hoelting, C., M. Gherasim, L. House, and K. Marfurt, 2003b, Elastic modeling and steep dips: unraveling the reflected wavefield: 73rd Annual International Meeting, Society of Exploration Geophysicists, Expanded Abstracts, 1833-1836.

Jackson, G. M., I. M. Mason, and D. Lee, 1991, Multicomponent common-receiver gather migration of single-level walk-away seismic profiles: Geophysical Prospecting, **39**, 1015-1030.

Jackson, M. P. A., and W. E. Galloway, 1984, Structural and Depositional styles of Gulf Coast Tertiary Continental Margins: Application to Hydrocarbon Exploration: Continuing Education Course Note Series, **25**.

Jackson, M. P. A. and C. J. Talbot, 1986, External shapes, strain rates, and dynamics of salt structures: Geological Society of America Bulletin, **97**, 305-323.

Jackson, M.P.A., D. G. Roberts, and S. Snelson, 1995, Salt Tectonics: A global perspective: AAPG Memoir **65**.

Kebaili, A., and Schmitt, D.R., 1996, Velocity anisotropy observed in wellbore seismic arrivals: Combined effects of intrinsic properties and layering: Geophysics, 61, 12-20.

Kosloff, D., Sherwood, J., Koren, Z., Machet, E., and Falkovitz, Y., 1996, Velocity and interface depth determination by tomography of depth migrated gathers: Geophysics, 61, 1511-1523.

Lee, M.W., 1990, Traveltime inversion using transmitted waves of offset VSP data: Geophysics, 55, 1089-1097.

LeVie, D. S., 1986, Interdomal Sediment ponding: a new Lower Hackberry play?: Gulf Coast Association of Geological Societies Transactions, v. 35, 171-178

Lin, I., K. J. Marfurt, and O. Johnson, 2003, Mapping 3D multiattribute data into HLS color space - Applications to Vinton dome, LA, 73rd Annual International Meeting: Society of Exploration Geophysicists, Expanded Abstracts, 1728-1731.

Lines, L. R., Bourgeois, A., and Covey, J. D., 1984, Traveltime inversion of offset vertical seismic profiles – A feasibility study: Geophysics, 49, 250-264.

Liu, W., A. Popovici, D. Bevc, and B. Biondi, 2001, 3-D migration velocity analysis for common image gathers in reflection angle domain, 71st Annual International Meeting, Soc. of Expl. Geophys., Expanded Abstracts, 925-928.

Lizarralde, D., and S. Swift, 1999, Smooth inversion of VSP traveltime data: Geophysics, 64, 659-661.

Lumley, D. E., J. Claerbout, and D. Bevc, 1994, Anti-aliased Kirchhoff 3-D migration: 64th Annual International Meeting: Society of Exploration Geophysicists, Expanded Abstracts, 1282-1285.

Marfurt, K. J., W. Duncan, and P. Constance, 2002, Comparison of 3-D edge detection seismic attributes to Vinton Dome Louisiana: 72nd Annual International Meeting Society of Exploration Geophysicists, Salt Lake City.

Martin, G. S., K. J. Marfurt, and S. Larsen, 2002, marmousi-2: an updated model for the investigation of AVO in structural complex areas: 72nd Annual International Meeting Society of Exploration Geophysicists, Expanded Abstracts, 1979-1982.

Moon, W., A. Carswell, R. Tang, and C. Dilliston, 1986, Radon transform wave field separation for vertical seismic profiling data: Geophysics, **51**, 940-947.

Moret, G.J.M., Clement, W.P., Knoll, M.D., and Barrach, W., 2004, VSP traveltime inversion: Near-surface issues: Geophysics, 69, 345-351.

Nemeth, T., Qin, F. and Normark, E., 1993, Dynamic smoothing in crosswell tomography, Expanded Abstracts of SEG 63rd Ann. Internat. Mtg., 118-121.

Schultz, P., 1999, The seismic velocity model as an interpretation asset: Society of Exploration Geophysicists, Tulsa, OK, 202p.

Sheriff, R.E., and L. P. Geldart, 1995, Exploration Seismology: 2nd Edition, Cambridge University Press.

Stewart, R.R., Huddleston, P.D., and Kan, T.K., 1984, Seismic versus sonic velocities: A vertical seismic profiling study: Geophysics, 49, 1153-1168.

Stolt, R., and A. Benson, 1986, Seismic Migration, Theory and Practice: Handbook of Geophysical Exploration, **5**, Geophysical Press.

Tabbi-Anneni, A., 1975, Subsurface geology of south central Calcasieu Parish,Louisiana: M.Sc. Thesis, The Universiy of Southern Louisiana.

Thompson, S.A., and O. H. Eichelberger, 1928, Vinton salt dome, Calcasieu Parish, Louisiana: Amer. Assoc. of Petrol. Geol. Bull., **12**, 385-394.

Tichelaar, B.W., and Ruff, L.J., 1989, How good are our best models? Jackknifing, bootstrapping, and earthquake depth: Eos, 593-606.

Wang, D., 2004, Vector 3C 3D VSP Kirchhoff Migration: 74th Annual Internation Meeting, Society of Exploration Geophysicists, Expanded Abstracts, 1455-1458.

Warren, A. D., 1957, The Anahuac and Frio sediments in Louisiana: Transactions, Gulf Coast Association of Geological Societies, **7**, 221-237.

Washbourne, J., Rector, J. W. and Bube, K., 2002, Crosswell traveltime tomography in three dimensions: Geophysics, 67, 853-871.

Wilson, F., and J. A. Noel, 1983, A gravity analysis of west-central Calcasieu Parish, Louisiana: Transactions, Gulf Coast Association of Geological Societies, **33**, 243-250.

Wynn, T. J., and S. A. Stewart, 2003, The role of spectral curvature mapping in characterizing subsurface strain distributions, Geological Society of London Special Publication No. **209**, 127-143.

Zhou, H., 2003, Multi-scale traveltime tomography: Geophysics, 68, 1639-1649.

Zhou, H., 2004, Direct inversion of velocity interfaces: Geophys. Res. Lett., 7, doi: 10.1029/2003GL019318.

Zhou, H., 2005a, Deformable layer tomography, Geophysics, in press.

Zhou, H., 2005b, First-break VSP Tomography for Vinton Dome, Geophysics, in press.

Zhou, R., Z. Patval, D.D. McAdow, S. Singh, F. Doherty, D. Dushman, and C. Barberan, 2003, Anisotropy estimation using walkaway VSP data: 65th Mtg., Eur. Assn. Geosci. Eng., F43.

6.0 TECHNICAL PAPERS RESULTING FROM THIS PROJECT

al-Dossary, S., and K. J. Marfurt, 2003, Improved 3D seismic edge-detection filter applied to Vinton Dome, Louisiana, 73rd Annual International Meeting: Society of Exploration Geophysicists, Expanded Abstracts, 2370-2372.

al-Dossary, S., and K. J. Marfurt, 2003, Fracture-preserving smoothing, 73rd Annual International Meeting: Society of Exploration Geophysicists, Expanded Abstracts, 378-381.

al-Dossary, S., K, J. Marfurt, and Y. Luo, 2002, Edge preserving smoothing: 72nd Annual International Meeting Society of Exploration Geophysicists, Salt Lake City.

al-Dossary, S., and K. J. Marfurt, 2005, Multispectral estimates of reflector curvature and rotation: Submitted to Geophysics.

al-Dossary, S., and K. J. Marfurt, 2005, Lineament-preserving filtering: Submitted to Geophysics.

Constance, P., 2003, Vinton Salt Dome, current issues in structural imaging: 73rd Annual International Meeting: Society of Exploration Geophysicists, Expanded Abstracts, 2357-2361.

Duncan, W., 2003, Using seismic data to improve the geologic model of the Vinton Dome area: 73rd Annual International Meeting: Society of Exploration Geophysicists, Expanded Abstracts, 2175-2178.

Duncan, W., 2003, Using seismic attributes as a QC for velocity model building - Vinton Dome, Louisiana, 73rd Annual International Meeting: Society of Exploration Geophysicists, Expanded Abstracts, 2199-2202.

Duncan, W., 2003, Velocity model building of Vinton Dome, Southwest Louisiana, 73rd Annual International Meeting: Society of Exploration Geophysicists, Expanded Abstracts, 2175-2178.

Duncan, W., 2003, Defining the structural and stratigraphic model for Vinton Dome, Louisiana, 73rd Annual International Meeting: Society of Exploration Geophysicists, Expanded Abstracts, 2353-2356.

Duncan, W., and K. J. Marfurt, 2003, Improved attributes for the interpretation and QC of the Vinton Dome 3D surface seismic: 73rd Annual Internatational Meeting Society of Exploration Geophysicists, Expanded Abstracts, 2199-2202.

Duncan, W.S., and H. Zhou, 2005, Velocity modeling of land 3-D surface seismic data for prestack depth migration, AGU 2005 Joint Assembly, New Orleans.

Hoelting, C., W. Duncan, M. Gherasim, K. Marfurt, and H. Zhou, 2002, A preliminary study of salt flank illumination at Vinton Dome, Louisiana: Do we need lateral wavefield continuation?, 72nd Annual International Meeting, Society of Exploration Geophysicists, Expanded Abstracts, 1368 – 1371.

Hoelting, C., M. Gherasim, W. Duncan, K. Marfurt, and H. Zhou, 2003a, A preliminary study of salt flank illumination at Vinton Dome, Louisiana: Do we need lateral wavefield continuation?: The Leading Edge, **22,** 974-975.

Hoelting, C., M. Gherasim, L. House, and K. J. Marfurt, 2003b, Elastic modeling and steep dips: Unraveling the reflected wavefield, 73rd Annual International Meeting: Society of Exploration Geophysicists, Expanded Abstracts, 1833-1836.

Jovanovic, K., and K. J. Marfurt, 2004, P and S waves separation from vector VSP's by a blocky antialias discrete Radon transform: Application to Vinton Dome, LA, 75th Annual International Meeting Society of Exploration Geophysicists, Expanded Abstracts, 2513-2516.

Jovanovic, K., and K. J. Marfurt, 2005, P and SV polarization filtering of a multicomponent vector VSP: Submitted to Geophysics.

Kisin, S. and H. Zhou, 2002, Reflection tomography of converted waves, 6th Workshop on Three-Dimensional Modeling of Seismic Waves Generation, Propagation and Their Inversion, ICTP, Trieste.

Kisin, S. and H. Zhou, 2003, VSP tomography of Vinton Dome, Louisiana, 73rd Annual International Meeting: Society of Exploration Geophysicists, Expanded Abstracts, 2349-2352.

Lapin, S., S. Kisin, and H. Zhou, 2003, Joint VSP and surface seismic tomography, 73rd Annual International Meeting: Society of Exploration Geophysicists, Expanded Abstracts, 2342-2344.

Lapin, S., S. Kisin, H. Zhou, and K. Marfurt, 2002, Reflection tomography: theory and practice, 6th Workshop on Three-Dimensional Modeling of Seismic Waves Generation, Propagation and Their Inversion, ICTP, Trieste.

Lin, I., K. J. Marfurt, and O. Johnson, 2003, Mapping 3D multiattribute data into HLS color space - Applications to Vinton dome, LA, 73rd Annual International Meeting: Society of Exploration Geophysicists, Expanded Abstracts, 1728-1731.

Lin, Q., and H. Zhou, 2003, A study of long-offset seismic imaging, 73rd Annual International Meeting: Society of Exploration Geophysicists, Expanded Abstracts, 1154-1157.

Marfurt, K. J., W. Duncan and P. Constance, 2002, Comparison of 3-D edge detection seismic attributes to Vinton Dome Louisiana: 72nd Annual International Meeting Society of Exploration Geophysicists, Salt Lake City.

Marfurt, K. J., 2005, Robust estimates of reflector dip and azimuth: Submitted to Geophysics.

Yoon, K., K. J. Marfurt, and W. Starr, 2004, Challenges in reverse-time migration: 74th Annual International Meeting Society of Exploration Geophysicists, Expanded Abstracts, 1057-1060.

Zhou, H., 2002, Kirchhoff reflection tomography: Concept and preliminary result: 72nd Annual International Meeting Society of Exploration Geophysicists, Expanded Abstracts, 953-956.

Zhou, H., 2003, Deformable layer tomography and application to the Vinton Dome, 73rd Annual International Meeting Society of Exploration Geophysicists, Expanded Abstracts, 2345-2348.

Zhou, H., 2004, Direct inversion of velocity interfaces, Geophys. Res. Lett. 7, doi: 10.1029/2003GL019318, 2004.

Zhou, H., 2004, VSP multi-scale deformable layer tomography, 74th Annual International Meeting Society of Exploration Geophysicists, Expanded Abstracts, 2327-2330.

Zhou, H., 2005, Deformable layer tomography, Geophysics, in press.

Zhou, H., 2005, First-break VSP Tomography for Vinton Dome, Geophysics, in press.